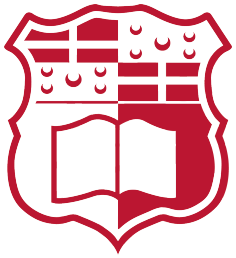

Extended commissioning and validation of the Comprehensive Motion Management (CMM) system on an Elekta Unity MR-Linac

Maronia Chetcuti

Supervised by Mr Martin Pirotta

Co-supervised by Mr Paul B. Bezzina

Medical Physics Unit

Faculty of Health Sciences

University of Malta

September, 2025

A dissertation submitted in partial fulfilment of the requirements for the degree of the Masters in Medical Physics of the Faculty of Health Sciences of the University of Malta .

WWW.UM.EDU.MT

First edition, September 28, 2025

L-Università ta' Malta

FACULTY/INSTITUTE/CENTRE/SCHOOL___Health Sciences_____

DECLARATIONS BY POSTGRADUATE STUDENTS

(a) Authenticity of Dissertation

I hereby declare that I am the legitimate author of this Dissertation and that it is my original work.

No portion of this work has been submitted in support of an application for another degree or qualification of this or any other university or institution of higher education.

I hold the University of Malta harmless against any third party claims with regard to copyright violation, breach of confidentiality, defamation and any other third party right infringement.

(b) Research Code of Practice and Ethics Review Procedures

I declare that I have abided by the University's Research Ethics Review Procedures. Research Ethics & Data Protection form code _____FHS-2024-00640_____.

As a Master's student, as per Regulation 77 of the General Regulations for University Postgraduate Awards 2021, I accept that should my dissertation be awarded a Grade A, it will be made publicly available on the University of Malta Institutional Repository.

To those who once thought they couldn't

This work is for you.

Acknowledgements

I would like to express my heartfelt appreciation to:

My supervisor, Mr. Martin Pirotta for his enthusiasm and passion for the project and from whom I have learned so much. His support, encouragement, and expert guidance have been essential in shaping this research endeavour.

My co-supervisor and Head of the Medical Physics Department at SAMOC, Mr. Paul Bezzina, for trusting me with the opportunity to carry out this research project. I will be forever grateful.

To the friends I have made along the way during this university journey - Kelsey and Samuel - thank you for the moments we shared, whether filled with laughter, tears, or celebration. I will always cherish the memories we've created together over the past five years.

I am extremely grateful to Prof. Carmel J. Caruana, Head of the Medical Physics Department at FHS, for his unwavering support over the years and for the opportunities he has provided to help shape my academic journey. I will always be thankful for his guidance and encouragement.

To all the lecturers who have made this Master's journey all the more engaging, thank you. A special mention goes to Mr. Eric Pace, whose guidance during my B.Sc. dissertation greatly contributed to the development of my academic writing and thinking in this M.Sc. thesis, and whose continuous support has been invaluable throughout my academic journey.

To my entire family - Doris, Mario, Alastair, and Ylenia - and my dear friends Destiny, Hannah, and Ingrid. I am forever grateful for your patience and understanding throughout this academic journey. Whether I managed to join you for just a few hours or had to cancel plans due to the demanding workload, your constant support has meant so much to me.

Abstract

Background The Elekta Unity MR-Linac (MRL), operational at Sir Anthony Mamo Oncology Centre (SAMOC) since July 2024, enables daily adaptive radiotherapy (ART) by adjusting treatment plans to account for tumour and anatomical changes. The Comprehensive Motion Management (CMM) system allows real-time motion tracking and gated beam delivery using different strategies, prompting the need for extended commissioning and validation to characterise performance under varied clinical conditions.

Objectives To design and deliver extended commissioning and validation tests on the Elekta CMM system, to quantify its positional and dosimetric accuracy across three selected gating strategies (respiratory, exhale navigated, and non-respiratory), and identify any potential limitations.

Research Methodology The MRI^{4D} MODUS QUASAR^{TM} phantom was commissioned to verify its positional accuracy, forming the basis for subsequent tests. A number of motion traces were used to challenge the system for the three gating strategies. Selected traces were used to quantify the Anatomic Position Monitoring (APM) positional accuracy, measure beam gating latency for both beam-on/off transitions, and assess the dosimetric impact of these parameters during different strategies. The dosimetric impact of different gating thresholds, volumetric overlapping criterion (VOICE) percentages, and complex waveforms was characterised using EBT4 film dosimetry.

Results APM analysis confirmed reliable target localisation within typically $<\pm 1$ mm across all strategies. In the respiratory strategy, regular waveforms met the manufacturer's latency specification, while irregular waveforms showed degraded performance. Film measurements for respiratory strategy indicated that regular breathing traces maintained target coverage (-0.40 ± 0.22mm change in prescription isodose), while irregular breathing may compromise dose conformity and reduce clinical target volume (CTV) coverage (-1.22 ± 0.23mm change). A trade-off was evident between gating window and efficiency: tighter gating thresholds (2mm) and VOICE 100% improved coverage (0.25 ± 0.20 and 0.08 ± 0.21mm) compared with 5mm and VOICE 95% (-1.13 ± 0.29 and -1.53 ± 0.21mm), but at the cost of delivery efficiency (3.3-5.5$\times$ longer). All gating scenarios retained gamma pass rates >97% (3%/2 mm), but a slight reduction was observed for challenging deliveries.

Conclusions and Recommendations The CMM system demonstrated robust performance under regular conditions but limitations where characterised under irregular motion including CTV coverage reduction and may need to be accounted for clinically but further investigation is required. Future work should validate CMM in lung-equivalent 4D phantoms and further assess the exhale-navigated strategy.

Keywords: MR-Linac, motion management, gating, respiratory motion phantoms, commissioning, and dosimetry.

Contents

List of Figures

List of Tables

List of Abbreviations

ED Electron densities 14

GTV Gross Tumor Volume 51

IGRT Image-Guided Radiation Therapy 33

IMRT Intensity-modulated Radiotherapy 127

ITV Internal Target Volume 102

Linac Linear Accelerator 7

LR Left-Right 87

MR Magnetic Resonance 97

MRgRT MR guided radiotherapy 33

MRI Magnetic Resonance Imaging 16

MRL Magnetic Resonance Linac 103

MU Monitor Units 61

OAR Organs at Risk 9

OD Optical Density 62

PET Positron Emission Tomography 9

PTV Planning Target Volume 103

QA Quality Assurance 128

QC Quality Control 73

RF Radiofrequency 13

RMSE Root Mean Square Error 88

RO Radiation Oncology 7

ROI Region of Interest 54

RT Radiation Therapy 20

SAMOC Sir Anthony Mamo Oncology Centre 63

SBRT Stereotactic Body Radiotherapy 127

1

Introduction

1.1 | Introduction

This chapter presents the problem statement, background and context, objectives, scope, summary of research methodology, ethical considerations and relevance of the study.

1.2 | Problem Statement

An Elekta Unity magnetic resonance linac (MRL) started clinical operations at Sir Anthony Mamo Oncology Centre (SAMOC) in Mater Dei Hospital on 29th July 2024. It is designed for daily adaptive radiotherapy (ART) where the treatment plan is adjusted during each session to account for changes in the shape of the tumour and other daily anatomical changes.

Comprehensive Motion Management (CMM) is a recent technological advancement on the Elekta Unity MRL that enables real-time tracking of tumour motion and allows for gated delivery of the radiation treatment. Acceptance testing of CMM was carried out prior to clinical use based on manufacturer recommendations, to ensure that the system was within manufacturer-stated tolerances. At the same time, there is a motivation to perform extended commissioning and validation tests to characterize the system

in greater detail and hence develop a deeper understanding of the performance of the system under a wide range of clinical conditions.

1.3 | Background and Context

An MRL provides superior soft-tissue visualization during treatment (Rammohan et al., 2022). The Elekta Unity 1.5T MRL was one of the first clinically implemented systems and has undergone continuous development since its introduction. A major advancement was the release of the CMM system, which received CE marking in October 2022 and U.S. FDA 510(k) clearance in February 2023 (Elekta, 2022, 2023a). CMM enables continuous real-time imaging and automatic gating which synchronises radiation delivery with tumour motion, and interrupt treatment when the tumour moves outside specified tolerances (Winkel et al., 2019). CMM employs four gating strategies (respiratory, exhale navigated, deep inspiration breath hold (DIBH), and non-respiratory) and incorporates a predictive algorithm to mitigate system latency and increase gating accuracy for respiratory motion (Brown, 2024).

Validation of motion management systems typically use motion phantoms that reproduce patient breathing patterns, enabling the evaluation of complex motion waveforms and system response (Viel et al., 2015). Dosimetric verification is typically performed using ion chambers or radiochromic film embedded within phantoms, allowing comparison of static reference versus dynamic deliveries with and without gating (Oliver et al., 2008; Wang et al., 2012).

Gating reduces the dosimetric consequences of intrafraction motion caused by respiratory movements or physiological changes. Respiratory movement leads to blurring of dose distributions, reduced target coverage, and increased dose to surrounding healthy tissues (Bortfeld et al., 2002). Physiological changes such as in stable sites (e.g., prostate) benefit from gating by pausing delivery when the target moves out of specified tolerances (Brown, 2024). The precision of such treatments is influenced by multiple factors:

the beam-on/off latency (Cui et al., 2014), the responsiveness of the system to irregular or abrupt patient motion (Han et al., 2019; Schnarr et al., 2018),the size of the gating window, the system latency, and the design of tracking and prediction algorithms (Johno et al., 2018).

Several studies have investigated dosimetric accuracy involving these factors. Across regular and irregular waveforms, gated deliveries maintained a good performance, with only slight degradation for irregular traces (Han et al., 2019; Nioutsikou et al., 2008). Studies also showed the effectiveness of prediction algorithms which mitigate gating delays and reduce target error caused by motion, improving delivered dose accuracy (Johno et al., 2018). A consistent finding between studies is the trade-off between the gating window size and treatment times. The narrower the gating window the better the recovery of the static reference but the longer the treatment times, while wider windows increase efficiency at the expense of residual blurring and reduced recovery of the reference (Pepin et al., 2011; Shiinoki et al., 2016).

The majority of this evidence, however, derives from conventional linacs or alternative MR guided RT (MRgRT) systems. Published validation studies of the Elekta Unity in clinical practice remain limited, underscoring the need for extended commissioning and performance validation for a more detailed characterisation of this system.

1.4 | Objectives of the Study

The objectives of the study were to:

1. Design and deliver extended commissioning and validation tests on the Elekta CMM system, informed by a review of existing methodologies in both MRL and non-MRL contexts.

2. Quantify the positional and dosimetric accuracy of the system within a wide range of clinical situations for three selected strategies: respiratory, exhale navigated,

and non-respiratory.

3. Identify any potential limitations of the system, if any.

1.5 | Scope of the Study

This study was limited to the evaluation of respiratory, exhale-navigated, and non-respiratory strategies, as the DIBH strategy was not evaluated because it is not in clinical use at SAMOC and there are no plans for its near-term implementation. All extended commissioning and validation tests were therefore conducted under these three strategies.

1.6 | Research Methodology

- The accuracy of the Modus QUASAR^{TM} Phantom (Modus Medical Devices, London, Ontario, Canada) was tested to verify compliance with manufacturer specifications and confirm its use as a simulation tool for the subsequent testing phases in this study.
- Waveforms provided directly by the Modus phantom manufacturer (or modified as required), as well as additional waveforms derived from literature (Smith et al., 2025) were used, selecting those that best tested and challenged the three gating strategies.
- In the first phase of this study, the Anatomic Position Monitoring (APM) system was evaluated to assess compliance with Elekta's specification that 95% of sampled points remain within ± 2 mm of the Modus QUASAR^{TM} Phantom recorded (ground-truth) position across all three cardinal axes. Importantly, testing was designed to extend beyond standard quality control (QC) procedures, using the Modus QUASAR^{TM} phantom, applying a range of programmed waveforms across the three selected strategies to evaluate APM performance.

- In the second phase, system latency performance was measured to evaluate beam delivery transitions for the selected waveforms and strategies. Testing was performed using the same set-ups as for APM but using ±5mm gating threshold for superior-inferior (SI). A single-beam 3D conformal radiotherapy (3DCRT) plan was delivered to all the selected waveforms and strategies. Beam on/off signals were recorded, ensuring multiple gating events for reliable analysis.

- In last phase, film dosimetry was performed to evaluate the dosimetric impact of free-breathing respiratory gating strategies. Gafchromic EBT4 films were used with the Modus QUASAR^{TM} phantom using the film cylindrical insert. An intensity-modulated radiotherapy (IMRT) 7 Gy stereotactic body radiotherapy (SBRT) plan with a Ø3 cm target was generated using the Monaco® treatment planning system (TPS). A static film measurement was taken as a reference. For subsequent measurements, a sinusoidal 10 mm, 14 bpm waveform was selected as the standard waveform which was delivered and tested using: ungated motion, different displacement gating thresholds (2, 3, 5 mm), different volumetric overlapping criterion (VOICE) gating (100, 97, 95%). In addition, typical and irregular motion patterns were used to capture more complex breathing patterns. Films were then digitised using a 10000XL Epson scanner, with scaling applied to account for dose-response variations, enabling accurate comparison of different gated and ungated deliveries against the static reference. Plan delivery efficiencies were evaluated using the CMM audit log files. Analysis of profile widths, midpoints, prescription isodose line overlays, and gamma analysis were conducted using a cloud-computing application (`radiochromic.com`).

1.7 | Ethical Considerations

This study was performed using a respiratory motion phantom, at no point were there any patients involved or any actual patient data. Ethical approval was granted by the University Research Ethics Committee of the University of Malta (Appendix C).

1.8 | Relevance of the Study

By extending testing beyond manufacturer recommendations for acceptance testing, the study assesses real-time tumour tracking and gated delivery capabilities of the CMM, thus validating its performance across diverse clinical situations. This study will benefit the patient as it improves confidence in the clinical performance of the system in greater detail for various patient cases. Moreover, it will also help the Medical Physics and Radiation Protection profession to be more confident in the performance of the system when applying it to an extended range of treatment sites. In addition, it will help develop a deeper understanding of the performance of the system.

1.9 | Conclusion

This chapter introduced the study. A literature review follows in Chapter Two. Chapter Three details the methodology, whilst Chapter Four presents and analyses the results. Chapters Five and Six provide key findings, recommendations, and future research directions.

2

Literature Review

2.1 | Introduction

A literature review was initiated using the following electronic search engines/databases until 25th August 2025: HyDi Software, Google Scholar, and PubMed search engine. The following keywords were used to search for articles in line with the PICO framework: MRL, motion management, gating, respiratory motion phantoms, commissioning, and dosimetry.

Only papers published in the last 10 years were considered (2015-2025) for the review of recent developments in MRL motion management. Older papers were only included if of crucial importance to the project and if they represent foundational contributions to the field. Selected articles had to satisfy the following inclusion criteria: (1) full-text papers written in the English language; and (2) studies linking MR-Linac, MRI, conventional linac, or any image-guided radiation therapy (IGRT) with motion management. Exclusion criteria included: (1) insufficient data; and (2) inadequate methodology.

2.2 | MRgRT in Modern Radiotherapy

Radiation oncology (RO) has advanced significantly through innovations in engineering, imaging, physics, and technology, as well as enhanced knowledge of radiobiology

(Corradini et al., 2019). The integration of computed tomography (CT) in treatment planning led to the move from two-dimensional (2D) to three-dimensional conformal radiotherapy (3DCRT), and later to intensity-modulated RT (IMRT), which improved dose conformity but increased treatment time due to the higher number of monitor units (MUs) (Ng et al., 2023; Placidi et al., 2021; Taylor and Powell, 2004). This was addressed by volumetric-modulated arc therapy (VMAT), which reduced treatment times by dynamically modulating beam parameters across multiple angles (Rana, 2013).

The introduction of cone-beam CT (CBCT) enabled image-guided RT (IGRT) and adaptive RT (ART), adjusting treatment plans based on inter-fraction anatomical changes (Ng et al., 2023; Ocanto et al., 2024). However, CBCT provides poor soft tissue contrast, especially in the thorax and abdomen, limiting its role in ART (Ocanto et al., 2024).

The integration of MRI with linacs enabled the development of hybrid MRL, such as ViewRay MRIdian and Elekta Unity. These systems enabled the clinical implementation of MRgRT, providing superior soft tissue contrast for clearer differentiation between healthy and tumour tissues and enabling detection of physiological changes during treatment (Rammohan et al., 2022). Currently, MRLs can only employ IMRT delivery but research and technical development are ongoing to enable VMAT delivery on these systems (Placidi et al., 2021; Tsekas et al., 2022).

Beyond anatomical visualisation, MRgRT provides functional imaging, real-time tumour monitoring without fiducials, adaptive planning, and dose escalation potential through integration of functional imaging into adaptive treatment planning (Corradini et al., 2019; Datta et al., 2018). These capabilities make MRgRT particularly suited for tumours with significant motion, those tumours better defined on MRI or requiring reduced margins. When combined with stereotactic body radiation therapy (SBRT), it enables high-dose treatments over hypofractionated courses (typically five sessions or fewer), with improved sparing of healthy tissue and potentially better outcomes compared to conventional RT (Chiloiro et al., 2023; Ma, 2019).

2.2.1 | Volume definitions

Standardised volume definitions are essential for effective treatment planning, accurate dose calculations, and comparability of outcomes across studies. ICRU Report 50 (1992) and ICRU Report 62 (1999) outline key target and critical structure volumes that guide treatment planning and facilitate outcome comparisons. The primary volumes (Figure 2.1) used in 3D planning are the following:

Gross tumour Volume (GTV): The GTV encompasses the visible extent and location of the tumour. It is determined through a combination of imaging modalities (CT, MRI, positron emission tomography (PET), etc.), pathology, and clinical assessment (ICRU Report 50, 1992).

Clinical Target Volume (CTV): The CTV includes the GTV and surrounding tissue that can contain microscopic disease (ICRU Report 50, 1992).

Internal Target Volume (ITV): The ITV includes an additional margin around the CTV to account for variations in the size and position of the CTV, primarily due to respiratory motion and organ content (like bladder, rectum) (ICRU Report 62, 1999).

Planning Target Volume (PTV): The PTV includes a margin to the CTV (or ITV) to account for uncertainties from patient setup, machine tolerances, and internal motion, ensuring the prescribed dose consistently covers the CTV (ICRU Report 50, 1992).

Organ at Risk (OAR): The OAR is any tissue or organ that, if exposed to radiation beyond established dose contraints, may experience detrimental effects. In such cases, treatment plans are modified to ensure compliance with OAR dose constraints while maintaining target coverage (ICRU, 2010).

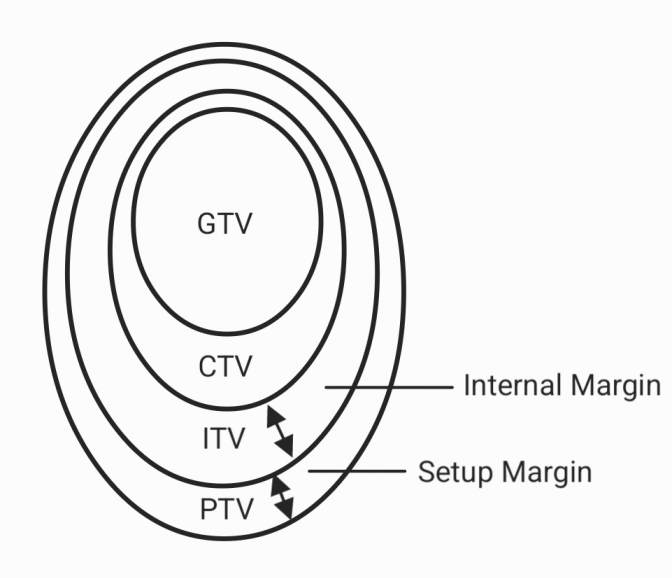

Figure 2.1: Target volumes in radiotherapy treatment planning.

2.2.2 | Clinical Applications of MRgRT

MRgRT can be applied for various diseases and multiple anatomical sites. In this section, some of the most common clinical applications are mentioned.

Prostate: MRI is routinely employed for prostate cancer diagnosis, staging, and treatment planning, effectively identifying malignant tissue and differentiating it from nearby organs like the bowel, rectum, bladder, and urethra (Benitez et al., 2023; Ng et al., 2023). MRgRT can track prostate motion caused by factors such as bowel gas, stool, bladder filling, and pelvic floor muscle activity. Moreover, MRgRT allows for enhanced intra-fractional monitoring of prostate motion during SBRT treatments (Cuccia et al., 2020; Ng et al., 2023). Another advantage is the ability to reduce the PTV margins while maintaining target coverage due to the improved tumor visualization (Ocanto et al., 2024).

Liver: Delineating GTV has been challenging despite using various imaging modalities (like contrast-enhanced CT) (Ng et al., 2023). However, MRgRT enables superior target characterization. Moreover, liver tumours are subject to substantial movement

in all three planes of motion which are well managed by the MRgRT's tumour-tracking system (Ocanto et al., 2024).

Lung: MRgRT is also used in central lung tumours. As demonstrated by Tekatli et al. (2023), their study showed excellent local control and low toxicity using MRgRT SBRT with reduced PTV margins and respiratory gating on patients with lung tumours. Additionally, Finazzi et al. (2020) reported reduced planning margins using breath-hold strategies compared to conventional ITVs for patients with peripheral tumours.

2.3 | General Techniques of Respiratory Motion Management

Intra-fraction motion or inter-fraction motion can result in discrepancies between the planned and delivered dose distributions (Keall et al., 2006). This is particularly important for respiratory motion, which affects most thoracic and abdominal tumours and, if unmanaged, degrades image quality, impairs target delination, and compromises dose calculations (Bortfeld et al., 2002; Keall et al., 2006). In techniques such as IMRT, which rely on steep dose gradients at field edges, this results in broadening of the penumbra and reduced conformity to the target (Bortfeld et al., 2002).

Increasing PTV margins to compensate is a suboptimal strategy as this results in an increased irradiation of healthy tissue. Conversely, insufficient margins may compromise target coverage, leading to suboptimal tumour control (Bortfeld et al., 2002). Thus, effective motion management is essential.

Strategies to mitigate respiratory motion in RT are described in detailed in the American Association of Physicists in Medicine (AAPM) TG-76. These approaches include motion-encompassing, respiratory gating, breath-hold, and real-time tumour-tracking techniques (Keall et al., 2006).

Motion-encompassing methods: (1) Inhalation and exhalation breath-hold CT where it acquires CT scans during both inhalation and exhalation phases. (2) 4D CT/respiration-correlated CT where inhalation and exhalation images can be reconstructed and analysed to identify the tumour's position, range of motion, as well as the tumour's relation to other organs (Szkitsak et al., 2021).

Respiratory gating methods: Respiratory gating is a technique employed to synchronise radiation delivery with specific phases of the respiratory cycle. This is accomplished through respiratory motion monitoring, utilizing either external respiration signals or internal fiducial markers.

Breath-hold methods: DIBH involves coaching the patient to achieve consistent deep inhalation and breath hold, expanding the lungs for better radiation delivery while sparing healthy tissue. Breath hold in combination with IMRT requires an accurate gating signal for radiation delivery.

Real-time tumour-tracking methods: This involves dynamically adjusting the radiation multileaf collimator (MLC) to follow tumour movement. In optimal conditions, this technique can eliminate the need for tumour motion margins while ensuring continuous dose delivery. This technique must be able to do four things, namely determining the tumour position, compensating for time delays in the beam-positioning response, repositioning the beam, and correcting the dosimetry for breathing effects.

While effective, these methods either increase treatment time or rely on surrogates (e.g. implanted fiducial seeds) that may not reliably represent tumour motion. MRLs overcome these limitations by providing real-time tumour visualisation and gating based on direct MRI tracking.

2.4 | Elekta Unity MRL System Overview

Unity by Elekta is composed of a 1.5-T MRI magnet with the static magnetic field (B_0) pointing out of the gantry (Figure 2.2). The magnet is surrounded by a large rotating gantry consisting of a magnetron, a tripole electron gun, and an S-band standing wave accelerating tube (Powers et al., 2022). The design ensures magnetic and radiofrequency (RF) shielding between the MRI and linac components. Magnetic shielding maintains a near-zero field around the electron gun, so electrons can be efficiently injected into the accelerating waveguide (Powers et al., 2022), while the RF shielding prevents waveguide leakage from interfering with MR image acquisition.

Elekta Unity system produces a single 7 MV FFF x-ray beam at a maximum dose rate of 425 MU/min (Powers et al., 2022). Compared to Elekta's Versa HD, which delivers up to 1400 MU/min, Unity's maximum dose rate is significantly lower. This limitation arises primarily from the increased source-to-axis distance (143.5 cm vs 100 cm) and attenuation from the MR components (Powers et al., 2022).

2.5 | Elekta Unity MRL Workflow and CMM Implementation

The MRgRT workflow consists of offline and online components, as illustrated in Figure 2.3, and will be discussed in the following subsections.

2.5.1 | Offline treatment planning

Patients typically undergo both a CT and MR scan for treatment planning. CT-MR image registration is performed where the anatomical structures are contoured on the CT scan and transferred to the MR scan. An MR reference plan is generated on the Elekta Monaco for Unity TPS (Uno et al., 2023). CT scans are still required because MRI does not provide electron density (ED) information, which is necessary for accurate dose cal-

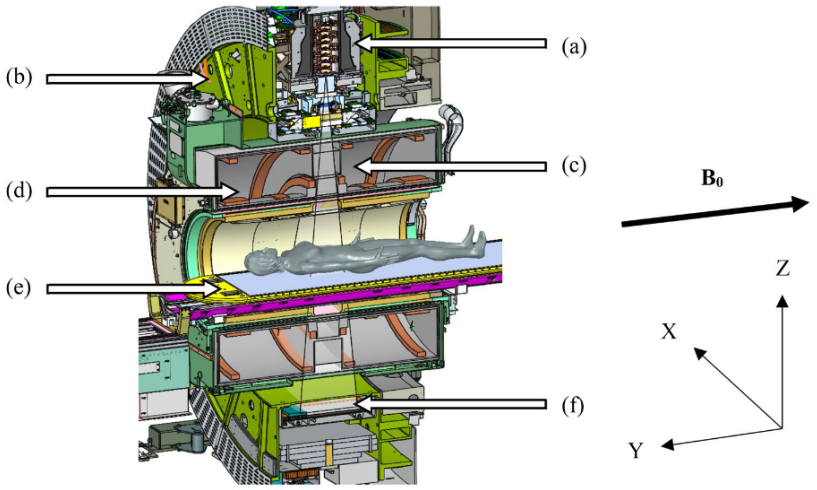

Figure 2.2: A schematic of the Elekta Unity MRL, courtesy of Elekta, showing (a) the straight-through waveguide, (b) the gantry ring, (c) the primary radiation beam passing through (d) the coil system embedded in the magnet cryostat, (e) the patient positioning system and (f) the MVI. Adapted from Powers et al. (2022)

culation. Bulk ED values are assigned to each contoured structure at the planning stage (Winkel et al., 2019). Although MR-only workflows are an active area of development, particularly with synthetic CT methods, they are not yet widely adopted in clinical practice (Autret et al., 2023).

2.5.2 | Online treatment planning

A pre-treatment daily MR scan is taken and fused with the reference MR plan, thus, any differences between the two are evaluated and contours of the anatomical structures are modified (Uno et al., 2023). The reference plan is adapted to the daily MR while the patient is on the treatment couch (Winkel et al., 2019). Plan adaptation on the Unity system is achieved through two workflows in the online Monaco® TPS (Winkel et al., 2019).

Adapt to Position (ATP): The pre-treatment MR scan is matched with the online planning MR using rigid registration (Winkel et al., 2019). The difference that arises

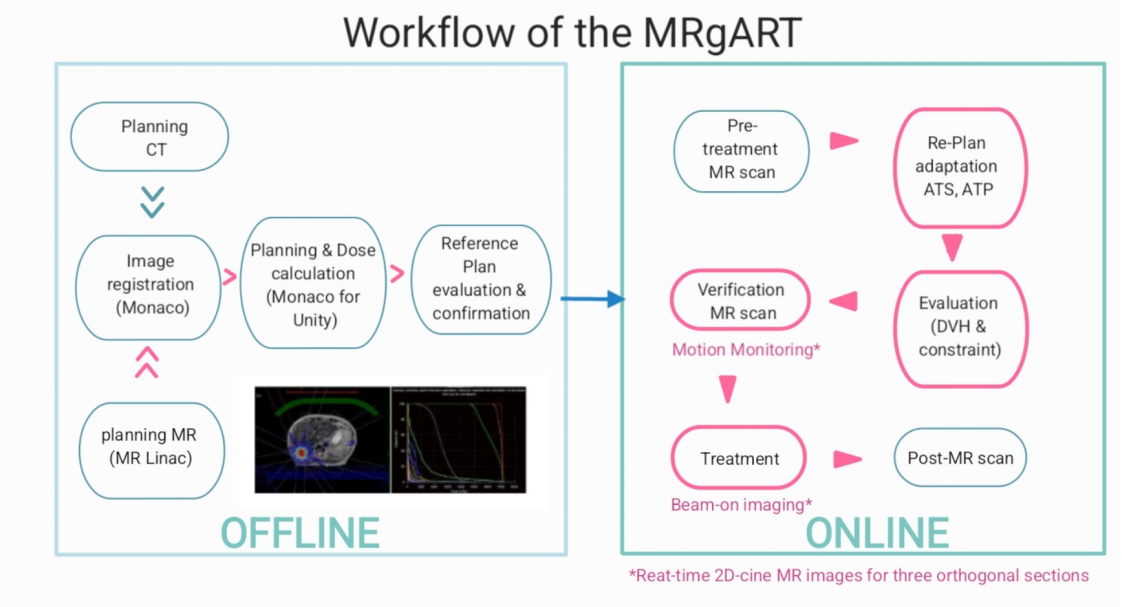

Figure 2.3: Workflow of MRgRT which involves two key steps. 1. Offline planning: A reference plan is created using the MRL system before treatment begins. 2. Online planning: Pre-treatment MR imaging is conducted with the MRL, followed by replanning to address anatomical changes. Adapted from: Winkel et al. (2019)

due to this registration is used so that the isocenter position in the reference data is updated. In ATP, the MLC apertures are adapted correspondingly to align with the new tumour position. This workflow limits the re-optimisation which typically includes MU optimisation and, in some cases, shape optimisation. However, as no contour editing can be done only the original contours on the reference MR can be used. Consequently, the recalculated or re-optimised plan remains constrained by the accuracy of the initial planning scan and its contours (Winkel et al., 2019).

Adapt to Shape (ATS): Similarly to ATP, the pre-treatment MR scan is registered with the online planning MRI. The pre-treatment contours are then automatically transferred to the online planning MRI using deformable registration, rather than rigid as is used in ATP. Contours are edited based on the daily anatomy and full optimisation is possible compared to ATP.

Comparative studies of ATP and ATS workflows have found that ATP performs adequately for minor positional shifts like the prostate, but underperforms when anatomical changes extend beyond rigid motion. In such cases, ATS provides superior CTV and margin coverage (Dassen et al., 2023; Zhou et al., 2024). ATP offers efficiency but risks suboptimal target coverage in more dynamic anatomical contexts.

2.5.3 | Real-Time Motion Management in Elekta Unity MRL

CMM utilises live 2D MR cine balanced turbo field echo (bTFE) imaging sequence which consists of a 1.13 mm $\times$ 1.13 mm pixel resolution, a slice thickness of 5 mm, and a temporal resolution of 200 ms (Smith et al., 2025). These Cine MRI images are dynamic and use two orthogonal planes (coronal and sagittal) to initially detect and track a registration structure, typically coinciding with the target or a correlated surrogate (Uno et al., 2023). The centroid of this structure defines the intersection point of the cine planes, forming the template for subsequent positional monitoring (Uno et al., 2023).

2.5.3.1 | Anatomic Position Monitoring (APM)

The APM system employs an algorithm that calculates the displacement of the registration structure in live images by comparing incoming cine MR images to template images (Rusu et al., 2024). These templates are generated from a short training set of approximately 30 cine MR images acquired at the start of each fraction, extracted as coronal and sagittal slices and aligned to minimise displacement relative to the daily MR volumes (Brown, 2024). Absolute registration is performed once per treatment, using this training set. The resulting template must then be reviewed and approved by the user before proceeding (Corbett, J., 2022). During beam delivery, relative registration is then performed, where each incoming live cine slice is compared to the approved template (Corbett, J., 2022). From this comparison, a displacement vector is derived in all three cardinal axes that describes the movement of the target (Figure 2.4).

A recent Unity study has tested APM performance under both regular and irregular

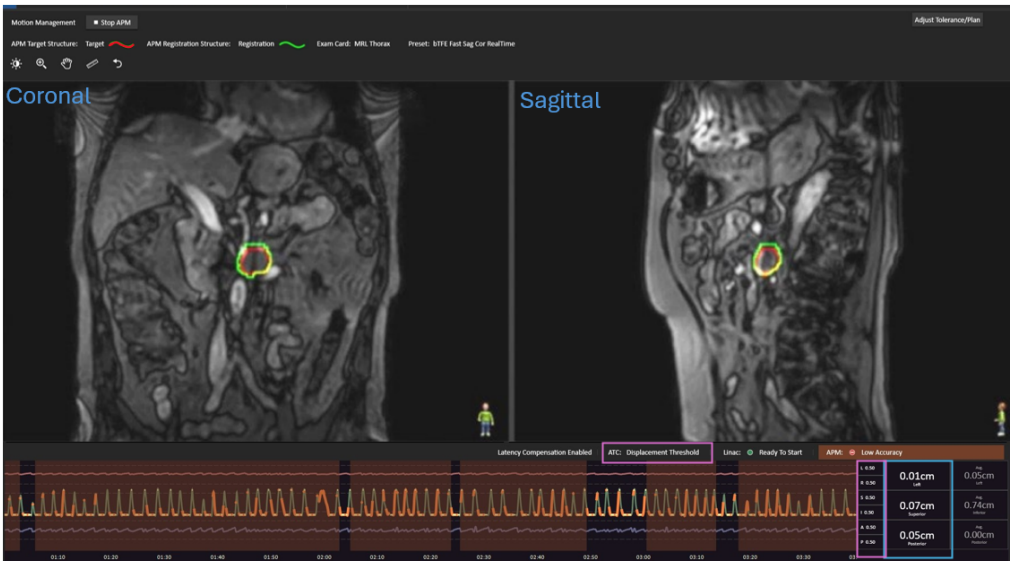

Figure 2.4: Example of APM with ATC displacement threshold on a patient treated with Elekta Unity CMM. The blue box displays the current displacements in the three cardinal axes using the tracked registration structure (yellow contour). The purple box indicates the user defined ATC displacement threshold. The left bottom panel shows the corresponding motion traces with gating decisions and low-accuracy intervals. Adapted from: Brown (2024)

traces using an MR-Safe motion phantom (Modus MRI^{4D} QUASAR phantom) (Smith et al., 2025). They reported $<\pm 2$ mm tracking accuracy for 95% of frames and latencies within tolerances for all waveforms, confirming Unity's robustness to irregular motion.

2.5.3.2 | APM Quality Factors

APM can provide low confidence estimates due to unforeseen circumstances or algorithm limitations. To address this, five quality factors are implemented: (1) large anatomy deformations, (2) through-plane motion, (3) jitter, (4) no-motion detection and (5) drop in registration score detection (Rusu et al., 2024). These factors evaluate various aspects of target movement and image quality to ensure confidence in APM's predictions under various scenarios, as seen in Table 2.1. Beam delivery is prevented if the accuracy is low. Moreover, not all quality factors are enabled at the same time, these depend on the motion management strategies utilised (Corbett, J., 2022).

Table 2.1: Examples of clinical scenarios where quality factors can be triggered.

Quality Factor	Patient Movement	Coughs	Changes in breathing pace	Big inhalations
Large Deformation	✓	✓		✓
Through-Plane Motion	✓	✓		✓
Jitter	✓			
No-motion	✓		✓	
Drop in Registration Score	✓	✓		✓

2.5.3.3 | Anatomic tolerance check (ATC)

ATC uses target tracking to determine if the target exceeds predefined tolerances. This can be performed using a gating envelope defined as either the target itself or an auto-expansion of it (Brown, 2024). Two methods of gating are available: displacement threshold and Volumetric overlap criteria (VOICE) (Brown, 2024).

Displacement threshold: This method employs a box-shaped tolerance in the imaging plane with 0.1mm resolution (Corbett, J., 2022). If the target's displacement exceeds this threshold in any direction within this 2D plane, the beam is turned off.

VOICE: This uses a percentage of target voxels overlapping with the gating envelope (Brown, 2024). If the overlap falls below a specified threshold, the beam is gated off.

Thus, APM is used with ATC to track the target continuously during treatment delivery in all 3 cardinal axes and see if the GTV (target or surrogate) exceeds the PTV (Threshold or envelope used) as seen in Figure 2.5.

2.5.3.4 | Latency

As acknowledged by Elekta (2023b), the primary challenge in this system is latency, which is the time delay between target movement and linac response i.e. how fast the beam can be switched off or on once the target structure moves out or into the gating envelope, respectively. The manufacturer specified latency of Unity is divided between

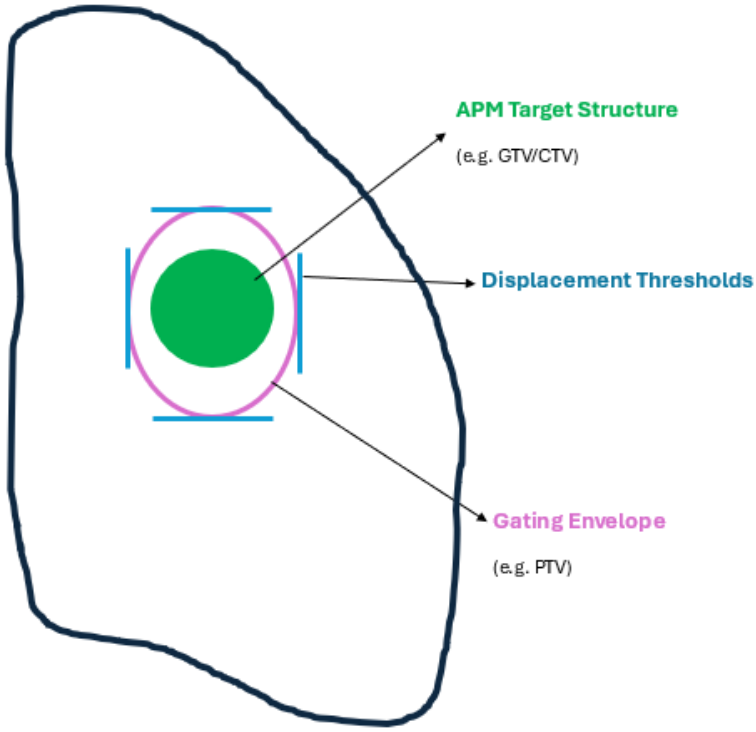

Figure 2.5: Monitoring the Position of the 3D target using either gating threshold or VOICE. Adapted from: Corbett, J. (2022)

two latency types:

Control system latency: The time difference between the instant the target moves into or out of the gating window and the moment the linac's gun modulator is instructed to switch on or off. This is the responsiveness of the gating control system itself. Acceptable latency ranges from –300 ms to +180 ms for beam-on and –220 ms to +180 ms for beam-off (Elekta, 2023b).

End-to-end system latency: The overall delay experienced clinically, which includes the (1) control system latency and (2) the beam ramp-up or ramp-down period. Ramp-up is defined as the time taken from when the gun is requested to start pulsing until 90% of the dose rate is reached, while ramp-down is the time until it falls to 10% (Elekta, 2023b).

Acceptable end-to-end system latency ranges from –200 ms to +280 ms for beam-on transitions and –200 ms to +200 ms for beam-off transitions.

Studies have demonstrated reduction in latency with the use of a prediction algorithm in respiratory-gated RT. Johno et al. (2018) showed using a conventional linac that without prediction, gate on/off delays led to deviations in gating windows, causing irradiation with errors exceeding 2 mm when normalized. By contrast, their prediction-based model reduced root mean square (**RMS!**) error to < 1.5 mm for most breathing traces, thereby improving dose delivery accuracy. This supports the integration of predictive models to maintain dose accuracy during respiratory motion.

2.5.3.5 | Prediction Algorithm

The Elekta Unity predictive algorithm predicts the target's position before it reaches its actual location. The predictive algorithm works by using continuous measurements from the APM values. These measurements form a mathematical motion model, which describes the target's displacement as a function of time (Brown, 2024). As new position measurements are acquired, the model parameters are updated, enabling the system to predict the target's location a few hundred ms ahead in time. This value varies based on the dynamic horizon, which calculates the necessary prediction lead time. This algorithm is used for targets that are expected to have rapid movements for example those located in the thorax.

Its accuracy however, is highly motion dependant, meaning that if the motion of the target is highly irregular, the accuracy of the prediction will be lowered and reliable prediction may not be possible (Brown, 2024).

2.5.4 | Unity's Motion Management Strategies

Motion management is crucial in various scenarios. Elekta Unity offers four strategies: three for respiratory motion and one for non-respiratory motion, which will be dis-

cussed in this subsection and can be visually represented in Figure 2.6.

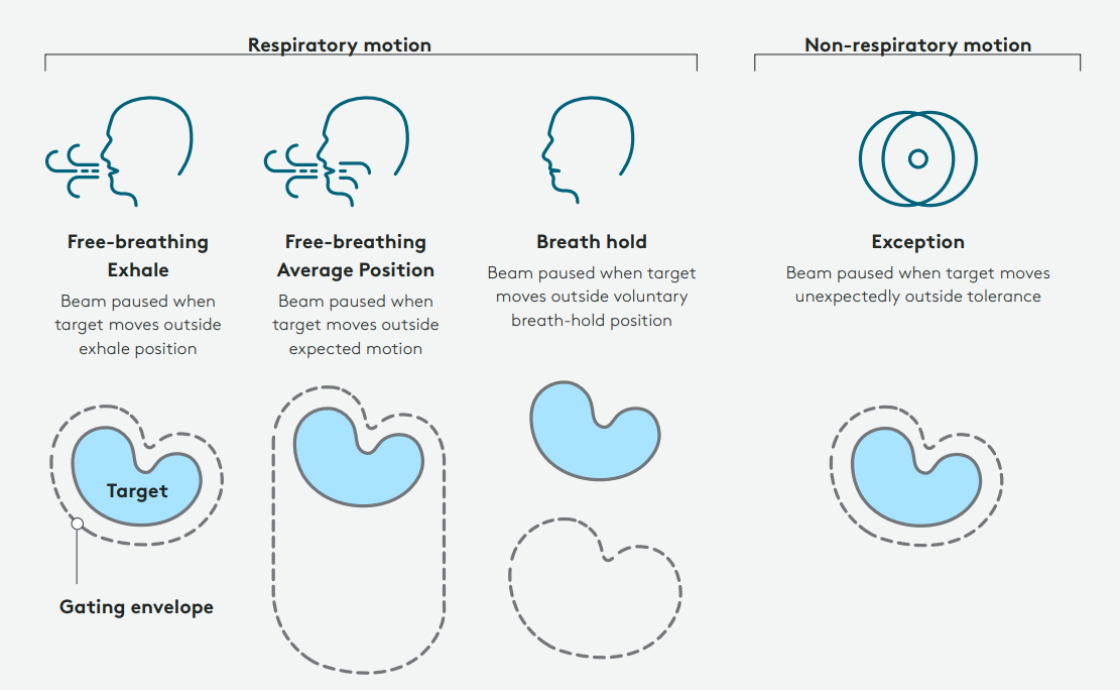

Figure 2.6: Unity's four Motion Management Strategies. Source: Brown (2024)

2.5.4.1 | Respiratory Motion

For free-breathing strategies (average position and exhale), the prediction algorithm (§2.5.3.5) is employed. It cannot be deactivated and requires approximately 25s for training, during which the APM status will show as *low-accuracy* (Corbett, J., 2022).

Free-breathing average: The patient is continuously imaged and treated while breathing freely. Instead of using a traditional ITV margin derived from 4D planning CT, motion is accounted for using real-time tracking of the target's average position during free breathing. Beam delivery is centered around this time-weighted average position, and automatically paused if the target moves beyond the expected range due to unexpected factors (Brown, 2024). This strategy is used for targets exhibiting small to moderate motion amplitude. In addition, it is widely incorporated clinically due to the simple

implementation and one which does not excessively extend treatment times.

Free-breathing exhale: This technique involves imaging and treatment while the patient breathes freely, similar to the free-breathing average (Brown, 2024). The major difference between the two is that the daily MR imaging and radiation delivery are carried out only during the exhale phase (Brown, 2024).

This approach is able to reduce the planning ITV margin compared to the free-breathing average technique, as the beam activates only when the target is within the desired exhale position. However, this increases overall treatment time due to delivery inefficiencies. Despite this, the approach may be particularly beneficial for patients with tumours that exhibit greater positional stability during exhalation such as certain liver or lung lesions as it allows for smaller margins and improved sparing of nearby organs at risk (Brown, 2024).

Breath hold: Involves imaging and treatment during a voluntary breath-hold. The patient holds their breath for 18-30 seconds and the system captures the daily 3D MR scan. Treatment is then delivered during subsequent breath-holds, guided by automated tracking and gating systems. This strategy minimises motion but requires patients to consistently liaise with the clinicians (Das et al., 2024). An extra margin is needed to account for variability between breath-holds. This method is particularly useful when increased lung volume helps reduce radiation exposure to nearby organs, such as moving the heart away from the target. However, it is poorly implemented on Unity as of yet and treatment time may be extended due to patient coaching and recovery periods between breath-holds (Das et al., 2024).

For this strategy, the prediction algorithm is not utilised. This is due to the fact that the target is not expected to move as the patient is holding their breath and the latency associated with the beam gating is minimal in comparison (Brown, 2024). Despite this increase in latency, the treatment accuracy is not expected to be effected significantly.

Therefore, for this strategy, latency compensation becomes disabled.

2.5.4.2 | Non-respiratory Motion

Exception: For targets like prostate tumours that are influenced more by random motion, the exception gating strategy is used (Nicosia et al., 2025). This allows real-time tracking, pausing radiation delivery if the target moves out of tolerance, ensuring precise treatment. Using this strategy will not significantly impact treatment time. Moreover, similarly to the breath-hold, this strategy does not make use of the prediction algorithm as the target is not expected to move significantly during treatment.

2.6 | Respiratory Motion Phantoms

To measure and manage the effects of respiratory motion, a realistic deformable phantom is essential as a gold standard for evaluating the accuracy of treatment delivery (Kim et al., 2016). Typical phantoms can mimic patient breathing patterns in various directions and perform user-defined complex motions (Viel et al., 2015). A key limitation in an MRL environment is that only MR-compatible motion phantoms can be used. Many commercially available respiratory motion phantoms designed for conventional linacs are unsuitable, requiring dedicated MR-safe phantoms that restrict experimental flexibility and increase cost.

Several commercially available MR-compatible phantoms are used in studies aiming to evaluate respiratory motion effects to test certain systems and characteristics of motion management. Various manufacturers on the market can provide such features such as Modus QUASAR^{TM} and CIRS ZEUS which multiple studies have employed (Dunn et al., 2012a; Kron et al., 2011; Lewis et al., 2022).

The Modus QUASAR^{TM} MRI^{4D} Motion Phantom (ModusQA, Ontario, Canada) is designed for quality assurance (QA) in MRL systems (Figure 2.7b) (Modus QA, 2022). It provides programmable SI translational motion over a range of $\pm$20 mm. When oper-

ating using translational motion only, this configuration is referred to as *no twist*. However, the phantom's moving platform can introduce a $\pm 30°$rotation about the longitudinal axis alongside the programmed SI translation when operated using the *twist* setting (Modus QA, 2022). In the standard configuration, the target insert has a 15 mm lateral offset from the rotation axis. Consequently, when operated in *twist* mode, the rotation introduces small superimposed AP/LR displacements in addition to the programmed SI motion. Alternative inserts are available including a centered target (Modus QA, 2022).

In contrast, anthropomorphic phantoms such as the CIRS Zeus include inhomogeneities that mimic lung, bone, and other tissue types are used for realistic patient-like heterogeneity (Figure 2.7a). However, in CIRS Zeus dynamic motion within the phantom is still limited to the dedicated moving cylindrical tumour target insert located in soft tissue, allowing motion in three directions (CIRS, 2019). All other inhomogeneities remain static, thus respiratory-related deformation of these structures cannot be simulated.

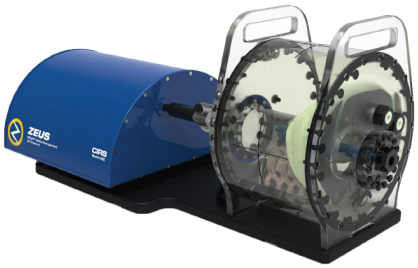

(a) Anthropomorphic CIRS Zeus (Model 008Z) CIRS (2019)

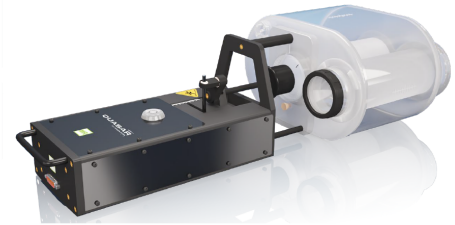

(b) Modus QUASAR^{TM} MRI^{4D} (Modus QA, 2022).

Figure 2.7: Common MR-safe respiratory motion phantoms used in MRgRT

Both phantoms are well-established in the literature and are widely used for commissioning and QA studies, particularly for APM testing and beam latency measurements of the system (Dunn et al., 2012b; Kron et al., 2011; Lewis et al., 2022; Smith

et al., 2025; Snyder et al., 2019). For film-based dosimetric measurements, the Modus QUASAR^{TM} MRI^{4D} is ideal, as it provides dedicated film insert capability, which is not available in the CIRS ZEUS. Other studies have developed research-built, non-commercial, MR safe, tissue-equivalent moving lung phantoms for simulating 3D lung deformations, a feature absent in Modus QUASAR^{TM} MRI^{4D} (Kim et al., 2016).

2.7 | Film Dosimetry

2.7.1 | Principles of Radiochromic Film

Radiochromic film dosimetry is widely regarded as the gold standard for high-resolution, 2D dose measurement in RT QA (Butson et al., 2009; Keshmiri et al., 2025). The most commonly used films are the commercially available Gafchromic^{TM} EBT films. The latest EBT versions have seen a lot of enhancements with EBT3 offering an optimal dynamic range of 0.2- 10 Gy, with improved uniformity and eliminated side orientation effects; EBT4 matches this 0.2 - 10 Gy range, improving signal-to-noise ratio (SNR) and signal stability. The latest EBT-XD offers the widest dynamic range of 0.4 - 40 Gy for high-dose applications such as SBRT (Guan et al., 2023b; Miura et al., 2016).

Radiochromic films provide several advantages including, energy independence in megavoltage photon beams, self-developing response without chemical processing, high spatial resolution for small fields and steep dose gradients, near water-equivalence, wide dynamic range, and stable, re-readable signals with minimal fading (Butson et al., 2009; Devic, 2011).

Radiochromic films consist of a thin polyester base coated with an ultrathin radiation-sensitive layer. This active layer contains colourless microcrystals of a radiation-sensitive monomer dispersed in gelatin (Guan et al., 2023a). The schematic construction of a radiochromic film and an example of an irradiated film are shown in Figure 2.8. When exposed to ionising radiation, the monomers undergo progressive polymerisation, form-

ing polymer chains within the active layer.

The length and density of these polymer chains increase with radiation dose. Thus, they modify the film's optical absorption characteristics, reducing the transmission of light through the active layer proportional to the absorbed dose (Guan et al., 2023a). This effect is quantified as optical density (OD), defined as the logarithm of the ratio of transmitted light intensities before and after irradiation (Eq. 2.1), which is the standard metric recommended in AAPM TG-235.

$$\mathrm{OD} = \log\left(\frac{I_0}{I_T}\right) = \log\left(\frac{P_{\mathrm{unexp}}}{P_{\mathrm{exp}}}\right) \tag{2.1}$$

where, I_0 is the incident light intensity, I_T is the transmitted light intensity through the irradiated film, and P_{unexp} and P_{exp} are the pixel values before and after irradiation (Ashland Advanced Materials, 2019; Niroomand-Rad et al., 1998).

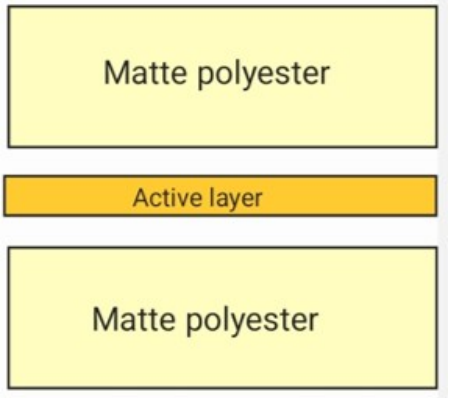

(a) Schematic radiochromic film construction of EBT4. Adapted from: (Soloviev et al., 2017)

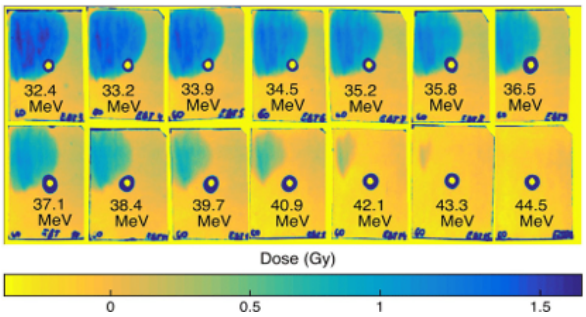

(b) Example of a resulting film following irradiation. Source: (Soloviev et al., 2017)

Figure 2.8: Schematic construction of Gafchromic^{TM} EBT4 construction and an example of resulting films following irradiation

2.7.2 | Calibration Procedures and Scaling Considerations

Each batch of films requires calibration to account for any manufacturing variability in the active layer, which can alter the dose-response relationship (Devic, 2011). Cal-

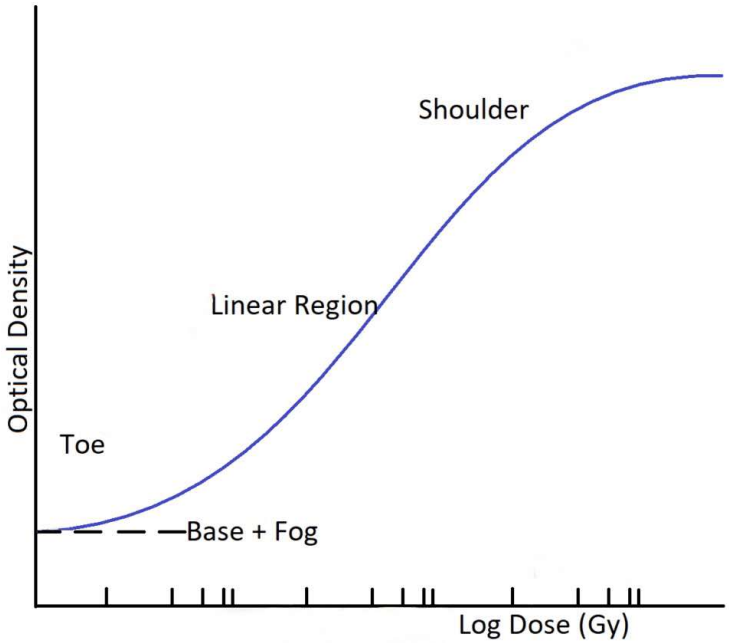

Figure 2.9: A sensitometric (calibration) curve for radiochromic film, showing the characteristic sigmoid relationship between net optical density and absorbed dose and the 3 main regions. Adapted from: (Oncology Medical Physics, 2023)

ibration is performed by irradiating film strips to a set of known reference doses and scanning them under identical conditions to those used for measurement films (Devic, 2011). This ensures that the resulting calibration or sensitometric curve accurately reflects the specific batch characteristics. For radiochromic films, as shown in Figure 2.9 this relationship typically follows a sigmoid-like trend where it has 3 main regions (Devic, 2011). (1) At low doses i.e. Toe region, the change in OD is small and the slope of the curve is shallow. (2) In the mid-dose range i.e. linear region, the slope increases, representing the high-sensitivity region where small changes in dose produce measurable changes in OD. (3) At high doses, the curve reaches a plateau i.e. the saturation limit where additional dose produces little or no further increase in OD (Devic, 2011).

Scaling may be applied during analysis to match measured film doses to a known reference. Lewis et al. (2012) and Reinhardt et al. (2012) reported that applying a global scaling factor between measured and reference doses can improve the agreement of ra-

diochromic film dosimetry results. This approach effectively compensates for small deviations between the calibration curve and film measurement conditions. These include beam output fluctuations or minor setup variations without requiring a complete recalibration, thereby enhancing accuracy, particularly in regions with steep dose gradients (Lewis et al., 2012; Uijtewaal et al., 2024). A common implementation is the *two-point* scaling method, in which the response of an unexposed film and a film irradiated to a high reference dose are used as the scaling limits. A linear scaling factor is then derived so that these two reference points align with their expected values, and all intermediate doses are rescaled accordingly (Lewis et al., 2012; Reinhardt et al., 2012).

2.7.3 | Film Digitisation and Image Analysis Techniques

The shape of the sensitometric curve highly depends on the scanner characteristics. Digitization is typically performed using high-resolution flatbed scanners operated in transmission mode. Commercial flatbed scanners such as Epson Expression 10000XL are routinely used. However, they exhibit lateral response artifacts i.e. non-uniform response across the scan bed that is caused by variations in optical path length and light polarization within the scanner optics (Lewis and Chan, 2015). This leads to systematic dose errors, particularly at the edges of the scan field. Several studies have reported that the magnitude of lateral response artifacts is minimised when films are scanned at the scanner midline, making central placement a simple and effective strategy (Lewis and Chan, 2015).

2.7.4 | Verification of film measurements

Verification of radiochromic film measurements usually involve using the gamma index, a metric that simultaneously evaluates dose difference and distance-to-agreement criteria between measured and calculated dose distributions (Agnew and McGarry, 2016). A point passes if its gamma value, (γ) is <1, with a 2%/2 mm and 3%/3mm being a common clinical criterion. As stated in, Hussein et al. (2017), the gamma value for each point is expressed as:

$$\gamma = \sqrt{\frac{\Delta r^2(\mathbf{r_R}, \mathbf{r_E})}{\delta r^2} + \frac{\Delta D^2(\mathbf{r_R}, \mathbf{r_E})}{\delta D^2}} \tag{2.2}$$

where $\Delta r(\mathbf{r_R}, \mathbf{r_E})$ is the spatial difference between the reference and evaluated points, $\Delta D(\mathbf{r_R}, \mathbf{r_E})$ is the dose difference, and δr and δD are the respective distance and dose difference criteria. The overall passing rate, expressed as the percentage of points with $\gamma < 1$, provides a quantitative measure of agreement between planned and delivered dose distributions. While gamma analysis is widely used, its dependence on chosen criteria (e.g. 2%/2mm vs 3%/3mm) can mask systematic errors, so care is needed when interpreting film results.

This analysis can be done either through the use of in-house scripts (e.g., MATLAB or Python) or by using a commercially available software, with FilmQA Pro and `radiochromic.com` software most widely employed. These tools typically include functions for multi-channel dosimetry, calibration curve fitting, inter-scan variability correction, film profile analysis, lateral response correction, and gamma evaluation (Méndez et al., 2021).

2.8 | Validation techniques of motion management

QA is essential in gated radiation therapy (Brady et al., 2010; Jiang et al., 2008; Niroomand-Rad et al., 1998). Procedures for acceptance, commissioning, and routine QA, including tolerances and frequencies, are well documented (Roberts et al., 2021; Snyder et al., 2019; Woodings et al., 2018, 2021). While published validation studies specific to the Unity system remain limited, the following section reviews the general methods used to evaluate gating systems across different platforms.

In the case of respiratory breathing, the validation of motion management and gated treatments typically involves acquiring patient-derived waveforms, created through respiratory motion phantom software, or third party waveforms provided by the manufacturer (Berson et al., 2004; Cui et al., 2014; Dunn et al., 2012b; Freislederer et al., 2015;

Han et al., 2019; Lachaine and Falco, 2013; Lamb et al., 2017; Lee et al., 2013; Wen et al., 2018).

2.8.1 | Dosimetric Measurements

A widely reported approach in IMRT QA to assess dosimetric accuracy under motion involves the use of radiochromic film or ion chambers placed in motion phantoms (Oliver et al., 2008; Wang et al., 2012). Three standard treatment scenarios are planned and delivered, which are divided as follows: (1) static delivery to a stationary target (to be used as reference), (2) delivery during motion without gating (to characterise blurring/penumbra broadening), and (3) delivery during motion with gating or tracking enabled (to quantify recovery of the planned dose distribution) (Lee et al., 2013; Oliver et al., 2008; Viel et al., 2015; Wang et al., 2012). Films are then compared to the planned distribution or static reference using the gamma index metric to report pass rates and identify any patterns at field edges and high-gradient regions.

Ungated motion degrades this film agreement as it smears dose in the direction of motion. This reduces central axis (CAX) dose and enlarges the penumbra. On the other hand, gating helps recover this agreement close to the static reference. For regular periodic waveforms (e.g., sinusoidal or cosine based), gated deliveries achieve gamma pass rates $\geq$99% at 3%/3 mm, and remain >99% under more stringent criteria such as 3%/1.2 mm (Brady et al., 2010). In contrast, same plans delivered without gating yield substantially lower pass rates (84.7%) due to motion-induced blurring. Similarly, Lamb et al. (2017) tested sinusoidal trajectories of varying frequency on the MRIdian MRL and demonstrated that gating improved pass rates from 22-59% in the ungated state to 97.8% with gating enabled.

When the breathing pattern changes from a regular periodic trace to an irregular trace, film agreement worsens unless the motion management system has an algorithm robust to variability. Unplanned respiratory events, such as coughs or short breath-

holds, further challenge motion management. Han et al. (2019) showed that frequent short interruptions, including simulated coughing, did not significantly degrade gated film agreement, with gamma pass rates maintained above 95% at 3%/3 mm. Other studies that introduced phase shifts and irregular respiratory traces observed a gamma pass rate of 95% gamma pass rate at 3%/3 mm in the gated condition compared to $\geq$99% in the regular waveforms (Nioutsikou et al., 2008). Cui et al. (2014) found that frequent beam interruptions on an Elekta Synergy linac did not degrade gated dosimetry, with all films achieving >99% pass rates at 3%/3 mm.

In particular, Nioutsikou et al. (2008) demonstrated that a temporal offset of 0.5–1.0 s between an external respiratory surrogate, in this case an infrared reflective marker block, and the internal tumour position produced systematic localisation errors of up to 4 mm. Such mismatches highlight the potential for gating uncertainties in conventional linac systems, where reliance on external surrogates may compromise dosimetric accuracy. This surrogate–tumour mismatch limitation does not exist in Elekta Unity, where real-time continuous imaging of the target is available. Moreover, Unity's IMRT delivery naturally includes brief beam interruptions during segment changes and gantry motion, which could stand-in for the beam interruptions reported by Han et al. (2019). Unity-specific studies for instance Smith et al. (2025) reported >97% gamma pass rates (3%/2 mm) under both regular and irregular traces using the MRI^{4D} QUASAR phantom, confirming Unity's robustness to irregular motion.

The gating window used also affects the resulting dosimetric measurements and, consequently, the gamma pass rates. A narrower gating window sharply improves dosimetric accuracy by minimizing residual blurring and has significantly higher gamma pass rates. However, this tighter control inherently reduces plan delivery efficiency and prolongs treatment time (Pepin et al., 2011; Short, 2018). Conventional linac studies have quantified this trade-off. Shiinoki et al. (2016) tested gating windows of 2-10 mm with a regular waveform on a film-equipped phantom. Windows $\leq$ 4 mm had $\geq$ 90% gamma pass rates (2%/2 mm) and closely matched static delivery, while $\geq$ 6 mm

produced visible blurring and pass rates < 90%. Similarly, Pepin et al. (2011) and Short (2018) showed that narrow windows (< 50% duty cycle) achieved $\geq$ 95% pass rates even at stringent 1%/1 mm criteria. However, this improvement in accuracy was accompanied by substantially prolonged treatment times ranging fom 5 to 7 times longer than ungated delivery.

This trade-off is particularly relevant for MRL, where continuous cine-MR allows tighter gating windows than conventional systems. However, excessive narrowing of the window may result treatments clinically impractical due to reduced delivery efficiency. In practice, MRL studies have mainly employed fixed thresholds (such as gating thresholds and VOICE limits on Unity) rather than exploring how varying these parameters affects dosimetric accuracy and treatment efficiency. For instance, Lamb et al. (2017) reported robust gamma performance using a 3 mm displacement window with $\pm$10% tolerance, demonstrating that tight gating is feasible on MRIdian MRL. On Elekta Unity, Smith et al. (2025) used a 5 mm PTV expansion, effectively tying the gating window to the PTV boundary, and achieved >97% gamma pass rates for regular waveforms. While gating performance has been demonstrated at fixed thresholds (e.g. VOICE of 95% or a 3 mm displacement window), no published study has systematically explored the impact of varying these parameters on film-based accuracy and treatment time on Elekta Unity.

2.8.2 | Latency

For the Elekta Unity, gating latency can be measured using a direct approach. This is done by recording the beam-control signal provided by the linac, offering high temporal accuracy without the need for external detectors (Smith et al., 2025; Snyder et al., 2019). The MRI^{4D} QUASAR motion phantom (§2.6) features an interface that collects beam-control signals from the radiation delivery system and gating signals from the motion phantom without additional instrumentation. This approach was followed by Smith et al. (2025) on an Elekta Unity MRL which showed latency values to be within

specification. Similarly, for the ViewRay MRIdian system a direct approach is taken to record the gating latency (Kim et al., 2021).

On other IGRT platforms or conventional linacs, this signal is not readily available, so alternative direct or indirect methods have been used. Direct approaches include connecting an oscilloscope to both a motion phantom trigger and the linac's pulse signal, with the delay between traces defining the latency (Green et al., 2018; Saito et al., 2018). Indirect approaches use dosimetric detectors such as film, ion chambers, or diodes to detect the actual radiation transition, comparing this with the phantom trigger to estimate latency (Bertholet et al., 2019; Wiersma et al., 2016). Direct approaches however are preferred as they depend on the timing the actual beam start/stop via the gun/beam-control signal. This results in millisecond precision rather than making use of dosimetric detectors which reduce this precision.

2.9 | Conclusion

A critical and systematic review of the literature associated with motion management in MRgRT, with a focus on the Elekta Unity MRL, has been presented in this chapter. While gated delivery has been shown to be feasible and robust at fixed thresholds, the effects of varying gating parameters on dosimetric accuracy and treatment efficiency remain largely unexplored. Furthermore, most studies focus on regular motion patterns, leaving uncertainties for irregular respiratory traces. These gaps underscore the need for systematic investigations, which will be addressed in this study. The research methodology is presented in the next chapter.

3

Research Methodology

3.1 | Introduction

This chapter presents the methodologies utilised for data collection and the analysis conducted on the gathered data. In carrying out this project, it is assumed that the Elekta Unity MRL operated at optimal mechanical and dosimetric performance, as determined by the routine quality control (QC) programme carried out clinically.

3.2 | Research Approach

A Quantitative and post-positivism (experimental) approach was taken for this research.

Quantitative methods offer a high level of control over variables, enabling the isolation of specific variables, and making it possible to determine if a potential outcome is viable. Therefore, any conclusions drawn are specific. Hence, the collection of numerical data for APM accuracy, beam gating latency measurements, and film dosimetry relied on measurable outputs, that contribute to a quantitative research approach. Unlike qualitative methods, it allows other investigators to replicate and verify the results obtained.

3.3 | Research Strategy

The research strategy employed in this study involved experimental testing. The primary aim of this study was to commission and validate the CMM system by conducting a comprehensive series of tests designed to simulate clinical conditions that extend beyond standard but limited testing conditions. This would enable a detailed characterization of the system's performance and thus, potentially identify any limitations. This process was supported by the commissioning of the Modus QUASAR^{TM} motion phantom to ensure its accuracy and reliability as a simulation tool. In addition, the software outputs were indirectly confirmed through independent calculations in Excel, thereby extending the statistics and providing confidence in both the phantom and its analysis platform.

This study adopts a prospective approach. This allowed for pre-planned acquisitions and controlled motion parameters, enabling an evaluation and subsequent analysis on the influence of waveform characteristics and gating strategy on system performance.

3.4 | Data Collection Technique

Data was collected from audit log files stored within the Elekta Unity CMM system as well as through the analysis software (Modus pResp software V5.0.2) available from the Modus QUASAR^{TM} motion phantom. Waveforms for the different Unity strategies were obtained from three sources: (1) the manufacturer-provided waveform library, (2) derived from supplementary material provided with published studies (Smith et al., 2025) and downloaded from the journal's website, and (3) custom waveforms created by modifying data from the first two sources using the Modus software. Waveforms taken from breathing traces during patient treatments were not used in this study.

From these sources, systematic and reproducible waveforms were selected to ensure

controlled testing conditions. This approach allowed consistent replication of motion patterns across repeated trials, facilitating an accurate evaluation of the MRL system's performance in scenarios involving repeated beam gating in response to a moving target. Experimental conditions were changed systematically with increasing complexity in breathing frequency and amplitude building up to complex patient-like waveforms.

3.5 | Data Collection Procedure

Within this section, the data collection process will be explained in detail. The overall workflow followed throughout this study is outlined in the flowchart shown in Figure 3.1.

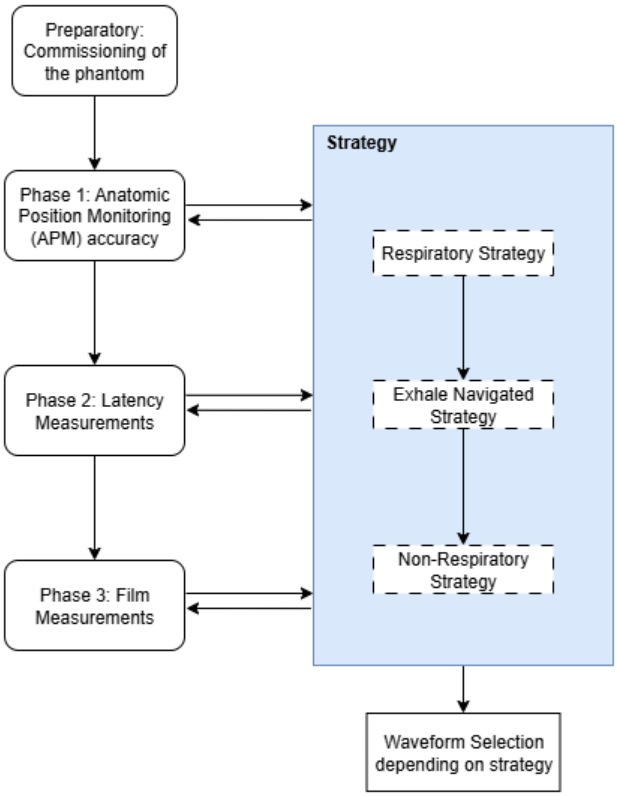

Figure 3.1: Flowchart of the methodology.

3.5.1 | Selection of Motion Management Strategies

The initial project scope included a comprehensive evaluation of APM, latency, and film dosimetry across all four Unity gating strategies. As the project progressed, it became clear that the experimental workload encompassing planning scans, treatment plan preparation, and individual measurements was too time intensive to complete within the available timeframe. This required a re-evaluation and reprioritisation of the work.

- The respiratory strategy was considered a priority as it is being continuously implemented in clinical practice and extended to a variety of treatment sites. Therefore, this study aimed to rigorously evaluate its performance.
- The exhale-navigated strategy was considered the next desired priority due to its potential clinical benefit. However, as detailed in the limitations of this study (§3.9), it could only be tested up to the APM stage. Despite repeated attempts and consultation with an Elekta clinical innovation specialist (L. Fogaça, personal communication, 13th March 2025), unresolved technical issues prevented further testing.
- The non-respiratory exception gating strategy was considered important as it is also being implemented in clinical practice. However, another parallel research study tested this strategy in a more clinically oriented evaluation (Micallef, 2025). Thus, testing was limited to a small set of systematic QC testing conditions that were considered to be within the scope of this project.
- Finally, the DIBH strategy was considered the lowest clinical priority and was excluded early in the project. This is because it is not currently used clinically in SAMOC, with no plans for implementation in the near-term future, making it a significantly lower clinical priority.

It is to be noted that all four Unity gating strategies are built on the same underlying algorithms, so their fundamental performance characteristics are expected to be

consistent. In particular, APM accuracy is algorithm-driven and should therefore be independent of the selected gating strategy. Likewise, latency performance is expected to be stable across strategies. For this reason, differences in gating strategy are not anticipated to affect the baseline commissioning results. Nonetheless, it would have been valuable to confirm these expectations as part of the validation process.

3.5.2 | Preparatory: Commissioning of the Modus QUASAR™ Phantom

The APM QC procedure is based on comparing the target position reported by the CMM system (as recorded in the audit log exported from the Unity Data Processing PC (DPPC)) against the programmed ground truth position determined by the Modus pResp Quasar software. This assumed ground truth is derived from the phantom's programmed motion profile, using the mathematical relationships given by the manufacturer (Table 3.1). These formulas apply for both available modus settings: *no-twist* (purely translational) and *twist* (translation and rotation) (Figure 3.2).

***No-Twist* Operation**	***Twist* Operation**
$x(w) = -f$	$x(w) = -f \times \sqrt{0.75 + \left(\frac{w}{40}\right)^2}$
$y(w) = 0$	$y(w) = \frac{f}{2} \times \sqrt{1 - \left(\frac{w}{20}\right)^2}$
$z(w) = w$	$z(w) = w$
$\theta(w) = 0$	$\theta(w) = \sin^{-1}\left(0.5 \times \sqrt{1 - \left(\frac{w}{20}\right)^2}\right)$

Table 3.1: Mathematical formulas describing programmed phantom motion for *No-Twist* and *Twist* operations. where f is the target lateral offset (0 mm or 15 mm), w is the programmed 1D waveform position along the SI axis (-20 mm to +20 mm), $x(w)$, $y(w)$, and $z(w)$ are the target positions along the left-right (LR), anterior-posterior (AP), and SI axis respectively (mm), and $\theta(w)$ is the rotation about the longitudinal (z) axis (degrees) (Modus QA, 2022).

Because all subsequent tests in this study are fundamentally based on this Modus-

reported ground truth, the MRI^{4D} Modus QUASAR^{TM} physical positional accuracy was first verified. This was performed using the phantom's cylindrical insert containing a Ø3 cm target positioned with a 15 mm lateral offset (Figure 3.3).

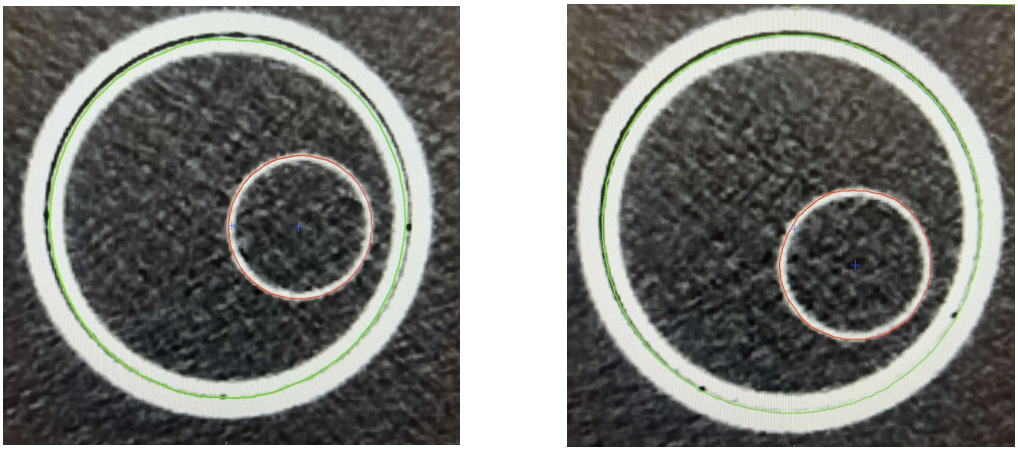

Figure 3.2: Ø3 cm target with 15 mm position offset measured at +20 mm and 0 mm, with the 0 mm position corresponds to the 30°rotation (*Twist*). The green contour outlines the cylindrical insert, the red contour outlines the target, and the blue cross markers indicate the centres of both the cylinder and the target structures.

The phantom was scanned on the Aquilion^{TM} LB CT scanner at SAMOC (Figure 3.3) using a 1 mm slice thickness. Scans were acquired with the target positioned at the central 0 mm reference position, followed by additional scans at $\pm$5 mm increments until the maximum displacement of $\pm$20 mm. This was repeated twice, once in the *twist* setting, and once with the *no twist* setting (Figure 3.3b and c).

The CT scans were imported into Monaco® TPS (Elekta AB, Stockholm, Sweden). Each scan was automatically registered to the 0 mm reference scan using translation-only fusion. From this registration, the translational displacements in the X (LR), Y (AP), and Z (SI) directions were compared with the expected ground-truth positions (Table 3.1), and the positional errors in each direction were quantified.

In addition, the physical accuracy of the target's lateral offset from the centre was

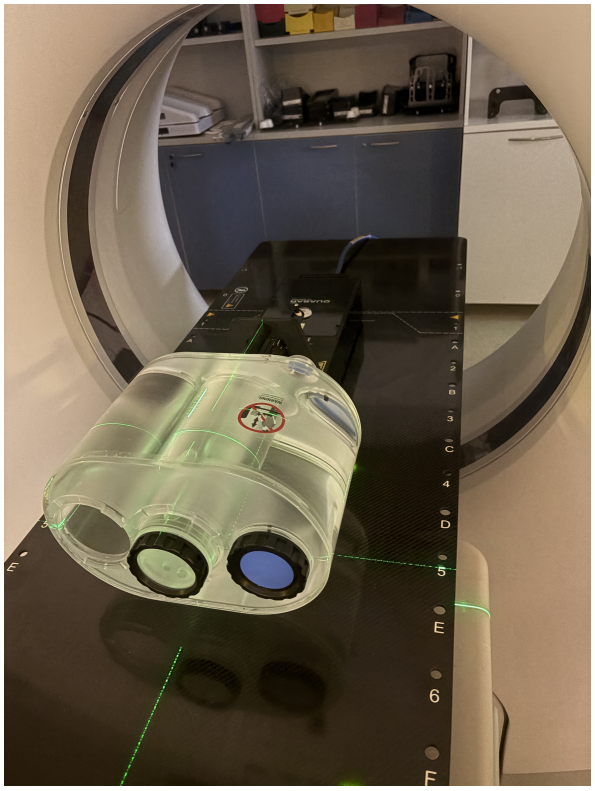

(a)

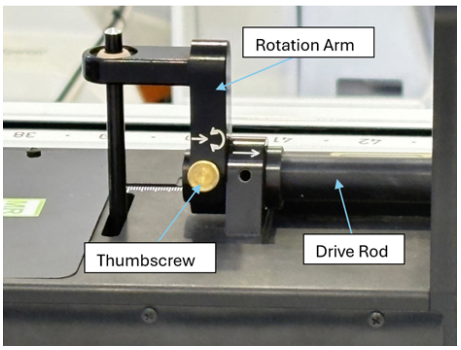

(b)

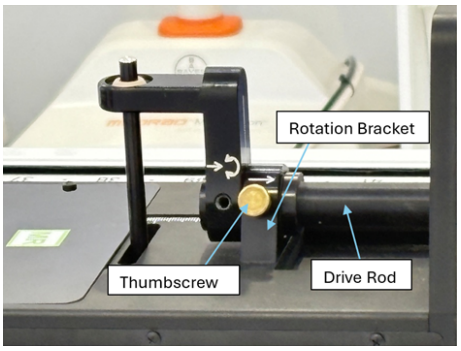

(c)

Figure 3.3: (a) Modus QUASAR^{TM} phantom positioned at 0° (posterior-anterior) on the Aquilion^{TM} LB CT scanner, aligned using room lasers prior to scout acquisition for positional accuracy evaluation.(b) *Twist*: Thumbscrew inserted in the rotation arm for combined translation and rotation. (c) *No Twist*: Thumbscrew inserted in the Rotation Block to allow translation only.

verified to be 15.0 mm by manually contouring both the spherical target and the cylinder structure, and calculating the offset between the respective centres (Figure 3.2).

Following verification of the Modus-reported ground truth, testing was conducted in accordance with departmental QC procedures, closely following the Elekta acceptance testing.

3.5.3 | Selection of Waveforms for APM and Latency Testing

In preparation for designing the APM and latency tests, it was necessary to select a series of waveforms to test, challenge and evaluate the selected gating strategies. These waveforms were selected from; the manufacturer-provided library, literature (Smith et al., 2025), and custom-made. The selection criteria included (1) variability in amplitude, (2) range of breathing rates , and (3) irregular (non-periodic) waveforms to reflect a range of clinically relevant motion patterns. The specification for each waveform used under each category can be summarised in Table 3.2 and visualised in Figure 3.4. Different waveforms were applied across the three clinically relevant gating strategies as follows:

Respiratory Strategy: A number of waveforms denoted as Respiratory in Table 3.2 were tested.

Exhale Navigated Strategy: Only clinically relevant waveforms were taken into consideration (Table 3.2). For a single test case, two distinct waveforms were used to investigate a clinically relevant scenario in which the patient's breathing pattern changes between template acquisition and treatment delivery. The waveform labelled as Typical 1 for the reference and daily MR scan, and Fast Typical 7 for the template acquisition. This approach simulated significant variation in respiratory motion while maintaining physiologically realistic patterns.

Non-Respiratory Strategy: For exception gating, where no predictive algorithm is available, the system depends solely on real-time APM tracking. High frequency waveforms (> 11 bpm and 10 mm amplitude) resulted in persistent *low accuracy* states, making treatment delivery infeasible. To ensure valid gating behaviour, a fixed 10 mm amplitude was maintained while the breathing rate was limited to 10 bpm and 5 bpm i.e. the highest frequencies at which the system could maintain acceptable tracking accuracy for uninterrupted beam delivery (Table 3.2).

Source	Waveform Name	Specification		Strategy Used
		Maximum Amplitude (mm)	Bpm	
Manufacturer	Typical 1	15	11-20	Respiratory & Exhale
	Typical 8	15	9-12	Respiratory
Manufacturer	Fast Typical 1*	15	22-40	Respiratory
	Fast Typical 7	15	22-32	Respiratory & Exhale
Manufacturer	Irregular 8	15	30-56	Respiratory & Exhale
Smith et al. (2025)	Irregular 12 bpm	14	10-14	Respiratory
Smith et al. (2025)	Cos^6 10 bpm	15	10	Respiratory
	Cos^6 14 bpm	15	14	Respiratory
	Cos^6 18 bpm	15	18	Respiratory
Custom	Cos^6 30 bpm	15	30	Respiratory & Exhale
	Cos^6 50 bpm	15	50	Respiratory
Custom	Sin 5 bpm	10	5	Non-Respiratory
	Sin 10 bpm	10	10	Non-Respiratory & Exhale

Table 3.2: Waveform specifications for each category. Bpm = breaths per minute. *This waveform was created using Typical 1 with a scaling factor of 0.5.

3.5.4 | Phase 1: Anatomic Position Monitoring Accuracy

The APM system was tested to verify if, in line with the manufacturer's specification, 95% of sampled points remain within ±2 mm of the Modus QUASAR™ Phantom recorded (ground-truth) position across all three cardinal axes, for various clinical scenarios and conditions that differ from the routine QC tests[1] (Elekta, 2023b). To track the target in the three cardinal axis *twist* setting was enabled on the Modus QUASAR™ phantom.

Standard Monthly APM QC procedures were conducted prior to each measurement

[1] In the current QC, APM accuracy is assessed using a single regular waveform trace (a sinusoidal trace at 10 bpm with a ±19 mm amplitude)

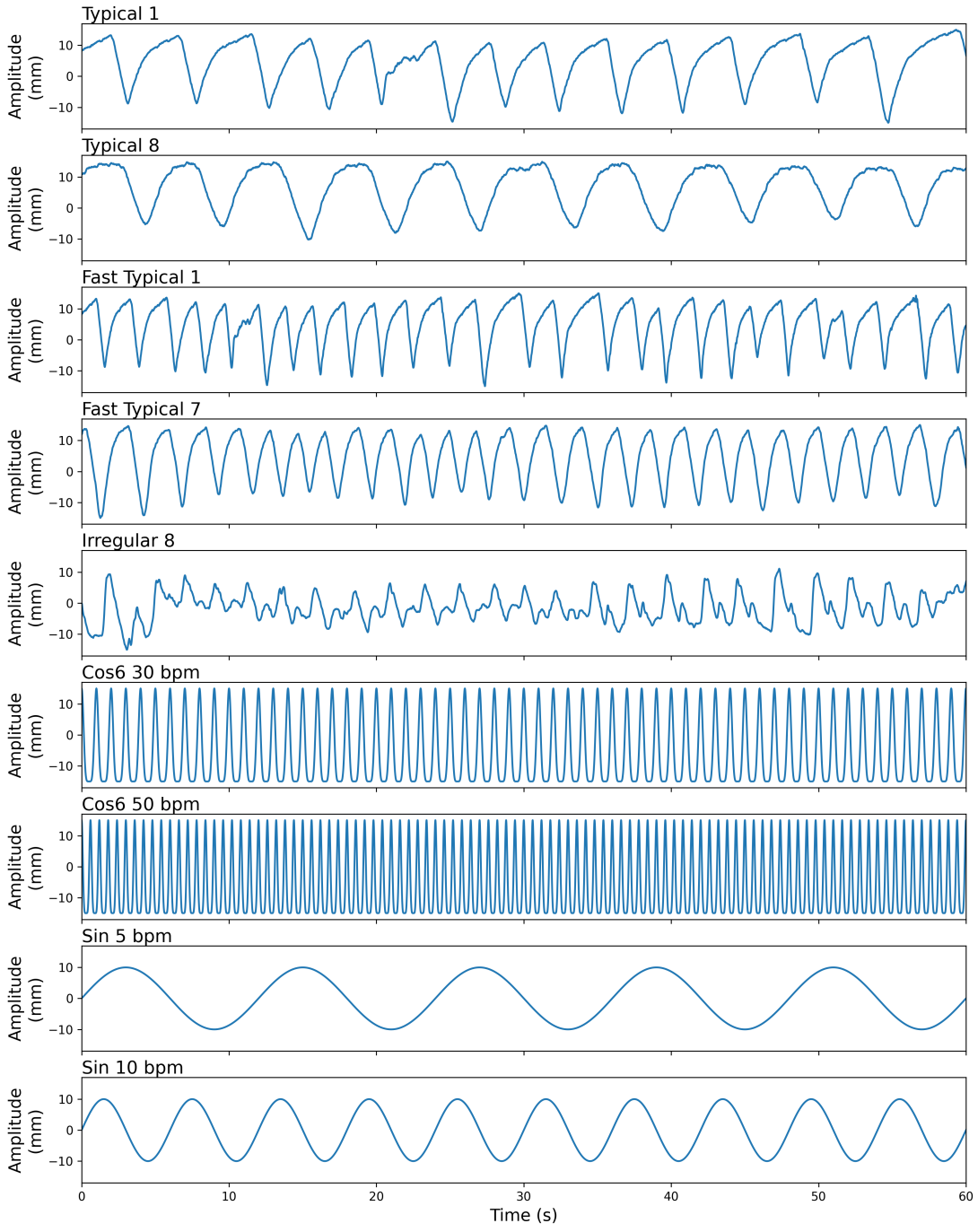

(a)

Continued on next page.

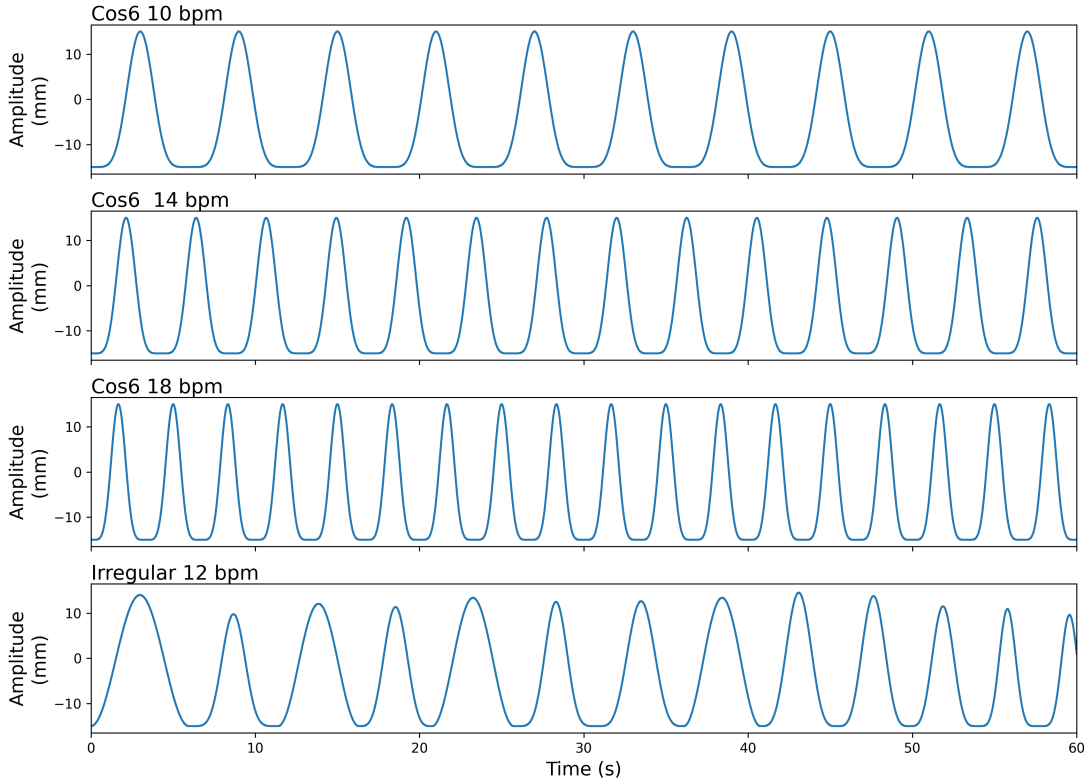

(b)

Figure 3.4: One-minute time series of the waveforms utilized for this work. (a) These are the waveforms selected from the manufacturer-provided library (b) These are waveforms derived using supplementary material from literature (Smith et al., 2025). bpm = breaths per minute.

session to provide a consistent benchmark and ensure confidence in the validity of the results. All other APM tests were performed in accordance with the standard clinical workflow, as would be performed for an actual patient. The reference plan used for system setup was a single beam 3DCRT plan which was not delivered during APM accuracy testing since it only required tracking of the target. The planning MR and template acquisition workflow was as follows:

- For the respiratory strategy, the planning and daily MR were acquired with the target stationary, while the template was acquired with a slight movement of ± 0.2 mm at 15 bpm. A total of 11 waveforms were tested (Table 3.2).
- For the exhale-navigated strategy The planning MR was acquired with the target held stationary at 1 cm inferior displacement, while the template was acquired

using the dynamic waveform that was going to be tested (Table 3.2). A total of 7 waveforms were tested.

- For the non-respiratory strategy both the planning MR and the template were acquired with the target stationary. A total of 2 waveforms were tested.

Moreover, for all the selected waveforms and strategies ATS workflow was performed on the daily MR for exact fusion with the planning scan, as used clinically and as described in literature (Winkel et al., 2019).

Each APM measurement was allowed to run for a minimum duration of 5 minutes before ending the session. The resulting audit log files from the Unity DPPC were then extracted and analysed in Modus pResp Quasar software against the programmed ground truth motion trace(Figure 3.5). This allowed evaluation of APM accuracy in the three cardinal directions.

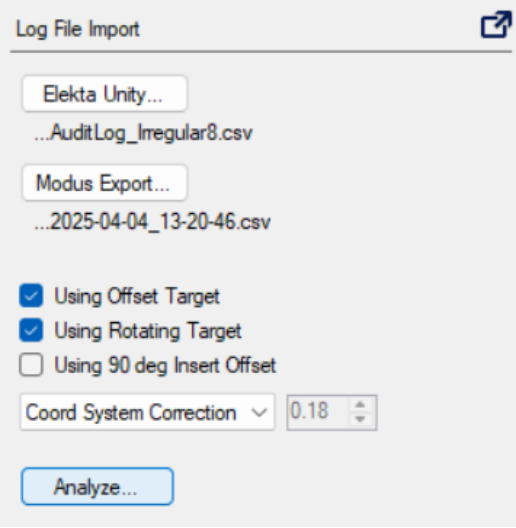

Figure 3.5: Modus QA software interface for log file import, showing the selection of the CMM audit log (Elekta Unity) and the Modus export file containing the programmed ground truth. The selected options indicate analysis using the offset target and rotating target configuration.

3.5.5 | Phase 2: Latency Measurements

Latency performance was evaluated to ensure that beam delivery transitions occur within acceptable time thresholds under varying conditions and strategies. All latency measurements were performed using a simple single beam 3DCRT plan, rather than an IMRT plan, to avoid inter-segment pauses and gantry motion pauses inherent to IMRT delivery. This ensured that only gating-related beam on/off transitions were captured and analysed by the Modus system.

In the Elekta acceptance testing and departmental QC procedures, latency and APM accuracy are tested separately, where unlike APM testing, the *no twist* setting on the Modus QUASAR^{TM} phantom is used for latency testing but a separate planning MR and reference plan is required for *no twist* mode. In this study, latency testing was initially also intended to be carried out separately, once the APM accuracy testing had been completed. However, at that stage, in view of the substantial time required to obtain new planning MR scans and repeat all planning preparations for the *no-twist* setting, an alternative combined method was developed in which latency could also be assessed using the same APM *twist* setup and reference MR scans and plans. This was achieved by adjusting the displacement gating thresholds such that in the SI direction the displacement gating threshold was retained at $\pm$5 mm, whilst for the LR and AP directions, the displacement gating thresholds were increased to $\pm$10 mm. This effectively suppresses gating beam holds for phantom motion in the LR and AP directions. Thus, latency testing procedure could be carried out in parallel with the same ATS and template acquisition workflow employed during APM testing. The same set of simulated waveforms used in the APM analysis were applied (Table 3.2).

The linac beam on/off signal was obtained through the latency module's analog input of the Modus QUASAR^{TM} control system, which sampled at 2 kHz without digital filtering (Figure 3.6) (Modus QA, 2022). The plan MUs were manually set to the maximum allowed by the Monaco TPS (8000 MU) to ensure sufficient beam-on time to

encompass both a minimum of 5 min delivery time for APM testing, as well as to capture a minimum 100 beam-gating events per waveform to ensure statistical reliability for the latency tests (as per method described in Smith et al. (2025)).

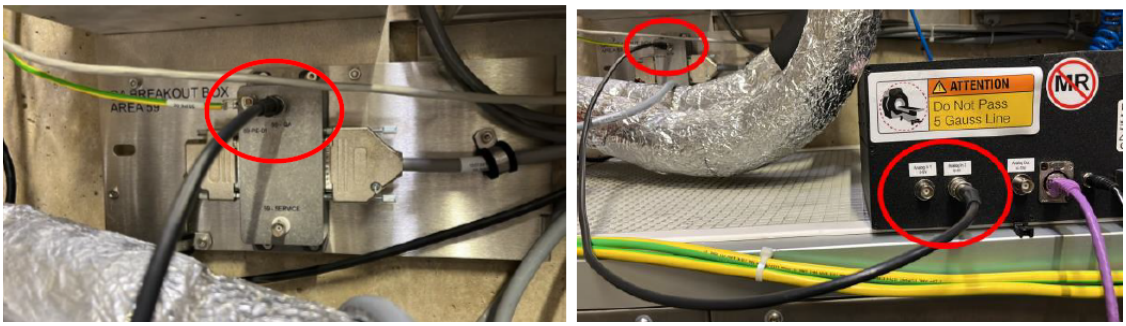

Figure 3.6: Modus control Unit connected to the breakout box on the wall i.e. Linac signal to detect the trigger pulse. Source: Modus QA (2022)

3.5.6 | Phase 3: Film Measurements

Prior to exposing the calibration films, an output constancy check of the linac was performed using the standard departmental dosimetry procedures to confirm that the output was within 1% of the expected dose rate of 1cGy/MU under reference isocentric conditions (10×10 cm^2 field size, 5 cm depth, gantry angle 0°) using a solid water phantom (Figure 3.8).

3.5.6.1 | Calibration, Scaling, and Film Irradiation

A set of 8 Gafchromic EBT4 film calibration strips (Ashland, Bridgewater NJ, USA; LOT# 10042401) with dimensions of 50mm $\times$ 175mm were irradiated to a range of doses (0.63, 1.25, 2.5, 5, 7, 10, 14 Gy) using the solid water phantom (set up in Figure 3.7b and c) under reference isocentric conditions (10×10 cm^2 field size, 5 cm depth, gantry angle 0°) with the film at isocentre height (Figure 3.7a). To ensure reproducibility, alignment crosshairs and a drawn calibration strip outline on the solid water phantom plate were used to position the film consistently across irradiations. In addition, scaling films (7 Gy and 10 Gy) were irradiated at the beginning and end of each measurement session to bracket the dosimetric measurements. Calibration was generally performed at the

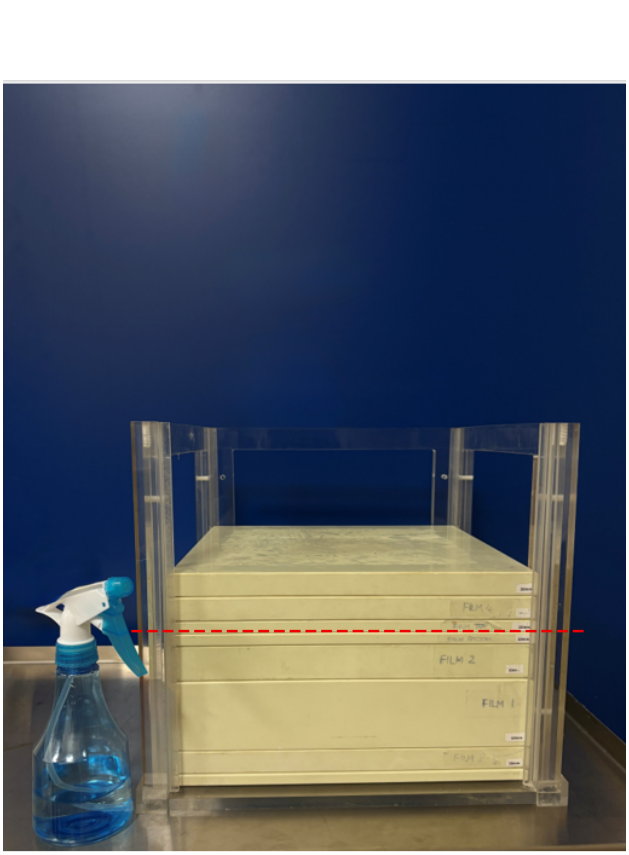

(a)

(b)

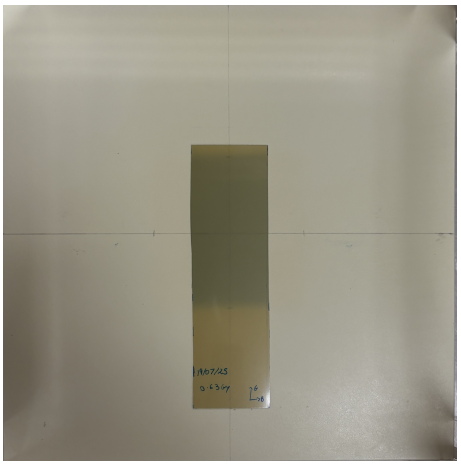

(c)

Figure 3.7: (a) Solid water phantom with the red dotted line indicating the isocentric height. For output constancy check it was modified to introduce a 2 cm Solid Water slab with a Farmer chamber cavity in place of the two 1 cm slabs that sandwich the film strip. Water spray bottle for reducing air gaps. (b) Solid water plate with drawn calibration strip outline (50mm $\times$ 175mm) and alignment crosshairs, ensuring reproducible film positioning. (c) Gafchromic EBT4 film placed within the plate, irradiated with a known dose (0.63 Gy).

middle of the measurement session to account for potential variations in film OD over the measurement session duration.

For film irradiation, the Modus QUASAR^{TM} phantom was used with the MRI^{4D}

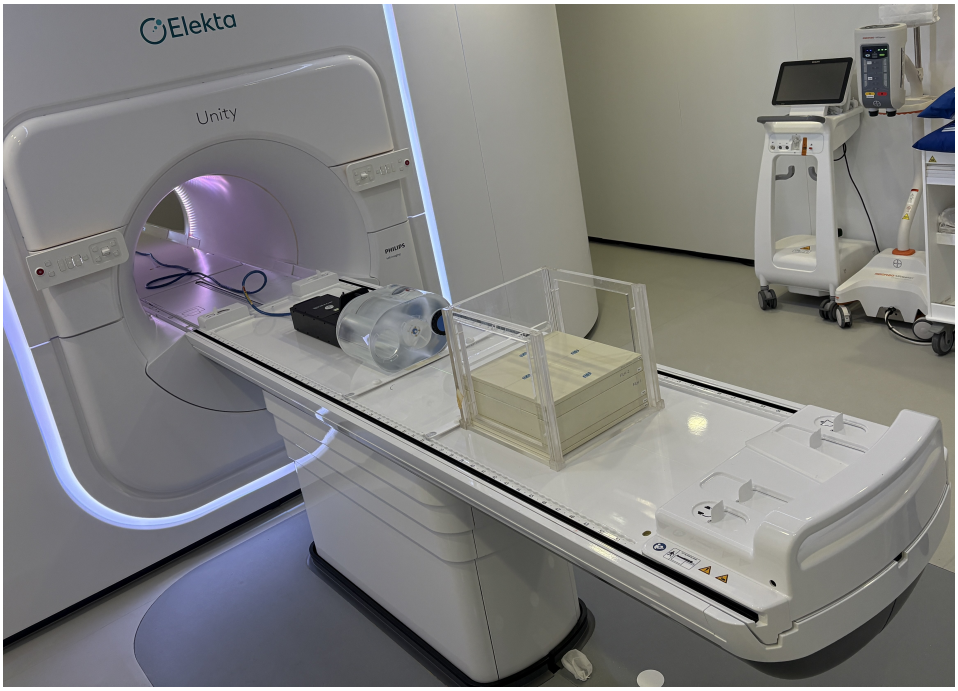

Figure 3.8: Solid water phantom setup used for calibration and scaling of Gafchromic EBT4 films, and Modus QUASAR^{TM} phantom setup for film measurements on Unity .

Film Cassette Insert available at SAMOC. This was filled together with the spherical target with aqueous contrast solution (70 ppm Mn^{2+}) following the procedure recommended by the manufacturer (Appendix E). Moreover, another set of Gafchromic EBT4 film with dimensions of 70mm $\times$ 175mm were prepared for insertion in the film cassette and secured using a set of predefined pinprick fiducials (Figure 3.9). When placed into the phantom, the film cassette exactly intersects the Ø3 cm target, allowing the film to record the dose distribution across its periphery (Modus QA, 2022). *No twist* setting was used so that the film does not rotate during plan delivery.

To prevent air pockets, which can contribute to electron contamination and effect dose measurement accuracy, a thin layer of water was sprayed onto both the upper and lower surfaces of the film. This procedure was used for all film measurements, including the calibration and scaling films following the approach in Uijtewaal et al. (2024).

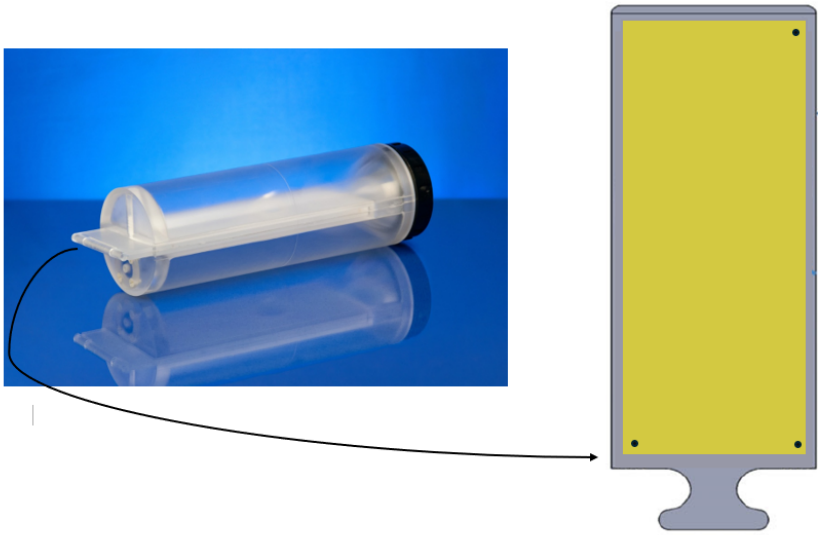

Figure 3.9: The film casette cylindrical insert is shown on the left (Modus QA, 2022). While on the right it is inside of the MRI^{4D} film cassette, showing the positions of the radiochromic films and the pinprick fiducials.

A 9-beam IMRT 7 Gy SBRT plan with a Ø3 cm target (GTV) and a 3 mm GTV to PTV margin was generated using the Monaco® TPS (Figure 3.10). The gantry angles used were 0°, 40°, 80°, 120°, 160°, 200°, 240°, 280°, and 320°. The plan comprised of 36 segments in total and delivered 1,400.99 MU. The 7 Gy prescription isodose was taken as a surrogate for the PTV edge in the film analysis.

Film irradiations were carried out following the same clinical workflow as for a patient treatment. The ATS workflow was performed once on the reference plan to create a version adapted to the first-day phantom geometry. For all subsequent measurements, every effort was made to position the phantom within $< \pm 0.25$ mm of the original ATS setup. This consistent phantom positioning allowed the ATP workflow to be applied on subsequent film irradiations without requiring any re-optimisation, thus consistently re-delivering the original ATS plan for all film exposures. This was confirmed by the isocentre shift recorded in the Monaco®. This approach was chosen to ensure the treatment plan parameters remained the same for all irradiations, thus eliminating plan re-

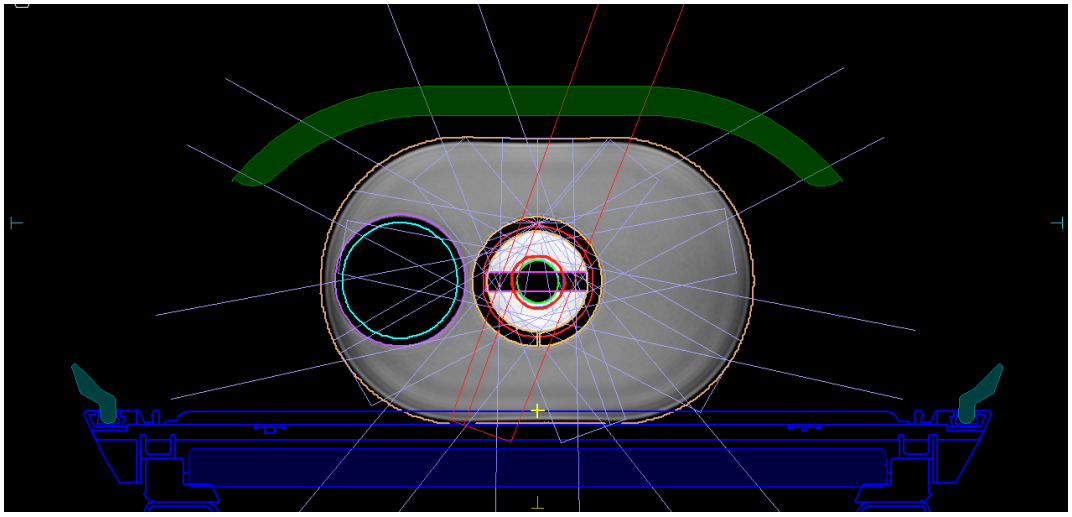

Figure 3.10: The 9-beam IMRT 7-Gy SBRT plan with a Ø3 cm target (Green contour) and a 3 mm GTV to PTV margin (red contour) using Modus QUASAR^{TM} phantom with the film insert. The green structure represents the RF coil, while the blue structure represents the patient couch on the MRL.

adaptation as a source of variation. The same plan was then delivered using different waveforms according to the different strategies shown in Table 3.3.

Waveform	**Amplitude (mm)**	**Frequency (bpm)**	**Gating Method**		**Strategy**
Sin	10	14	VOICE	100%	Respiratory
				97%	
				95%	
			Displacement Threshold	2mm	
				3mm	
				5mm	
			No Gating	N/A	
Typical 1	15	11-20	Displacement Threshold	5mm	Respiratory
Irregular 8		20-56			

Table 3.3: Waveform specifications for each strategy with the gating method used for film measurements. Bpm = breaths per minute.

3.5.6.2 | Respiratory Strategy

For each measurement day, a static reference film was acquired with the target at the 0 mm reference position and no programmed motion. For subsequent tests, a sinusoidal

trace with an amplitude of 10 mm and a frequency of 14 bpm was applied, a periodic waveform representative of a regular respiratory pattern suitable for QC purposes. This trace was first delivered without gating by disabling the ATC. For the gated deliveries, the same trace was used with different displacement thresholds and VOICE based gating enabled (Table 3.3).

Displacement threshold gating: Thresholds of 2 mm, 3 mm, and 5 mm on the target structure were applied (Table 3.3). These thresholds reflect current and evolving clinical practices in PTV margin selection: 5 mm remains common for abdominal sites such as the liver, while 3 mm and the 2 mm gating threshold were included to explore the potential feasibility of further margin reduction and the effects on plan delivery efficiency.

VOICE-based gating: VOICE thresholds of 100%, 97%, and 95% were assessed (Table 3.3). A VOICE setting of 100% implies the most stringent condition, requiring complete overlap with the PTV margin (corresponding to the 3 mm PTV margin expansion around the target). Lower VOICE thresholds progressively relax this constraint, simulating more flexible gating conditions that may be considered in clinical practice to improve treatment efficiency.

In addition to the baseline waveform, two additional motion traces, labelled as Typical 1 and Irregular 8 (Table 3.3) were selected to represent more challenging respiratory patterns. These waveforms were selected based on prior experience obtained during APM testing, so as to have < 50% of the delivery time in a *low accuracy* state, thus avoiding frequent beam interruptions and impractically long delivery times. In addition, the waveform labelled as Typical 1 was intended to capture performance under regular patient-like breathing patterns, while the waveform labelled as Irregular 8 was selected based on prior latency testing that highlighted challenging conditions. A 5 mm displacement threshold was applied to maintain the experimental conditions used during latency measurements.

3.5.6.3 | Non-respiratory Strategy

Due to the more extensive investigation of the exception gating strategy for prostate treatments in a parallel project Micallef (2025), no films measurements were taken to avoid unnecessary duplication of work.

3.5.6.4 | Digitisation and Processing

Scanning and digitising of the films was done after 24-36 hours of irradiation. All films were digitised using an Epson Expression 10000XL flatbed scanner (Seiko Epson Corp., Nagano, Japan) in transmission mode and at 127 dpi (Figure 3.11). To ensure uniform contact with the scanner bed and prevent curling, a 4 mm thick glass plate was placed on top of the irradiated films together with their corresponding scaling strips (7Gy and 10Gy) that were closest in time. Analysis was carried out using the cloud computing application `radiochromic.com`.

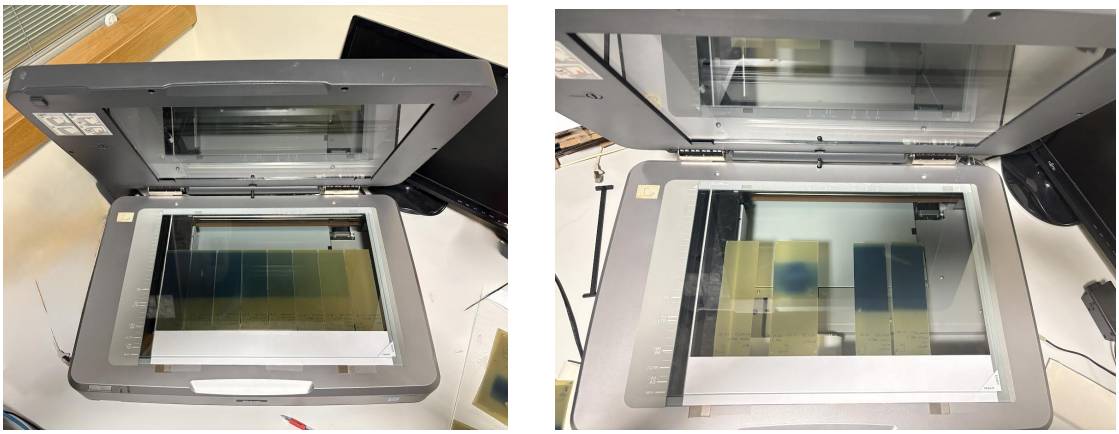

Figure 3.11: Setup of Gafchromic EBT4 films arranged on the Epson Expression 10000XL flatbed scanner (Seiko Epson Corp., Nagano, Japan) with a 4 mm thick glass plate for digitization. (a) Setup of the irradiated calibration strips (b) Setup up of irradiated films with its corresponding scaling strips (7Gy and 10Gy) that were closest in time.

For film profile measurements, a full calibration curve needed to be generated for each respective day of data collection. Each calibration curve was created by placing a $1 \times 1\text{cm}^2$ region of interest (ROI) at the maximum peak of the dose profile, since the

central axis (CAX) crosshair could not be marked directly on the film in the absence of a light field on Unity. This ROI was applied consistently across all corresponding calibration strips to ensure accurate dose response mapping (Figure 3.12).

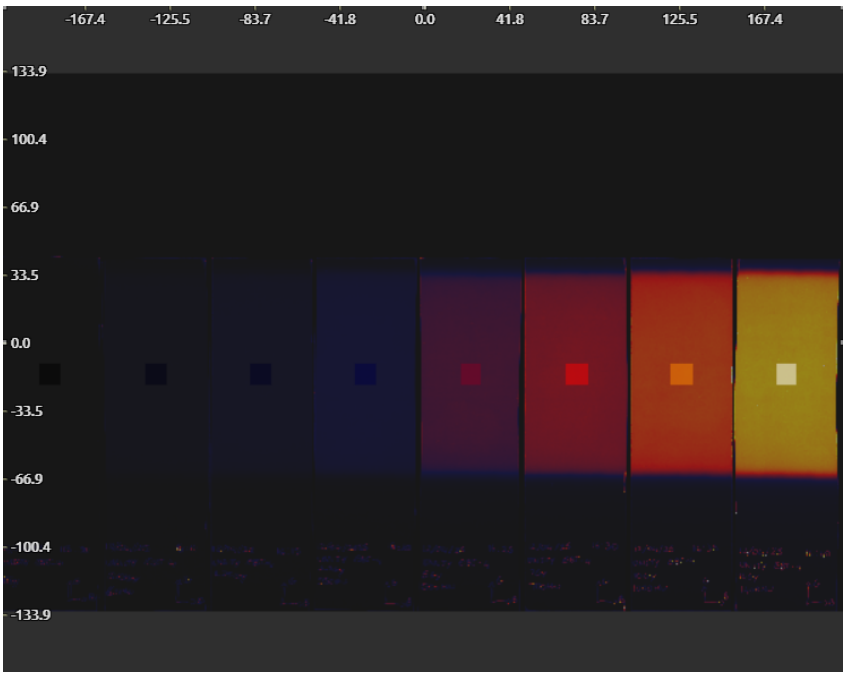

Figure 3.12: Selection of ROI's for the creation of calibration curve.

For the additional scaling strips, the $1 \times 1\text{cm}^2$ ROI was similarly placed at the maximum dose region. The reported mean dose of each ROI dose for both 7Gy and 10Gy scaling strips was recorded for three separate conditions, (a) the calibration curve applied directly without scaling, (b) the calibration curve applied with scaling on the 7Gy dose point, and (c) the calibration curve applied applied with scaling on the 10Gy dose point. The corresponding dose error to the expected dose was quantified for each case. For each film, the scaling strip closest in time to its irradiation was used to account for time-dependent changes in OD. Films acquired mid-day used the full calibration curve directly, while those from earlier or later sessions were scaled using the morning or evening 7Gy scaling strips, respectively.

For all measured film exposures, manual alignment was performed using the pin-prick fiducial marks on all films to ensure accurate alignment between each film and the reference. Every effort was made to achieve optimal alignment by using these fiducial marks and zooming in to the smallest available pixel resolution (corresponding to 0.2mm per pixel).

3.6 | Data Collection Tool

A 1.5T-MRgRT system (Elekta Unity) was used for the APM, latency, and film measurements. The MRI^{4D} Modus QUASAR^{TM} phantom together with the Modus pResp Quasar software (Version 5.0.2) was also used for data collection to analyse data.

The body of the phantom had two cavities for acrylic inserts filled with distilled water and an added aqueous solution of manganese dichloride ($MnCl_2 \times 4H_2O$ at 7 ppm). Each of the inserts features a 3 cm fillable spherical target filled with $MnCl_2$ contrast media with an acrylic stem and two baseplates. In addition, a film casette insert was used which allows placements for radiochromic film with dimensions of 70 mm $\times$ 175 mm.

The Modus pResp software allows for the analysis of the CMM audit log file extracted from the DPPC against the programmed ground truth reported by MRI^{4D} Modus QUASAR^{TM} (exported in `.csv` format). Moreover, it allows for latency measurements as the Modus pResp software compares the motion data from the encoder, simultaneously synchronized with the beam-control signal using a common time stamp with the CMM system derived on the Unity DPPC.

The CT Scanner (Aquilion^{TM} LB) was used for the assessment of the phantom's physical accuracy using the Monaco® treatment planning system (Elekta AB, Stockholm, Sweden) to derive translational offsets.

The Epson expression 10000XL flatbed scanner (Seiko Epson Corp, Nagano, Japan) was used for the digitizing of the EBT4 Gafchromic Films. For dosimetric analysis, they were uploaded into a cloud-computing application (`radiochromic.com`), which allows for the processing of images of exposed films, the calculation of isodose lines and gamma analysis (§2.7.3). Python (Version 3.10) and Excel were used to analyse profile widths and CAX dose of the film measurements.

3.7 | Data Analysis Technique

3.7.1 | Preparatory: Commissioning of the Modus QUASAR™ Phantom

Positional values were calculated in Monaco® based on the applied target shifts, and the expected positions were calculated separately from the Modus QUASAR™ programmed motion equations. The differences between these two sets of values were used to determine the maximum positional error and establish the baseline precision.

3.7.2 | Phase 1: Anatomic Position Monitoring Accuracy

The Unity acceptance testing procedure provided by Elekta makes use of the Modus QUASAR™ software to import the audit log files derived from Unity and compared against the recorded target positions from the programmed phantom motion profile (as recorded by the same software). From the software's output, the following statistics were considered for analysis: Absolute average, standard deviation (SD), and 95th percentile (P95%).

- The absolute average error was defined as:

$$\mu_{\text{abs}} = \frac{1}{N}\sum_{i=1}^{N}|x_i| \tag{3.1}$$

where, x_i are each individual error value, and N is the total number of data points.

- The SD (σ) of the positional errors to quantify the spread of error around the mean was defined as:

$$\sigma = \sqrt{\frac{\Sigma_{i=1}^{n}(x_i - \mu)^2}{N}} \tag{3.2}$$

where, μ is the mean of all error values.

- As stated by International Organization for Standardization (2006), P95 refers to the 95th percentile, i.e., the value below which 95% of all sampled positional errors fall. In this study, the P95 value represents the positional error that 95% of all sampled points remain within (Elekta, 2023b).

Additionally, Excel was used to confirm the calculations made by the Modus pResp software and to derive additional statistical calculations including the root mean square error (RMSE) as defined in Eqn.(3.3), and the average error (without taking the absolute value). This, allows for a thorough validation and verification of the software's accuracy and its computational results.

- The RMSE was selected as it provides a representative measure of the overall size of the errors, independent of their sign or directions, making it especially useful to assess components of differing signs. This is mathematically expressed as follows:

$$\text{RMSE} = \sqrt{\frac{1}{N}\sum_{i=1}^{N} x_i^2} \tag{3.3}$$

3.7.3 | Phase 2: Latency Measurements

To quantify the latency of the system the Modus pResp software was used together with a separate in-house Excel sheet that was created to replicate the analysis methodology (and accompanying Excel analysis worksheet) provided by Elekta as part of the Unity acceptance testing procedure, which evaluates and classifies the two latency types described in §2.5.3.3 i.e. Control system latency and end-to-end system latency.

For the control system, acceptable latency ranged from -300 ms to +180 ms for beam-on and -220 ms to +180 ms for beam-off. For the end-to-end system, acceptable latency ranged from -200 ms to +280 ms for beam-on transitions and -200 ms to +200 ms for beam-off transitions. Because ramp-up and ramp-down are not directly measured in this test, the Elekta methodology incorporated the maximum allowable ramp values into the Modus-reported latencies to assess compliance. The analysis also reports % beam-on and % beam-off data points, which indicate the percentage of transition data points that were within the manufacturer-specified latency limits. For each waveform used, a result $\geq$ 95% was considered to meet the performance requirements established by Elekta.

3.7.4 | Phase 3: Film Measurements

Profiles were defined along the SI direction of motion, passing through the isocentre position, corresponding to the longitudinal axis midway through the fiducial markers. These profiles were then extracted from the `radiochromic.com` software as a `.csv` file and plotted using Python (Version 3.10). All measured profiles were analysed relative to the static reference film, which served as the baseline for comparison across strategies.

The 7 Gy dose crossing points were first identified on the penumbra of each measured film profile. To improve accuracy, a linear regression fit was applied to the profile data within $\pm$3 mm around the 7 Gy level, and the position of the 7 Gy dose was interpolated from the fitted slope. From the two crossing points thus obtained, the profile

width of the 7 Gy region and its midpoint were calculated.

To calculate the uncertainty of the profile widths at the 7 Gy prescription dose, two sources of error were considered:

- In the first instance, the uncertainty of the linear regression used to determine the 7Gy inflexion point on the profile penumbra was found using:

$$\Delta x_7 = \frac{\sigma_{res}}{\mid m \mid} \tag{3.4}$$

where, Δx_7 is the uncertainty in the x-position corresponding to a dose of 7 Gy,m is the slope of regression line and σ_{res} is the SD of the residuals from the linear fit calculated using:

$$\sigma_{res} = \sqrt{\frac{1}{n-p}\Sigma_{i=1}^{n}((y_i - \hat{y}_i)^2} \tag{3.5}$$

where, y_i are the actual data points, $\hat{y}_i$ are the predicted values from the regression line, n is the number of data points (5), p is the number of fitted parameters (in this case 2).

- In the second instance, an additional source of uncertainty from the % dose error on the 7 Gy value that was used to derive the inflexion point, that in turn translates to a positional difference along the penumbral slope. This is reflected from the dose error determined from the 7Gy scaling strip for each profile, which was converted into mm distance by taking into consideration the respective slope of each profile at the 7Gy dose point:

$$\Delta y_7 = \frac{\sigma}{\mid m \mid} \tag{3.6}$$

Finally, the total uncertainty of the width, left and right 7 Gy distances on the profile after subtracting them from the reference (static) uncertainty is the quadrature sum of the regression term and the dose-scaling term:

$$\Delta z = \sqrt{(\Delta x)^2 + (\Delta y)^2} \tag{3.7}$$

where, z is the uncertainties of the difference of widths, midpoints, left and right distance, Δx is the uncertainty of the regression term, and Δy is the uncertainty of the dose-scaling term.

Moreover, an additional independent (random) term in the uncertainty of the 7 Gy profile width is attributed to the insertion of the film casette into the cylinder. Although radiochromic film was positioned precisely within the cassette using predefined fiducials, inserting the cassette into the cylinder introduces a small uncertainty in how consistently the position it was pushed at. Whilst extreme care was taken during film setup, a residual of < 0.25 mm between insertions can be estimated. This adds a minor positioning component to the measured 7 Gy profile width values.

The average dose around ± 2.5 mm of the profile centre was then calculated to represent the central-axis (CAX) dose. This metric was compared as a percentage difference against the reference (Static) film, providing a measurement of the dose difference at the profile peak.

The 7Gy isodose lines from the 2D film dose distributions were qualitatively evaluated using the film software (`radiochromic.com`) and visually compared to the reference film (static) to identify any changes or shifts in the dose distribution. Furthermore, gamma analysis pass rates were used to quantify the dosimetric impact of the system latency for each waveform trace. Gamma criteria of 3%/1 mm, 3%/2 mm, and 5%/2 mm, 5%/2 mm and 10% low-dose threshold, were used. This quantified the film agreement between the measured gated dose profile against the static reference dose profile.

3.7.4.1 | Planning delivery efficiency

To calculate planning delivery efficiency, the following equation was used:

$$\text{Plan Delivery Efficiency} = \frac{T_{\text{measured}}}{T_{\text{static}}} \times 100\% \tag{3.8}$$

where, T_{static} is the measured beam-on time (or MU delivery time) when delivered without interruptions (i.e., no gating) and, T_{measured} is the actual delivery time observed, including interruptions.

3.8 | Ethical Considerations

The University Research Ethics Committee of the University of Malta has approved this study (Appendix C).

3.9 | Limitations of the Research Methodology

One limitation is due to the phantom used is that although the phantom's positional accuracy was assessed at discrete static positions across the full ± 20 mm range, this does not guarantee that the positional accuracy is maintained during rapid positional changes in dynamic motion. The complexity of making such a measurement was beyond the scope of our project. Instead we relied on the specification quoted by the manufacturer, which stated that the phantom achieves a dynamic translational motion precision of ± 0.25mm (Modus QA, 2022).

Another limitation of our results is that the features of the phantom are idealized, and the contrast of the moving target being monitored by the CMM system is higher than likely to be encountered for patient tumours, where in the latter case the accuracy of the tracking algorithm may potentially be impacted in cases of very low contrast.

Moreover, waveforms derived from actual patient recorded data are not utilised in this project. Only manufacturer-provided motion waveforms, custom user-created waveforms, or waveforms downloaded directly from literature was used.

A further limitation of this study lies in film measurements. They are subject to several sources of uncertainty, including film to film sensitivity differences, and temporal variations in OD growth. To mitigate these effects, scaling films irradiated to 7 Gy and 10 Gy were included at the beginning and end of each measurement session. These scaling films allowed a QC assessment to monitor and assess potential inter-session and intra-session variability.

Moreover, the Gafchromic EBT4 film has a dynamic range of 0.2 to 10 Gy, therefore, the IMRT SBRT plan was constrained to this range, rather than to the full range of clinically representative doses. At SAMOC, prostate SBRT is typically prescribed at 7.25 Gy per fraction, whereas other SBRT treatments may use higher prescriptions reaching 20-30 Gy per fraction. For such prescribed doses, EBT-XD films can be used due to their wider dynamic range. However, these were not accessible at our institution. Practically, such high-dose deliveries will also extend delivery times for each film to 45 minutes or more, making a detailed study such as undertaken in this project very impractical. Nevertheless, since the linac performance evaluation performed can be considered to be independent of the absolute prescription dose, the results are expected to remain valid and directly comparable to all clinical scenarios.

Another limitation lies in the rotational alignment of the film cassette folder within the phantom. While the film cassette was securely mounted and locked into the insert channel of the Modus QUASAR^{TM} phantom, precise rotational alignment with the Drive Rod's reference line was required to avoid tilting. This alignment was carefully verified during setup; however, due to observer limitations in alignment precision, a small negligible angular error ($\sim$1.2°) may still have been introduced. Such deviation could have lead to a slight tilt of the film, potentially affecting the measured dose distribution.

Finally, time constraints limited the work that could be carried out due to the high clinical demand on the system, its use in a parallel research project (Micallef, 2025), and the need for a Medical Physicist to be present during data collection (generally scheduled

during evening and weekend sessions). For the Respiratory strategy, APM and latency phases each took approximately 8 hours per session, while film dosimetry spanned two 13-hour sessions. The Non-Respiratory strategy required 4 hours for APM and 4 hours for latency. For the Exhale strategy, despite system issues preventing full data collection, multiple attempts totalling 36 clinical hours were dedicated attempting to resolve technical issues, assisted by an Elekta clinical innovation specialist (L. Fogaça, personal communication, 13th March 2025), unresolved technical issues prevented further testing. These figures exclude further time generally required for treatment planning and contouring, preparations for the Record and Verify system and film scanning and analysis. Thus the number of waveforms tests were limited as a result and extensive testing for a wider range of different clinical scenarios could not be carried out.

Dosimetric analysis was limited to 4D water-equivalent phantoms. MR safe 4D anthropomorphic phantoms containing lung and bone tissue heterogeneities were not available at SAMOC. Consequently, this study did not assess the dosimetric impact of motion in lung tissue, where inhomogeneities and differences in motion characteristics compared to soft tissue can introduce additional complexities. Thus, our findings cannot be generalised to all the clinical scenarios especially those including lung inhomogeneities.

3.10 | Conclusion

This chapter presented the research methodology used in the study. The next chapter will include the presentation, analysis and discussion of the results.

4

Results

4.1 | Introduction

This chapter presents the data, data analysis, and results obtained from this study.

4.2 | Data

4.2.1 | Preparatory: Commissioning of the Modus QUASAR™ Phantom

The relative positional values obtained from both the Monaco and Modus control software were tabulated alongside the respective positional error for the X (LR) , Y (AP), and Z (SI) directions for both the translational and rotational settings in Table 4.1. The full data representation can be found in Appendices A and B.

Metric	**Translational Only**			**Translational and Rotational**		
	X	Y	Z	X	Y	Z
Abs Average (mm)	0.02	0.00	0.08	0.15	0.19	0.21
SD (mm)	0.01	0.00	0.08	0.18	0.16	0.21
Abs Maximum (mm)	0.03	0.00	0.09	0.16	0.32	0.32

Table 4.1: Summary of Modus positional errors in the *No Twist* and *Twist* settings. Metrics shown are the absolute average, SD, and absolute maximum for each spatial component.

4.2.2 | Phase 1: Anatomic Position Monitoring Accuracy

The results of the APM accuracy values for the respiratory, exhale, and non-respiratory strategies are presented in Tables 4.2, 4.3, and 4.4, respectively.

A histogram of the differences between the APM target displacements and the ground-truth translations provided by the Modus pResp Quasar software were also plotted in Figure 4.1, 4.2, 4.3.

Name	**QC Procedure***			**Typical 1**			**Typical 8**			**Fast Typical 1**		
	X	*Y*	*Z*	*X*	*Y*	*Z*	*X*	*Y*	*Z*	*X*	*Y*	*Z*
Average (mm)	−0.10	0.07	−0.01	−0.11	0.14	−0.04	−0.14	0.15	−0.05	−0.06	0.07	0.01
SD (mm)	0.10	0.12	0.09	0.11	0.16	0.14	0.14	0.17	0.15	0.10	0.12	0.15
RMSE (mm)	0.13	0.17	0.15	0.11	0.21	0.15	0.19	0.24	0.16	0.12	0.14	0.15
Average Abs (mm)	0.10	0.13	0.10	0.12	0.16	0.12	0.16	0.19	0.13	0.09	0.11	0.12
P 95% (mm)	0.21	0.29	0.21	0.32	0.44	0.29	0.35	0.43	0.32	0.25	0.28	0.29

Name	**Fast Typical 7**			**Irregular 8**			**cos^6 30 bpm**			**cos^6 50 bpm**		
	X	*Y*	*Z*	*X*	*Y*	*Z*	*X*	*Y*	*Z*	*X*	*Y*	*Z*
Average (mm)	0.04	0.05	−0.09	−0.03	−0.05	−0.05	−0.05	−0.03	0.01	−0.07	−0.08	−0.15
SD (mm)	0.09	0.12	0.19	0.09	0.11	0.22	0.15	0.14	0.22	0.22	0.17	0.96
RMSE (mm)	0.11	0.14	0.21	0.10	0.12	0.22	0.16	0.15	0.22	0.23	0.18	1.01
Average Abs (mm)	0.09	0.10	0.16	0.07	0.09	0.16	0.14	0.11	0.18	0.20	0.15	0.64
P 95% (mm)	0.18	0.28	0.41	0.22	0.23	0.41	0.25	0.31	0.44	0.43	0.37	1.76

Name	**Cos^6 10 bpm****			**Cos^6 14 bpm****			**Cos^6 18 bpm****			**Irregular 12 bpm****		
	X	*Y*	*Z*	*X*	*Y*	*Z*	*X*	*Y*	*Z*	*X*	*Y*	*Z*
Average (mm)	−0.11	0.07	0.02	−0.01	0.07	−0.01	−0.08	0.09	−0.02	−0.02	−0.01	0.03
SD (mm)	0.16	0.18	0.17	0.16	0.17	0.19	0.15	0.16	0.19	0.19	0.11	0.13
RMSE (mm)	0.19	0.19	0.17	0.16	0.18	0.19	0.16	0.19	0.19	0.20	0.11	0.14
Average Abs (mm)	0.17	0.16	0.15	0.14	0.15	0.16	0.15	0.16	0.17	0.17	0.09	0.11
P 95% (mm)	0.30	0.36	0.19	0.27	0.33	0.34	0.27	0.35	0.34	0.35	0.20	0.26

Table 4.2: Measurement APM Data for the **respiratory strategy** using the selected waveforms. *QC procedure refers to a sinusoidal waveform with 19 mm amplitude and 10 bpm. **These are breathing traces imported from supplementary material from literature (Smith et al., 2025).

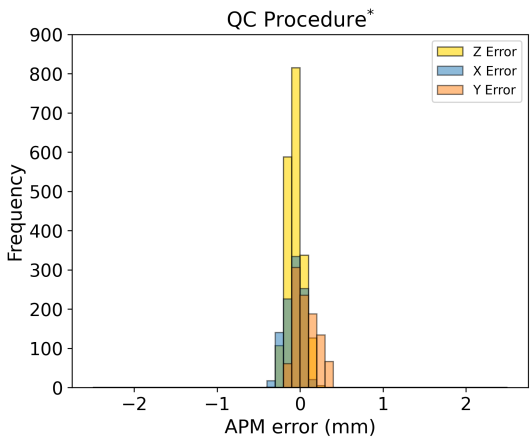

(a)

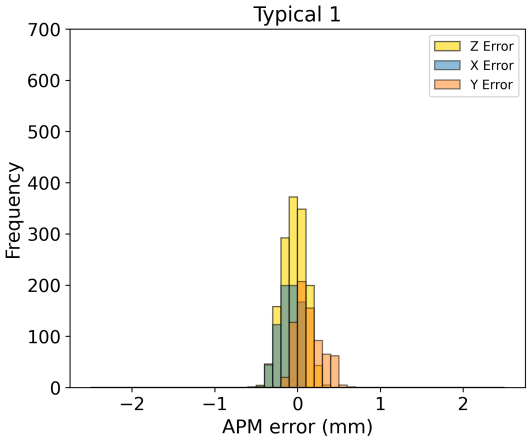

(b)

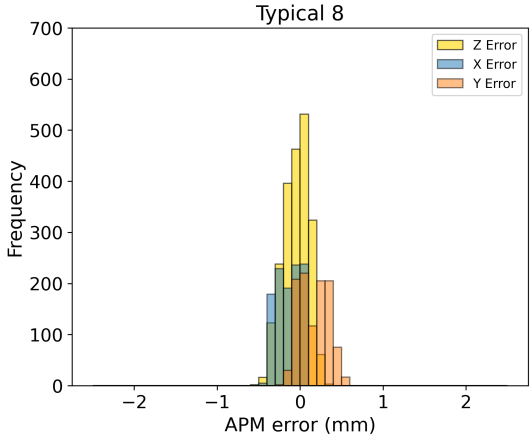

(c)

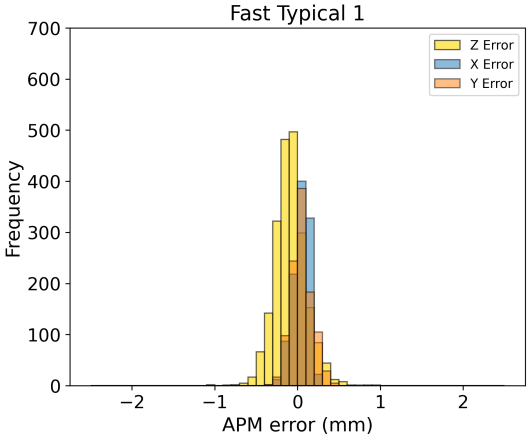

(d)

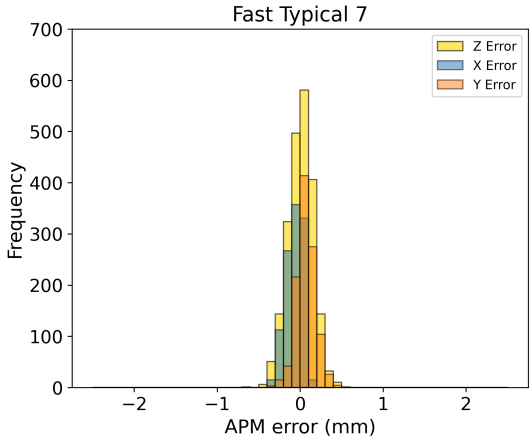

(e)

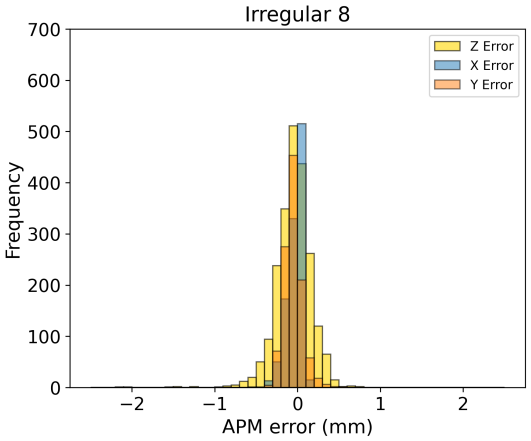

(f)

Continued on next page.

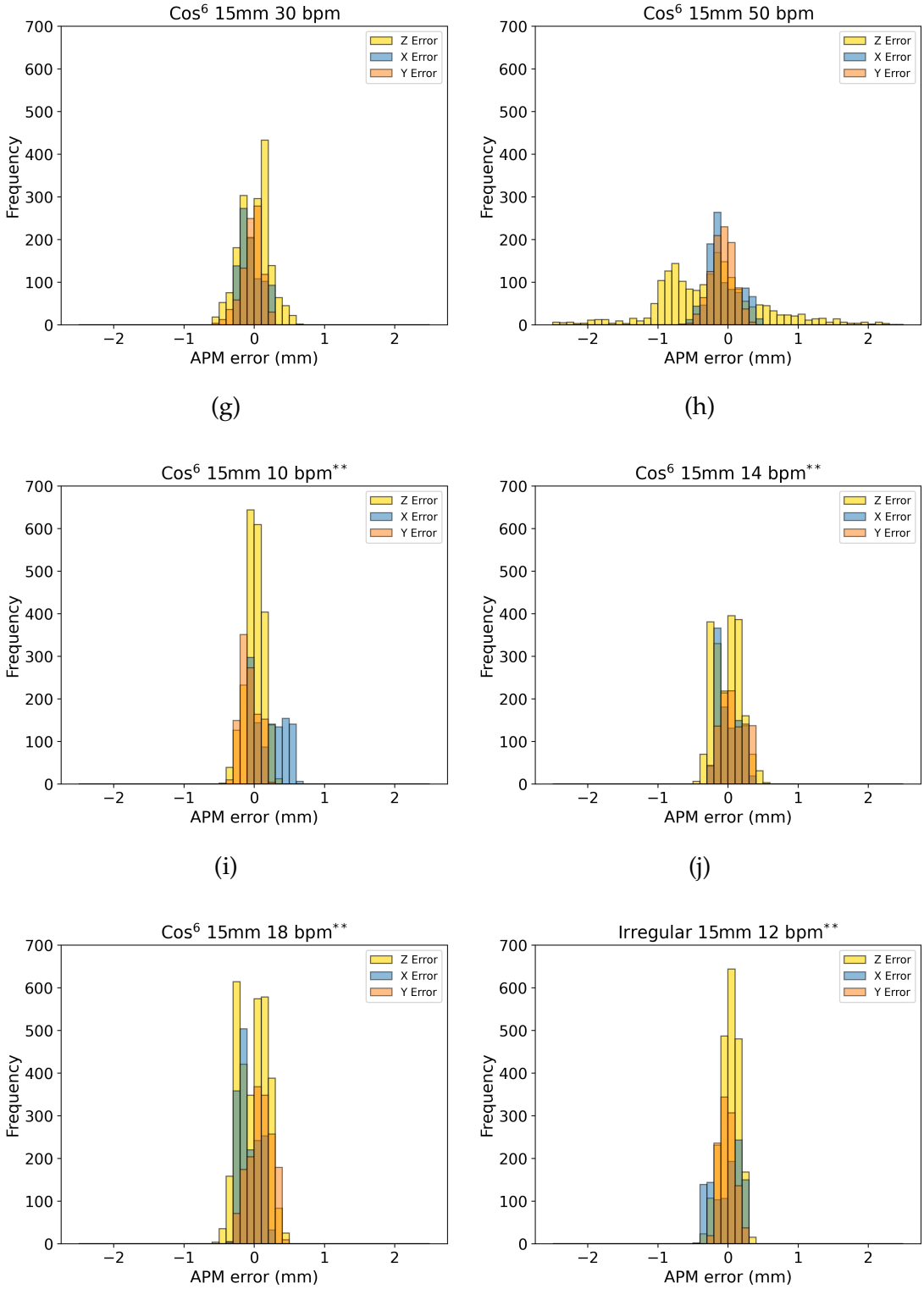

Figure 4.1: Histograms of APM error for the **respiratory strategy** using the 11 waveforms.*This refers to sinusoidal waveform with 19 mm amplitude and 10 bpm. **These are breathing traces imported using supplementary material from literature (Smith et al., 2025).

Name	QC Procedure*			Typical 1			Fast Typical 7**			Fast Typical 7		
	X	*Y*	*Z*	*X*	*Y*	*Z*	*X*	*Y*	*Z*	*X*	*Y*	*Z*
Average (mm)	−0.02	−0.01	0.02	−0.01	−0.09	−0.06	0.01	0.06	−0.11	0.21	−0.05	−0.08
SD (mm)	0.19	0.11	0.13	0.12	0.22	0.16	0.13	0.22	0.29	0.14	0.16	0.36
RMSE (mm)	0.20	0.11	0.14	0.12	0.24	0.18	0.13	0.23	0.31	0.25	0.16	0.31
Average Abs (mm)	0.19	0.08	0.12	0.09	0.20	0.14	0.11	0.18	0.26	0.22	0.14	0.33
P 95% (mm)	0.31	0.20	0.24	0.21	0.39	0.34	0.23	0.47	0.55	0.42	0.30	0.61

Name	Irregular 8			$\cos^6$ 10 bpm			$\cos^6$ 30 bpm			Sin 10 bpm		
	X	*Y*	*Z*	*X*	*Y*	*Z*	*X*	*Y*	*Z*	*X*	*Y*	*Z*
Average (mm)	−0.04	0.07	0.01	0.04	0.00	−0.12	0.04	0.00	−0.12	−0.08	0.07	−0.06
SD (mm)	0.09	0.11	0.27	0.09	0.15	0.48	0.09	0.15	0.48	0.11	0.13	0.09
RMSE (mm)	0.10	0.13	0.27	0.10	0.15	0.21	0.10	0.15	0.29	0.13	0.15	0.11
Average Abs (mm)	0.07	0.09	0.23	0.08	0.14	0.46	0.08	0.14	0.46	0.10	0.12	0.09
P 95% (mm)	0.23	0.28	0.46	0.19	0.25	0.74	0.19	0.25	0.74	0.28	0.31	0.21

Table 4.3: Measurement APM Data for the **exhale strategy** using the 7 selected waveforms. *QC procedure means Sinusoidal waveform with 19 mm amplitude and 10 bpm **This was performed using Typical 1 for the reference and daily MR acquisition, and Fast Typical 7 for the template acquisition.

Name	Sin 5bpm			Sin 10bpm		
	X	*Y*	*Z*	*X*	*Y*	*Z*
Average (mm)	-0.06	0.14	−0.04	−0.03	0.08	−0.07
SD (mm)	0.13	0.13	0.09	0.12	0.13	0.09
RMSE (mm)	0.14	0.19	0.09	0.12	0.16	0.11
Average Abs (mm)	0.11	0.15	0.08	0.09	0.12	0.09
P 95% (mm)	0.28	0.36	0.20	0.25	0.32	0.23

Table 4.4: Measurement APM data for the **non-respiratory** strategy using the selected 2 waveforms.

4.2.3 | Phase 2: Latency Measurements

The results for end-to-end latency for the respiratory and non-respiratory strategy are tabulated in Table 4.5 and Table 4.6. These tables include the maximum, minimum, average, SD, 95% percentile, and the percentages of beam-on and beam-off instances within tolerance. The corresponding histogram distributions are shown in Figure 4.4 for the respiratory strategy and Figure 4.5 for the non-respiratory strategy. For the respiratory strategy the $\cos^6$ 15 mm 30 bpm and 50 bpm could not be analysed for latency as for all instances they were always in a *low accuracy* state, preventing beam delivery.

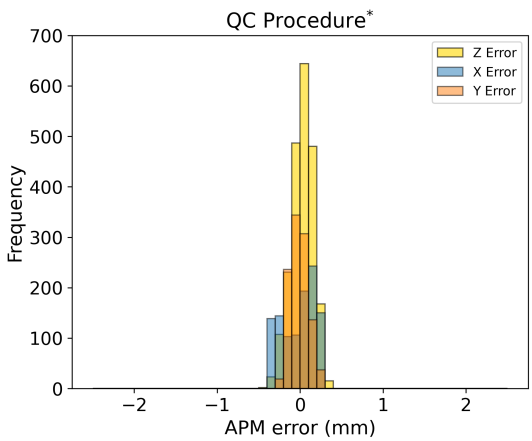

(a)

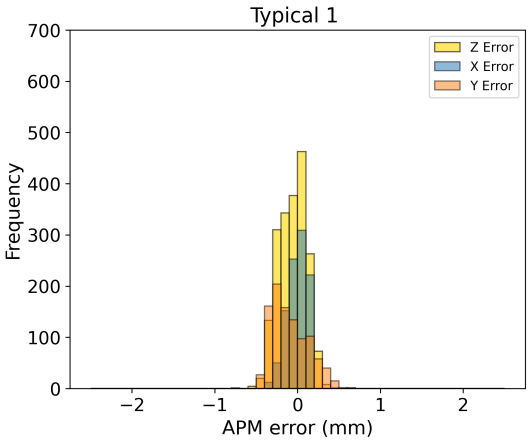

(b)

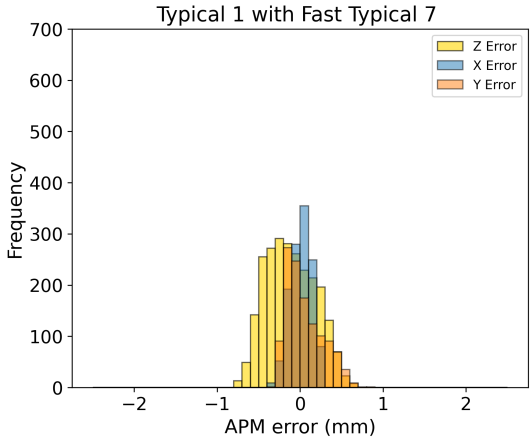

(c)

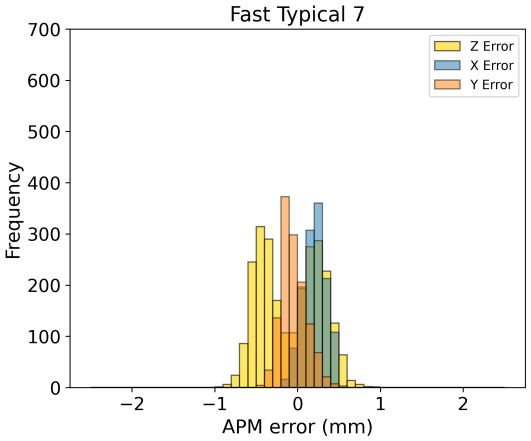

(d)

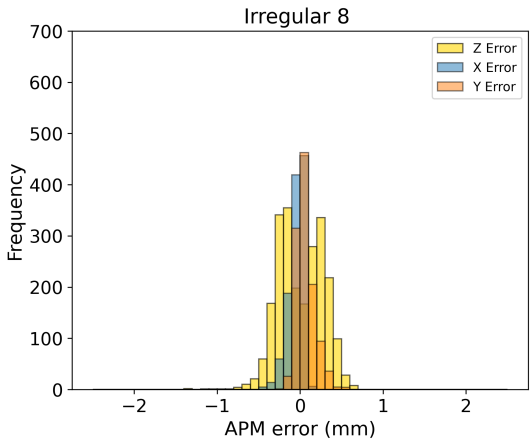

(e)

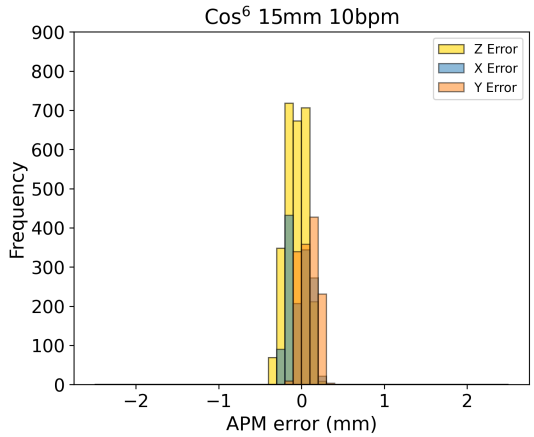

(f)

Continued on next page.

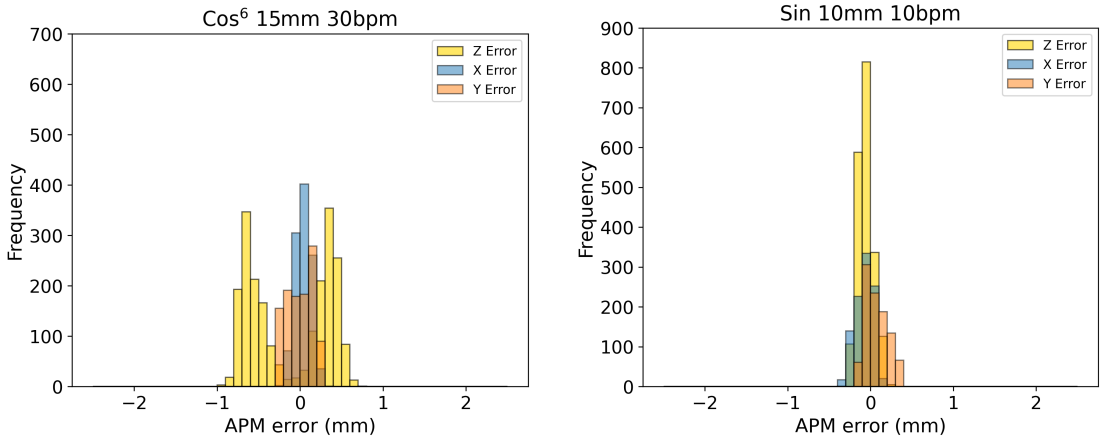

(g) (h)

Figure 4.2: Histograms of APM error for the **exhale strategy** using the 7 simulated waveforms. *QC procedure means Sinusoidal waveform with 19 mm amplitude and 10 bpm.

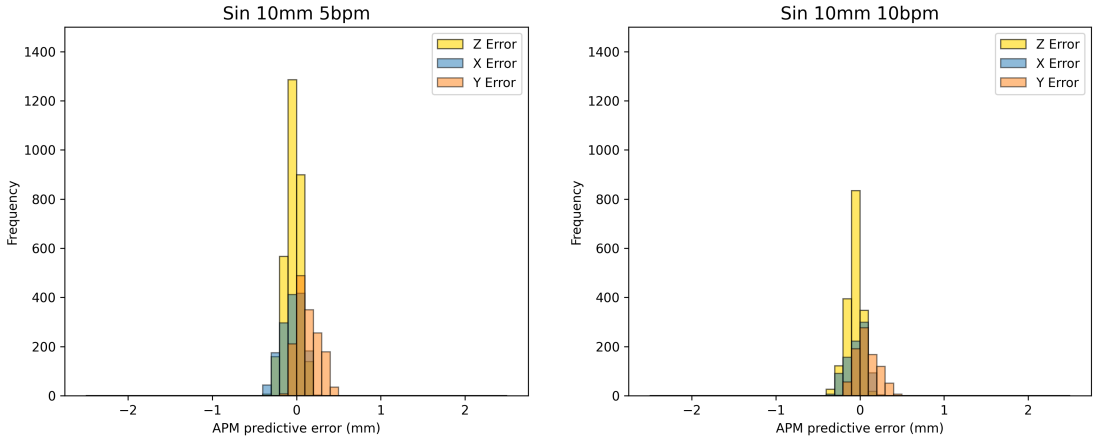

(a) (b)

Figure 4.3: Histograms of APM error for the **non-respiratory strategy** using the 2 simulated waveforms

Name	QC Procedure*		Typical 1		Typical 8		Fast Typical 1	
	On	Off	On	Off	On	Off	On	Off
Minimum (msec)	−116.5	−277.5	−254.5	−195.5	−292.5	−301.0	−548.0	−918.5
Maximum (msec)	309.0	102.0	242.0	140.5	234.5	203.0	1335.0	954.5
Average (msec)	−6.8	−17.3	69.1	−30.1	39.6	−7.7	−22.9	−30.5
SD (msec)	79.2	59.5	123.9	90.4	114.3	86.0	230.7	186.9
P 95% (msec)	120.0	106.0	254.5	195.5	222.5	179.0	428.5	313.0
% On	96.4%	–	80.0%	–	89.6%	–	77.3%	–
% Off	–	99.1%	–	100.0%	–	97.2%	–	89.1%

Name	Fast Typical 7		Irregular 8		$\cos^6$ 30bpm		$\cos^6$ 50bpm	
	On	Off	On	Off	On	Off	On	Off
Minimum (msec)	−397.0	−630.0	−349.0	−949.0	N/A	N/A	N/A	N/A
Maximum (msec)	750.5	1413.0	1862.5	978.5	N/A	N/A	N/A	N/A
Average (msec)	71.7	10.1	113.9	−7.2	N/A	N/A	N/A	N/A
SD (msec)	176.1	200.6	287.7	258.1	N/A	N/A	N/A	N/A
P 95% (msec)	397.0	359.0	490.5	675.5	N/A	N/A	N/A	N/A
% On	74.8%	–	68.0%	–	N/A	–	N/A	–
% Off	–	85.2%	–	84.0%	–	N/A	–	N/A

Name	Cos^6 15mm 10bpm**		Cos^6 15mm 14bpm**		Cos^6 15mm 18bpm**		Irregular 12bpm**	
	On	Off	On	Off	On	Off	On	Off
Minimum (msec)	−143.5	−148.0	−177.0	−238.0	−103.0	−105.0	−333.0	−220.5
Maximum (msec)	196.5	112.0	137.5	102.5	158.5	117.5	280.0	163.5
Average (msec)	−17.4	−14.4	2.6	−13.7	−9.2	24.1	−3.0	−13.6
SD (msec)	58.9	56.2	57.9	55.9	67.8	57.8	92.5	66.8
P 95% (msec)	103.5	103.5	110.0	99.0	146.0	98.0	202.0	114.0
% On	99.1%	–	99.3%	–	100.0%	–	95.4%	–
% Off	–	100.0%	–	100.0%	–	100.0%	–	99.2%

Table 4.5: Measurement Data for the latency using the **respiratory strategy** using the selected waveforms. N/A indicates cases where beam delivery was not possible due to persistent low-accuracy state. *This refers to sinusoidal waveform with 19 mm amplitude and 10 bpm. **These are breathing traces imported using supplementary material from literature (Smith et al., 2025).

Name	Sin 1 (10mm 5bpm)		Sin 2 (10mm 10bpm)	
	On	Off	On	Off
Minimum (msec)	227.0	232	222.0	228.5
Maximum (msec)	621.0	489.5	496.0	504.5
Average (msec)	365.5	371.2	349.0	362.3
SD (msec)	68.2	65.0	64.0	63.0
P 95% (msec)	468.0	467.5	453.5	460.0
% On	0%	-	0%	-
% Off	-	0%	-	0%

Table 4.6: Latency measurements for non-respiratory strategy

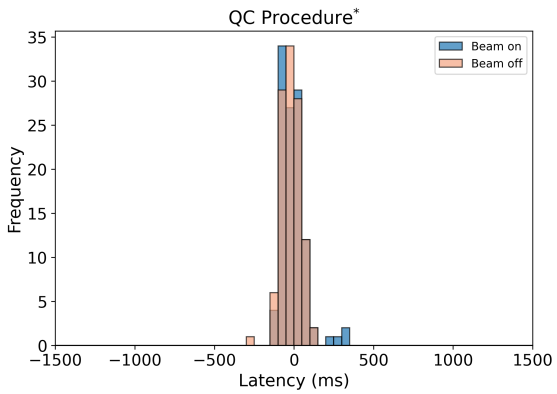

(a)

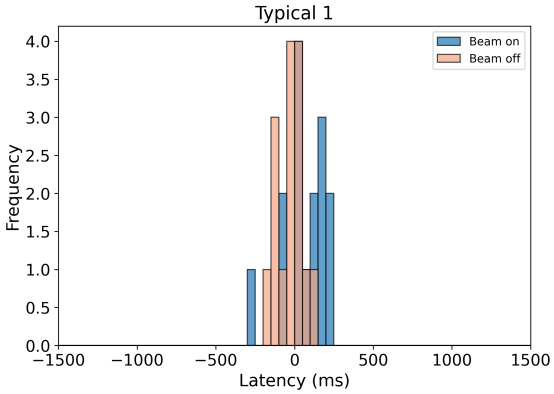

(b)

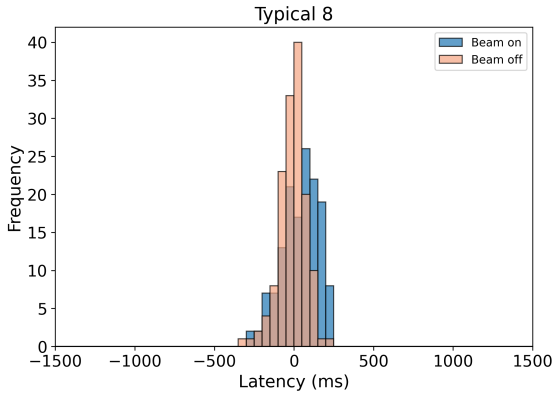

(c)

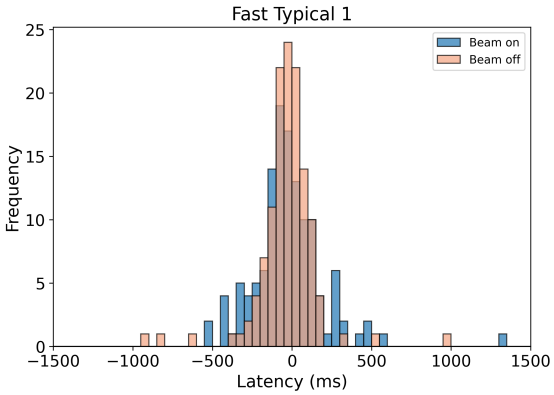

(d)

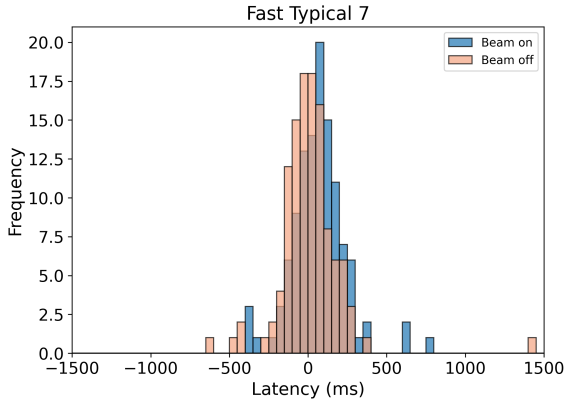

(e)

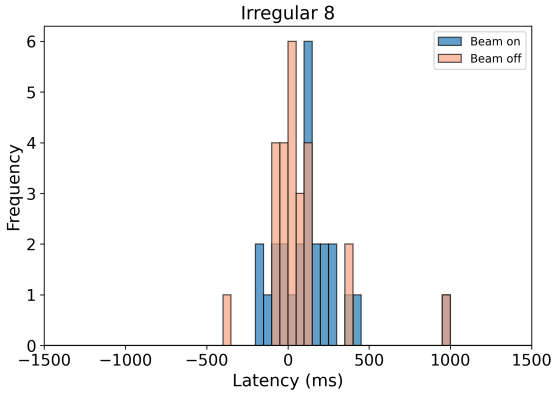

(f)

Continued on next page.

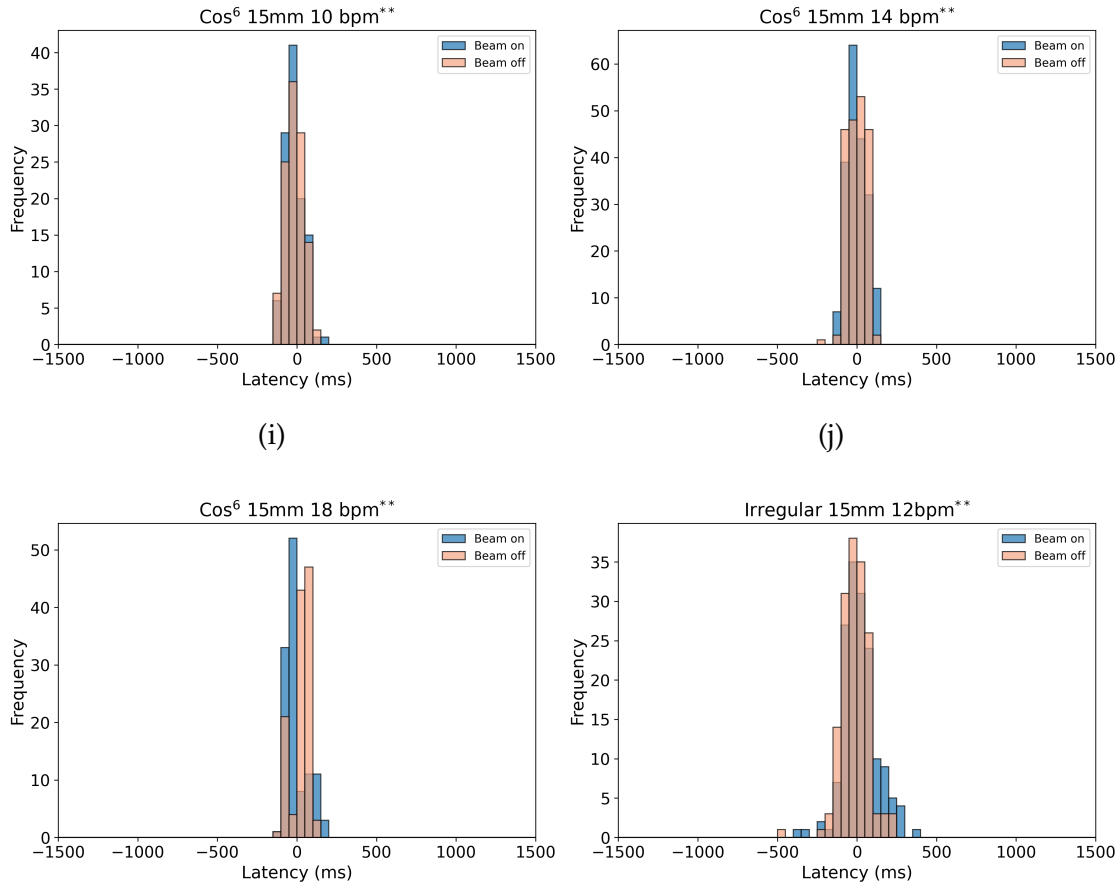

Figure 4.4: Histograms of latency measurements for the **respiratory strategy** for the 11 waveforms tested. *QC Procedure refers to a sinusoidal waveform with 19 mm amplitude and 10 bpm. **These are breathing traces imported using supplementary material from literature (Smith et al., 2025).

4.2.4 | Phase 3: Film Measurements

Quantification of scaling errors (both for the 7Gy and 10Gy) can be seen in Table 4.7.

The characteristics of three static reference profiles acquired during separate irradiation sessions are presented in Table 4.8 as an indication of the reproducibility of the film measurements.

To aid in the selection of waveform trace used for film measurements, low-accuracy instances from the CMM audit log files were quantified and presented in Table 4.9.

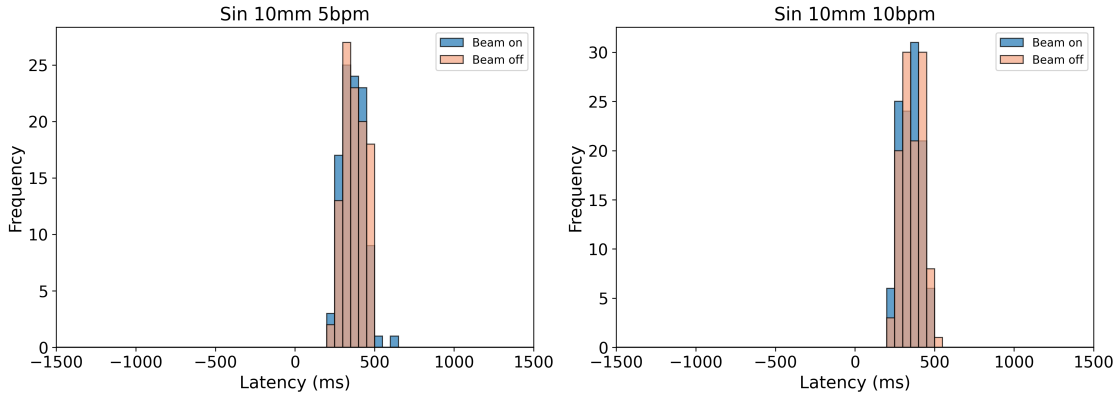

(a) (b)

Figure 4.5: Histograms of latency measurements for the **non-respiratory strategy** for the 2 selected waveforms tested

Profile	**Scaling on 7 Gy**		**Scaling on 10 Gy**	
	Error on 7 Gy (%)	Error on 10 Gy (%)	Error on 7 Gy (%)	Error on 10 Gy (%)
Static	0.2	0.7	-0.8	0.2
Not Gated	0.1	2.4	-2.3	0.0
Gating TH 2 mm	0.1	1.9	-2.4	-0.3
Gating TH 3 mm	0.1	0.4	-0.4	0.1
Gating TH 5 mm	0.0	1.7	-1.9	0.1
VOICE 100%	0.1	-1.0	0.0	-1.0
VOICE 97%	0.0	-0.7	0.9	0.0
VOICE 95%	0.0	-0.5	0.6	0.0
Typical 1	-0.1	-1.2	1.9	0.7
Irregular 8	-0.3	-1.2	2.0	0.9

Table 4.7: Scaling errors on the 7 Gy and 10 Gy for different profiles.

The film profiles generated from the film irradiations were categorized into four groups; (1) Ungated motion (gating disabled), (2) Different gating threshold (2,3,5 mm), (3) Different VOICE (95,97,100%), and (4) Complex waveforms (Typical 1 and Irregular 8). All Groups were plotted against the static reference to evaluate dose profile changes (Figure 4.6). Plan delivery efficiency was also calculated for each profile from the CMM

Profile	Width (mm)	Dose (Gy)
Static 1	36.76	8.72
Static 2	36.81	8.76
Static 3	37.29	8.73
Average	36.95	8.74
SD	0.20	0.04

Table 4.8: Comparison of statistics for three repeated static profiles: width, and dose at the centre ($\pm$2.5 mm) together with the SDs.

Waveform Name	Low Accuracy (%)
Typical 1	32.1%
Typical 8	35.2%
Fast Typical 1	91.8%
Fast Typical 7	90.1%
Irregular 8	42.3%

Table 4.9: Percentage of time each waveform considered for film analysis had an APM state that was classified as *low accuracy*.

audit log files and can be seen in Table 4.10.

The extracted dose profiles were analysed to quantify the 7 Gy prescription dose width, midpoint position, change in left and right edge from CAX at 7 Gy, and the dose at the CAX. The corresponding results, together with the uncertainties calculated using Equations 3.4-3.7, are presented in Table 4.11. Moreover, the the 7 Gy isodose line was visualised using the cloud-computing application (`radiochromic.com`), as shown in Figure 4.7. Global gamma analysis using 3%/2mm, 3%/1mm, 5%/2mm, and 5%/2mm gamma critera and 10% threshold was performed for each profile, compared with the reference (Static), as tabulated in Table 4.12.

4.3 | Data Analysis and Results

Profile	Plan Delivery Efficiency (%)
Static	100.0%
Not Gated	100.0%
Gating TH 2 mm	546.9%
Gating TH 3 mm	330.8%
Gating TH 5 mm	203.1%
VOICE 100 %	323.6%
VOICE 97%	229.6%
VOICE 95%	175.4%
Typical 1	341.5%
Irregular 8	182.8%

Table 4.10: Plan delivery efficiency across different motion profiles, expressed in %. TH = Threshold.

4.3.1 | Preparatory: Commissioning of the Modus QUASAR™ Phantom

Analysis of the average results across the three cardinal directions showed that all errors were < 0.25 mm, in agreement with manufacturer's specification (Modus QA, 2022). In the *no-twist* configuration, negligible errors were observed in the *X* (LR) direction, even though no motion was programmed along this axis. Overall, these results underline the accuracy of the manufacturer-provided Modus equations target positions, supporting their use as the ground truth reference in subsequent analysis. Moreover, the physical accuracy of the target's lateral offset from the centre was verified to be 15.0 mm, confirming the lateral offset stated by the manufacturer (Modus QA, 2022).

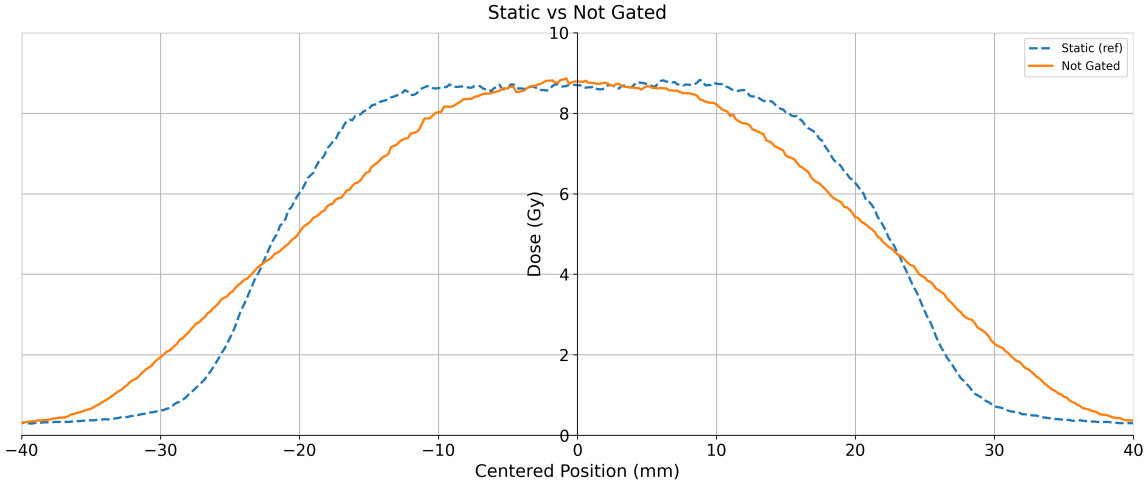

(a)

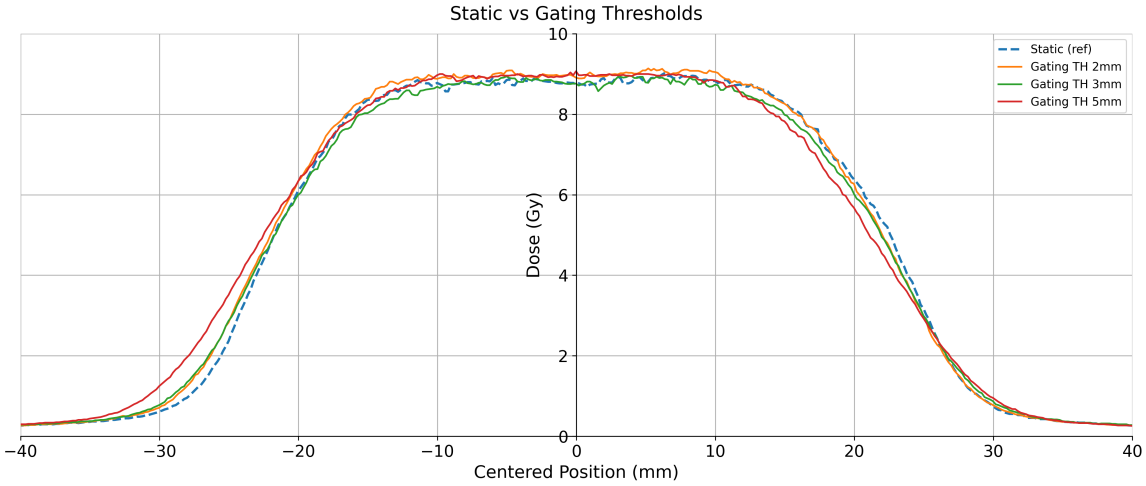

(b)

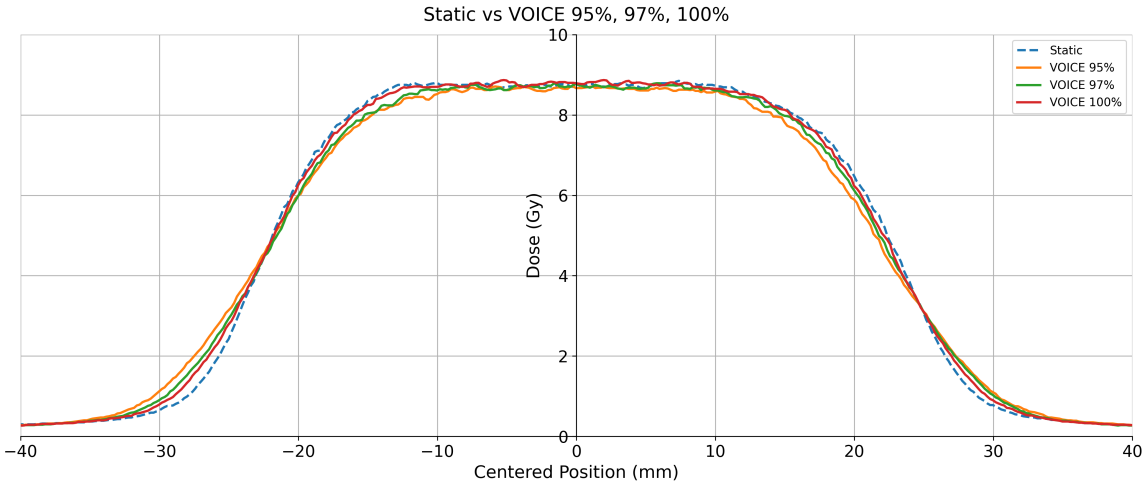

(c)

Continued on next page.

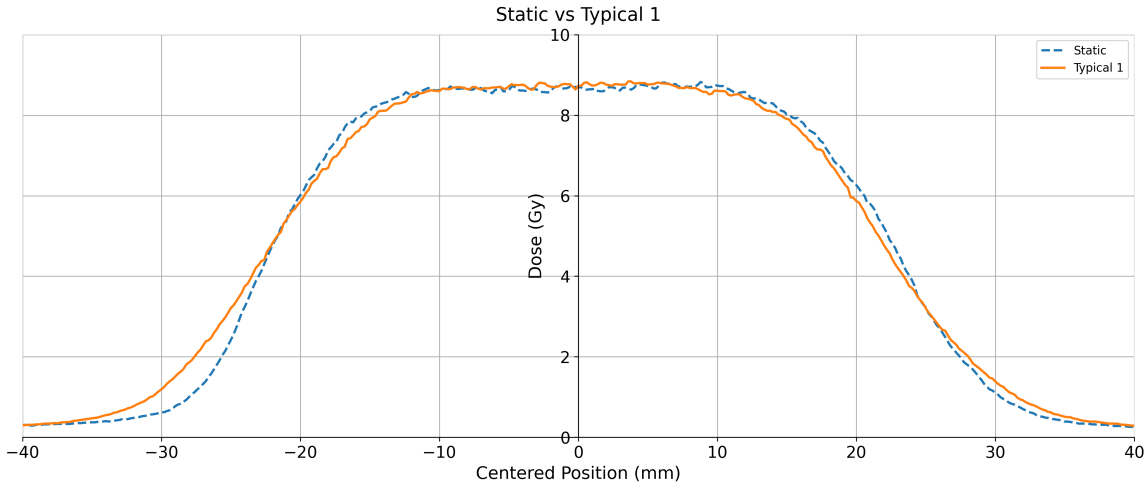

(d)

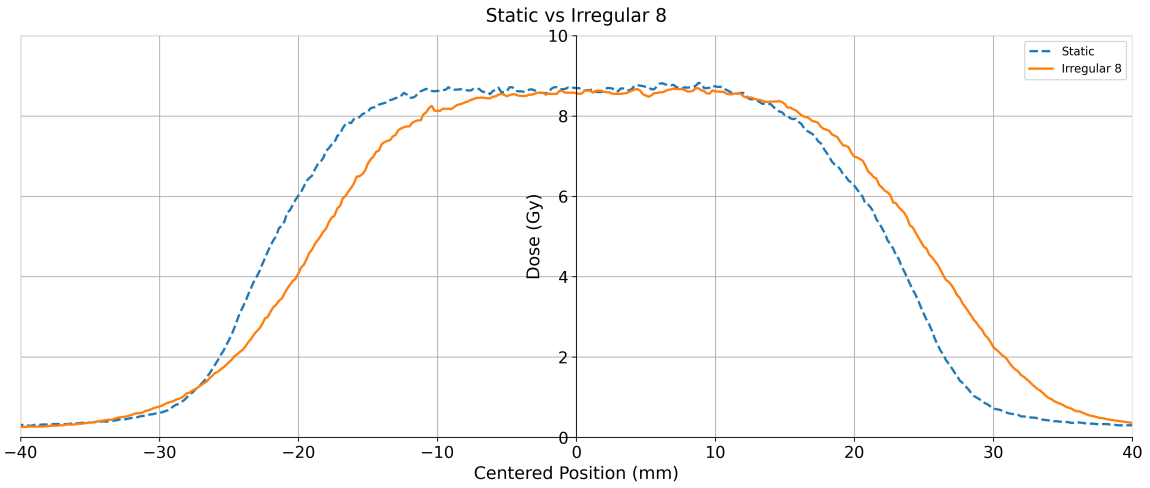

(e)

Figure 4.6: Dose profiles that were grouped according to (1) Ungated motion , (2) Different gating threshold (2,3,5 mm), (3) Different VOICE (95,97,100%), and (4) Complexity of waveform trace (Typical 1 and Irregular 8). TH = threshold. All groups were plotted against the static which was set as the reference.

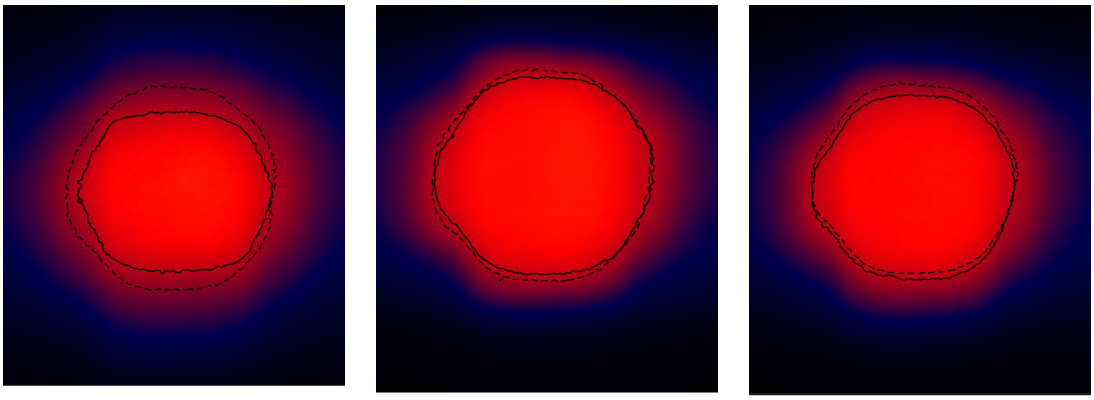

(a) Not Gated (b) Typical 1 (c) Irregular 8

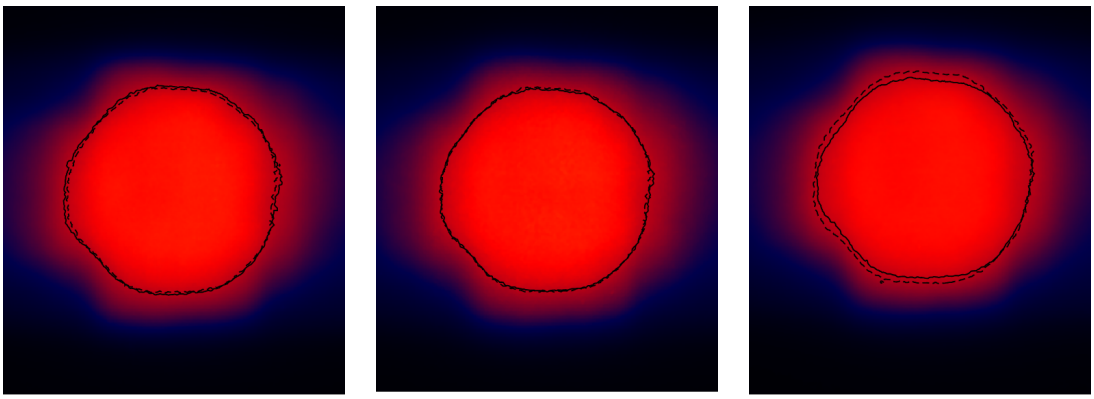

(d) Gating Threshold 2mm (e) Gating Threshold 3mm (f) Gating Threshold 5mm

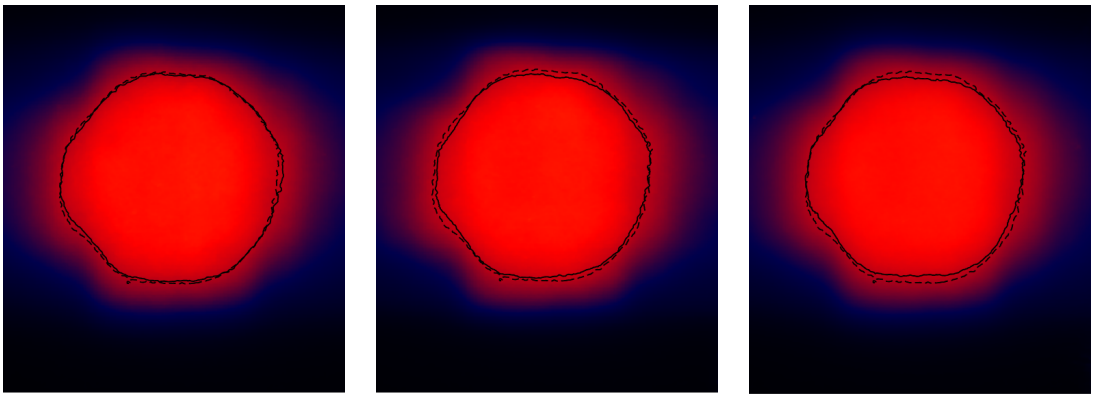

(i) VOICE 100% (j) VOICE 97% (k) VOICE 95%

Figure 4.7: 7 Gy prescription isodose lines of film measurements using respiratory strategy. The dotted line is the reference (Static) and the solid black line is the profile in question.

Profile	Width±SD (mm)	ΔWidth±SD (mm)	ΔLeft±SD (mm)	ΔRight±SD (mm)	ΔMidpoint±SD (mm)	Dose* (mean±SD) (Gy)	ΔDose
Static (reference)	36.95±0.20	–	–	–	0.00	8.73±0.04	–
Not Gated	28.57±0.18	−8.38±0.28	−4.74±0.20	−3.64±0.20	0.55±0.14	8.76±0.01	0.3%
Gating TH 2mm	37.20±0.16	0.25±0.26	0.15±0.19	0.10±0.18	0.03±0.13	8.96±0.01	2.6%
Gating TH 3mm	35.77±0.15	−1.18±0.25	−0.64±0.18	−0.55±0.18	0.05±0.13	8.77±0.01	0.5%
Gating TH 5mm	35.82±0.21	−1.13±0.29	−0.25±0.20	−0.98±0.20	−0.37±0.14	8.96±0.01	2.6%
VOICE 100%	37.03±0.06	0.08±0.21	0.05±0.15	0.03±0.15	0.01±0.11	8.81±0.01	0.9%
VOICE 97%	36.33±0.07	−0.63±0.21	−0.29±0.15	−0.34±0.16	−0.03±0.11	8.73±0.01	−0.0%
VOICE 95%	35.42±0.06	−1.53±0.21	−0.54±0.16	−0.99±0.15	−0.23±0.11	8.67±0.01	−0.7%
Typical 1	36.57±0.10	−0.40±0.22	−0.23±0.17	−0.17±0.16	0.03±0.12	8.75±0.01	0.2%
Irregular 8	35.73±0.12	−1.22±0.23	−2.16±0.17	0.92±0.17	1.54±0.15	8.60±0.01	−1.5%

Table 4.11: Comparison of Width, Midpoint, and Average Dose Values for each Profile compared to the reference. TH = threshold. *This represents the average dose at the CAX.

Profile	3%/1mm (10%)	3%/2mm (10%)	5%/1mm (10%)	5%/2mm (10%)
Not Gated	64.8%	80.3%	84.0%	90.5%
Gating TH 2mm	95.4%	98.5%	100.0%	100.0%
Gating TH 3mm	97.7%	98.7%	97.8%	98.8%
Gating TH 5mm	93.7%	98.0%	95.1%	98.6%
VOICE 100%	97.0%	98.5%	97.1%	98.6%
VOICE 97%	96.0%	98.0%	96.9%	98.1%
VOICE 95%	93.3%	96.9%	95.1%	97%
Typical 1	96.6%	98.0%	97.0%	98.2%
Irregular 8	72.5%	96.9%	85.9%	98.2%

Table 4.12: Gamma global pass rates (%) at 3%/2mm, 3%/1mm, 5%/2mm, and 5%/1mm criteria (10% threshold) for each profile compared with the static (reference). TH = Threshold

4.3.2 | Phase 1: Anatomic Position Monitoring Accuracy

Based on the results reported by the Modus pResp Quasar software, APM accuracy was within specification (95% of points less than ± 2 mm of the ground truth) for all regular and irregular waveforms representative of patient breathing patterns. All APM data points recorded were included in the analysis.

The results for the respiratory strategy represented in Table 4.2 had mean absolute errors in the X direction (LR) remaining within 0.07-0.29mm. The Y direction (AP) showed slightly lower dispersion, with absolute errors ranging from 0.09-0.19mm. The Z direction (SI) showed the highest mean absolute errors, ranging from 0.09-0.64 mm. Across all directions and waveforms, RMSE stayed < 0.30 mm, with the exception of Cos^6 15mm 50bpm which resulted in a 1.01mm RMSE. Moreover, looking at the average values they are all <0.11mm in all three direction with the exception of the Cos^6 15mm 50bpm (0.64mm in the Z direction).

For the exhale-navigated strategy from Table 4.3, mean absolute errors in the X direction remained within 0.07-0.26 mm. The Y direction showed slightly lower dispersion, with absolute errors ranging from 0.09-0.22 mm. The Z direction showed the highest mean absolute errors, ranging from 0.09-0.46 mm. RMSE remained $\leq$ 0.30 mm for all directions. For the respiratory strategy from Table 4.4, mean absolute errors in the X, Y, and Z direction were within 0.08-0.15 mm. RMSE values remained $\leq$ 0.30 mm in all directions.

Moreover, the histograms show narrow, well-centred error distributions with the exception of the Cos^6 15 mm 50 bpm waveform for the respiratory strategy and the Cos^6 15 mm 30 bpm waveform for the exhale strategy.

4.3.3 | Phase 2: Latency Measurements

Latency performance varied according to whether the gating strategy tested employed the predictive algorithm or not. For the respiratory strategies that used the prediction algorithm, latency distributions were centered around 0 ms, confirming the algorithm's ability to minimise systematic bias despite the presence of occasional large outliers. However, distributions were significantly wide for the waveforms labelled as Fast Typical 1 and 7 and Irregular 8, where beam-off delays occasionally exceeded 900 ms. For the cos^6 15 mm 30 bpm and 50 bpm waveforms, data could not be collected, as persistent *low-accuracy* states prevented beam delivery. Among the respiratory cases, the proportion of beam-on and beam-off events within tolerance ranged from 68% to >99%. Regular periodic waveforms showed they all met latency specifications with >95% beam-on and off % in specification. However, waveforms reflecting more realistic real-world conditions encountered clinically (Fast Typical 1 and 7 and Irregular 8) showed a reduction in performance relative to the $\geq$95% threshold defined in the specification[1]. A general trend across all waveforms was observed with beam-on % consistently being lower than

[1]End-to-end system, acceptable latency ranged from -200 ms to +280 ms for beam-on transitions and -200 ms to +200 ms for beam-off transitions.

that of beam-off events.

In particular respiratory waveforms (Fast Typical 1 and 7 and Irregular 8), isolated instances of beam activation occurred without a corresponding gating trigger. These events were not quantified, as the Modus pResp Quasar software does not label or timestamp them, but examples are shown in Figure 4.8. Consequently, it is unclear whether the system classified such events as delayed beam-on or beam-off transitions, or whether they were classified as *'missed'*. This introduces an unquantifiable uncertainty in the reported latency values.

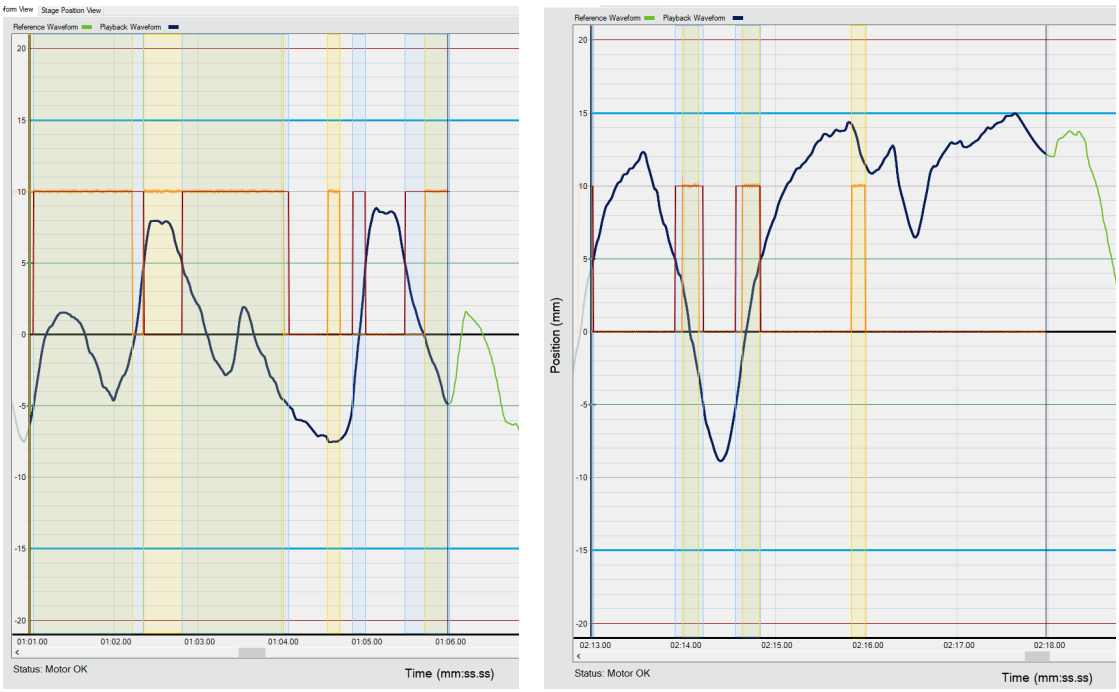

(a) Irregular 8 (b) Fast Typical 7

Figure 4.8: Example of unintended beam-on events occurring without a corresponding gating trigger during the respiratory strategy. The yellow regions correspond to beam-on events (as derived from the linac beam on signal), whereas the blue regions indicate intervals where the beam should have been delivered (as determined by Modus according to the configured gating level of $\pm$ 5 mm in this example).

By contrast, in the non-respiratory case, mean beam-on latencies exceeded 349 ms,

with no instances meeting specification[1] and 0% pass rates for both beam-on and beam-off.

4.3.4 | Phase 3: Film Measurements

When scaling on the 7 Gy strip, the film dose error was minimsed at 7 Gy but increased on the 10 Gy up to 2.7% (Table 4.7). Conversely, scaling on the 10 Gy strip minimised the error at 10 Gy but transferred the relative error to 7 Gy up to 1.9%. Since the plan prescription dose was 7 Gy and the film dose profile analysis focused specifically on this 7 Gy region, the 7 Gy scaling strip was selected for further analysis. Thus, at dose levels exceeding 7 Gy (e.g., the maximum dose at the CAX), these effects contributed to increased uncertainty in dose estimation.

From Table 4.11, the reference (Static) exhibited a prescription dose width (7 Gy) of 36.95 mm. The ungated profile exhibited the largest deterioration, with a narrowing of the field width (-8.38 mm) and a significant shift in both the left (ΔLeft = $+4.74$ mm) and right (ΔRight = -3.64 mm) intersections, as expected. Furthermore, the stricter the gating criteria (whether 2 mm threshold or 100% VOICE) the closer the 7 Gy prescription isodose line was to the reference (static). The corresponding width differences were 0.25mm and 0.08mm, respectively. Contrastingly, the 5 mm gating threshold and VOICE 95% showed the least recovery with a loss of -1.23mm and -1.53mm in total profile width. The waveform labelled as Typica1 1 was shown to have a better recovery with a loss 0.40 mm compared to the waveform labelled as Irregular 8 which showed a change of -1.22mm width.

Variability was observed when comparing dose values at the CAX with the reference (Static). The average dose at the CAX varied from -0.0% to +2.6% relative to the static film, with the highest corresponding to gating threshold 2 mm and 5 mm. These differences are consistent with the scaling trade-offs described previously. However, as no independent chamber verification was performed, the possibility of a true dosimetric

effect cannot be excluded. Consequently, these CAX dose values are reported descriptively.

The global gamma analysis (Table 4.12) showed as expected that that the lowest film agreement was the ungated profile with gamma pass rates of $\leq$90% even with less stringent criteria. Within the gating threshold group, a trend was noticed with improved performance the tighter the gating threshold. The 2 mm gating threshold consistently produced the highest gamma agreement, reaching $\geq$95% under all criteria and $\geq$98% at less stringent criteria. The 3 mm and 5 mm gating thresholds showed a slightly reduced performance even under less stringent criteria. The VOICE gating group demonstrated a similar trend. With VOICE 100%, 97%, and 95% achieving a 100%,97.8%,95.1% gamma pass rate using 5%/1mm criteria.

The complex waveforms labelled as Typical 1 and Irregular 8 profile showed a slight discrepancy between one another. With the Typical 1 achieving >95% pass rates under all criteria, while Irregular 8 only exceeded >95% using the less stringent criteria (3%/2 mm and 5%/2 mm) and fell to $\leq$86% for more stringent criteria.

4.3.4.1 | Plan Delivery Efficiency

Table 4.10 shows the delivery efficiency, expressed as the percentage ratio of the measured delivery time to the static delivery time, calculated using Eq. (3.8). For different gated thresholds, efficiency was lowest with the strictest threshold of 2 mm, where delivery took 5.5$\times$ longer than static, and improved to 2.0$\times$ longer as the threshold widened to 5 mm. A similar trend was observed with the VOICE approach, where the strictest gating envelope VOICE 100% was found to have 3.2$\times$ longer than the static, and improved when using VOICE 95% reaching only 1.8$\times$ longer. Among the waveform-specific profiles, the irregular trace showed higher efficiency (1.8$\times$ longer than static) than the typical breathing trace (3.5$\times$ longer than the static).

4.4 | Conclusion

This chapter presented the results and analysis derived from the data collection used in the study. The next chapter will include a discussion of the results in further detail.

5

Discussion

5.1 | Introduction

This chapter discusses and analyses the results obtained in further detail.

5.2 | Discussion

5.2.1 | Preparatory: Commissioning of the Modus QUASAR^{TM} Phantom

From the preparatory part of this study, the Modus QUASAR^{TM} Phantom was commissioned to confirm clinically relevant positional accuracy, as all subsequent measurements relied on it.

The analysis performed showed that the positional accuracy of the Modus Quasar demonstrated minimal deviations, with maximum absolute errors reaching only 0.03 mm for the *no twist* setting and up to 0.32 mm with the *twist* setting. Although a maximum positional error of 0.32 mm was observed during the *twist* setting, this was a one instance occurrence rather than representative of the overall performance. This outlier could likely be attributed to minor setup inaccuracies or inherent uncertainties introduced by rotational movements. Moreover, errors present in LR for the *no-twist* setting

even though no motion was programmed along this axis might also be indicative of minor setup uncertainties of the phantom on the CT scanner. Given that average errors were consistently lower, all within the manufacturer's specification ($\pm$0.25 mm), this singular outlier does not significantly impact the overall reliability of the phantom for clinical applications, increasing the confidence in the performance of the phantom.

The slightly increased error observed under all combined rotational scenarios highlights the potential sensitivity of positional accuracy to rotational dynamic movements in comparison to translation only movement. However, the statistical analysis generally emphasises the phantom's reliability, showing consistently low positional errors across all three cardinal axes and motion types, with minimal SD (< 0.25 mm). This suggests negligible variability. It is important to note that the results of this study apply for static positional accuracy. Although we relied on the manufacturer specification that dynamic positional accuracy is within $\pm$0.25 mm as discussed in §3.9.

5.2.2 | Phase 1: Anatomic Positional Monitoring

APM measurements were performed to evaluate the positional accuracy of the system against the manufacturer's acceptance criterion (P95% $\leq \pm$2 mm of the ground truth). Across all strategies, P95% values were < $\pm$1.0 mm and RMSE maintained all values of all strategies < 0.30 mm demonstrating good system performance and indicating high accuracy and reliability in the APM tracking system. All histograms showed well-centred error distributions with average signed errors < 0.15 mm in all the cardinal axes, indicating negligible bias. Only in the case of the Cos^6 50 bpm in the respiratory strategy, it was found that the P95% of the Z (SI) direction resulted in 1.76 mm and an RMSE of 1.01 mm which showed a significantly pronounced tail in its histogram. However, this waveform was included solely as an extreme test condition to test system limits. Moreover, this outlier result most likely have resulted from: reduced accuracy of the phantom during fast dynamic changes and potentially the APM's inability to manage such abrupt motion.

Previous studies (Smith et al., 2025), APM data points obtaining a low APM accuracy status were omitted, as these would not contribute to clinical beam delivery. In contrast, this work retained these instances. In Unity, this *low accuracy* status is a confidence metric based on 5 quality factors (§2.5.3.2) that inhibits beam delivery when one of its quality is disturbed and allows it once the confidence is regained. They only indicate insufficient confidence for safe irradiation, not a systematic bias in the displacement target-tracking estimate. Thus, their inclusion in this work was deemed appropriate, as they do not effect the accuracy of subsequent calculation.

Moreover, since the waveforms used in the work of Smith et al. (2025) were replicated in this study, direct comparison is possible. However, in this study the latest version of the Modus pResp software (V5.0.2) was used for positional evaluation, while Smith et al. (2025) used a previous version (V4.2.12). In the previous version, positional evaluation in all cardinal axes was based on combined data values from both imaging planes (coronal and sagittal). The updated version uses coronal plane data exclusively for the X direction, and sagittal plane data exclusively for the Y direction. This resulted the P95% values to reduced substantially by 18-55% and 64-86% in the X and Y directions respectively (Table 5.1). By contrast, the calculations for the Z direction stayed the same (taking into account both imaging planes) and therefore showed the smallest reduction in results (5-43%). This consistent reduction does not indicate improved system accuracy but rather it demonstrates that the software update improved the reported statistics of the three cardinal axes for each imaging plane used in this study.

5.2.3 | Phase 2: Latency

While APM analysis confirmed that the system can localise the target within ± 2 mm accuracy and has the ability to mitigate the total system latency, treatment precision also depends on how effectively the beam gating responds to target motion (Brown, 2024).

Waveform	Direction	P95% (mm)		
		(Smith et al., 2025)	This study	ΔP95 (%)
Cos^6 10 bpm	X	0.6	0.30	50%
	Y	1.0	0.36	64%
	Z	0.2	0.19	5%
Cos^6 14 bpm	X	0.6	0.27	55%
	Y	1.0	0.33	67%
	Z	0.6	0.34	43%
Cos^6 18 bpm	X	0.6	0.27	55%
	Y	1.5	0.35	77%
	Z	0.5	0.34	32%
Irregular 12 bpm	X	0.4	0.35	13%
	Y	1.4	0.20	86%
	Z	0.5	0.26	48%

Table 5.1: Comparison of this study's P95% (mm) values with (Smith et al., 2025).

In the respiratory strategy where the prediction algorithm is applied, low-frequency, regular periodic motion traces replicated from Smith et al. (2025) showed the most consistent latency performance, with 95th percentile beam-on latencies between 103-202 ms and beam-off latencies 103-115 ms, with most representing near-symmetric switching behaviour. This is in line with Smith et al. (2025) findings (< 188ms for beam on and <130ms for beam off). Moreover, they all met the manufacturer's latency specifications[1] with beam on % > 95% and beam off % > 99%. However, these waveforms are very periodic (i.e. cosine) and controlled which aids the predictive algorithm. Even the waveform labelled as Irregular 12 bpm in this set derived from Smith et al. (2025), despite its label, is composed of a combination of cos^6, cos^4, and cos^2 functions, making it repetitive enough for the algorithm to predict accurately. Moreover, the Cos^6 30 bpm and 50 bpm waveforms were in a constant 100% *low-accuracy* state, preventing latency measurements from being obtained.

In contrast, both waveforms labelled as Typical 1 and Typical 8, although not peri-

[1]End-to-end system, acceptable latency ranged from -200 ms to +280 ms for beam-on transitions and -200 ms to +200 ms for beam-off transitions.

odic exhibited narrow latency distributions in the histograms (Figure 4.4b and c). However, their beam-on percentages did not meet the specification (as they were < 95%), whereas beam-off percentages remained within tolerance (> 95%). This indicates that the beam experienced more delays when turning on, with P95% values of 254.5 ms and 222.5 ms for waveforms Typical 1 and Typical 8, respectively. The reduced beam-on performance can be seen as a general trend in all the waveforms and can be attributed to: (1) the prediction algorithm limitation to handle short-term erratic disruptions in the waveform and (2) due to the ramp up of the beam on which is 100ms, far longer than the 20ms ramp down (Elekta, 2023b). For example, an instance in the waveform labelled as Typical 1 (Figure 5.1), a disruption in the segment located between 20-24 seconds shows the breathing amplitude continuing to rise rather than returning downward as expected. A limitation of the Unity prediction model arises from the dynamic horizon component, which sets the prediction lead time based on the assumption that the target will either continue along its current trajectory or change direction (§2.5.3.5). In this case, the algorithm anticipated a downward return, however the trajectory kept rising leading to larger beam-on latency. This mismatch between expected and actual motion delayed the model's confidence, resulting in an increased beam-on latency.

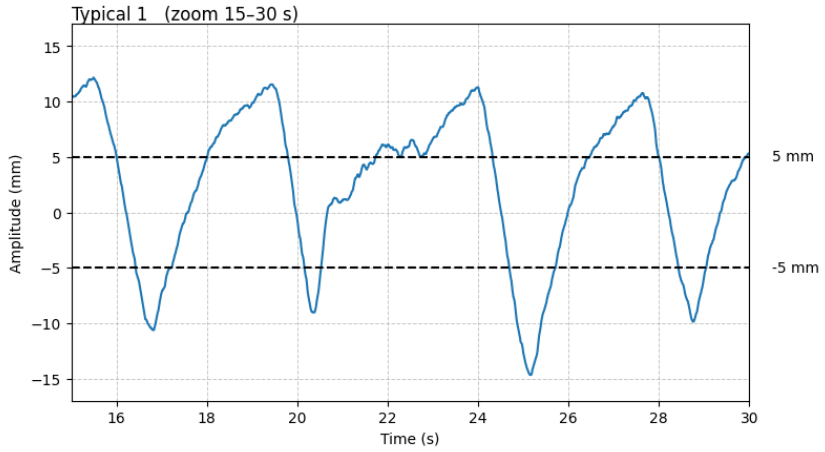

Figure 5.1: A zoomed view of the waveform labelled as Typical 1 between 15 s and 30 s showing discontinuities. Horizontal dashed reference lines at ±5 mm represent the displacement gating thresholds.

Following the same argument, waveforms labelled as Fast Typical (1 and 7) and Irregular 8 both exhibited a wide latency distribution, with maximum values > 750 ms in both the beam-off and beam-on cases. This spread in latency is caused by the irregular and rapid motion within the limited lead time of the dynamic horizon, as explained. Thus, as stated in Brown (2024), although the prediction algorithm is to mitigate average latencies the occasional high outliers (Figure 4.4d and e) suggest that prediction errors under rapid phase changes can still cause delayed beam-hold initiation.

Noticeable late and early gating latency were quite visible during certain waveforms, in particular waveforms labelled as Fast Typical 1 and 7 and Irregular 8 where there was beam delivery without having a corresponding gating event (Figure 4.8). This behaviour may indicate a timing mismatch between the motion prediction algorithm and beam-control execution, potentially resulting in irradiation outside the intended target position, which aimed to be quantified in film measurements. Once again, this further highlights the limitation of the prediction algorithm. The dynamic horizon was constrained when sudden phase shifts occur such as in the waveforms labelled as Fast Typical 7 and Irregular 8 waveforms possess (Figure 3.4). Because the algorithm must commit to a lead time based on the expected trajectory, abrupt changes in direction lead to residual latency that cannot be compensated once the prediction is executed. Clinically, such occurrences could compromise dose conformity and increased exposure to surrounding healthy tissue.

These events could not be directly quantified, as the `.csv` export file from the Modus pResp software does not label or timestamp them. However, it can be assumed that this may have led to incorrect identification of gating instances, explaining why these waveforms recorded beam-on and beam-off percentages less than the 95% threshold specification[2]. Moreover, as shown in the histograms in Figure 4.4, the average latency of the waveform labelled as Irregular 8 displayed a slight bias toward positive latencies.

[2]End-to-end system, acceptable latency ranged from -200 ms to +280 ms for beam-on transitions and -200 ms to +200 ms for beam-off transitions.

This indicates a greater number of instances where the beam was activated later than intended, in line with the much lower beam on % in specification of 68%.

In general, the tests in the respiratory strategy demonstrated that the predictive algorithm perform well under systematic testing conditions. However, under real-world clinical conditions, limitations in system performance were characterized in situations that challenge its design parameters that are more patient-like meeting one of this study's objectives.

In non-respiratory strategy, the predictive algorithm is not applied as the target is assumed to remain largely static and the beam is only interrupted if it moves outside the treatment region (Brown, 2024). The effect of this are highly visible from the histogram plots (Figure 4.5), where there is a visible systematic lag, due to the absence of the predictive algorithm and the use of a rapidly changing waveform (sinusoidal 10 mm and 5/10 bpm). So, while the latencies remained repeatable with low standard deviations (∼65-68 ms), the measured average of 362 ms did not meet the specifications[3] resulting in 0% pass for both beam on and off %. Clinically, non-respiratory motion (e.g., prostate) is dominated by slow drifts or occasional one-off shifts. Therefore, despite the longer absolute latency, the velocity is slow and the distance traversed during the latency interval is small, implying a limited dosimetric effect.

5.2.4 | Phase 3: Film

5.2.4.1 | Dose-Profiles

For the reference static condition, the three independent static measurements were compared to assess reproducibility in subsequent analysis of film profiles. Although SD were small (0.20 mm for width and 0.04 Gy for dose), the one outlier in the static repeats (Static 3) sets an upper limit on setup reproducibility. Subsequently, an averaged profile

[3]End-to-end system, acceptable latency ranged from -200 ms to +280 ms for beam-on transitions and -200 ms to +200 ms for beam-off transitions.

of the three static exposures served as the reference for subsequent comparisons with different waveforms.

For the ungated profile, the significant reduction in beam width and corresponding changes in the left and right edges is expected from motion blurring effects. This occurs as the beam remains continuously on while the target moves, the delivered dose is effectively averaged over the entire motion trace. This results in overlapping penumbra regions and an apparent narrowing of the measured profile, where a large -8.38 ± 0.28 mm decrease in width was observed. Clinically, this narrowing and inward shift of the 7 Gy prescription isodose translates to reduced CTV coverage, as this motion blurring causes parts of the target volume, particularly at the periphery to receive less than the prescribed dose, increasing risk of underdosage. This collapse of the dose distribution is clearly observed, with the 7 Gy prescription isodose line showing a marked inward shift relative to the static reference (Figure 4.7a). The same effect is consistently reflected in the corresponding dose profile and gamma result (between 64.8-90.5% for each criteria). However, this is directly applicable for soft tissue only as the Modus QUASAR^{TM} phantom is water-equivalent and does not replicate lung tissue heterogeneity. Consequently, the findings presented here are directly applicable to soft-tissue tumour sites but cannot be generalised to lung tumours. For lung targets, this effect is typically more pronounced, one expects blurring with a broader penumbra, dose reduction along CAX, further collapse of the prescription isodose, and further underdosage at tumour periphery as demonstrated by Tsiakalos et al. (2004) and noted by White et al. (1996). This is due to the low density in lung which increases secondary electron ranges, causing partial loss of lateral electronic equilibrium at tumour lung interface.

In contrast to the ungated profile, the gating threshold profiles show recovery of the 7Gy prescription isodose. With a tight 2 mm gating threshold, this broad penumbra realigns back with the static almost completely with a minimal change in width of 0.25mm. Clinically, this minimal deviations indicate that tight gating can restore CTV coverage to a level comparable with static (ideal) delivery. The 3 mm gating threshold

showed a greater deviation, with a -1.18 ± 0.20 mm change in width and broadening of the penumbra on both edges (-0.64 ± 0.18 mm vs -0.55 ± 0.18 mm). Clinically, this means one is compromising the CTV coverage. By contrast, the 5 mm gating threshold exhibited a slightly smaller reduction (-1.13 ± 0.29 mm) than that for the 3 mm threshold but the shifts in the left and right edges (-0.25 ± 0.20 mm vs -0.98 ± 0.20 mm) were larger. This asymmetry was clearly visible in the dose profiles (Figure 4.6). Considering these asymmetries, results show that it was only for this profile and the corresponding lenient gating of VOICE 95% (-0.54 ± 0.16mm vs -0.99 ± 0.15 mm) from these 2 sets. However, these asymmetries might have been attributed to setup/measurement uncertainties. Thus, further work should replicate this work to determine if this implies peripheral underdosage on one side of the CTV.

Similarly, the trends observed with the gating thresholds were also evident in the VOICE gating results. The 100% VOICE setting (equivalent to a 3 mm gating threshold) showed minimal deviations from the static reference with 0.08 ± 0.21mm change in width. This is also highlighted in the dose profiles and isodose lines where the penumbra is seen to closely match the static reference compared to the ungated profile much better than the 3mm gating threshold. This deviation from the gating threshold 3mm likely reflects motion-related positional uncertainties, where even small deviations at the field edges are amplified by the penumbra gradient and manifest as changes in profile width. As the VOICE percentage was reduced (VOICE 97%), a clear trend of increasing width deviation appeared with a -0.63 ± 0.21mm change, consistent with the greater gating tolerance and broader penumbra. The poorest performance was observed using the lowest VOICE setting of 95%, with a -1.53 ± 0.21mm width change. A similar concept to the 5 mm gating threshold, this clinically means that the 7 Gy prescription isodose line would no longer fully cover the CTV, leading to underdosage at the tumour periphery.

Moreover, as previously reported for conventional linacs, tighter gating windows are associated with lower plan efficiency (Pepin et al., 2011; Short, 2018). A similar trend

was observed in this study on Elekta Unity, where delivery time reduced from 5.5× to 2.0× longer when the gating threshold was changed from 2 mm to 5 mm and from 3.3× to 1.8× longer when VOICE was changed from 95% to 100%. Thus, the argument of Pepin et al. (2011) and Short (2018) holds true in the MRL setting where, although a stricter gating threshold or VOICE ensures superior target coverage, it does so at the expense of treatment efficiency, which may be clinically impractical for routine use unless adequately addressed with increased PTV margins.

Complex waveforms such as the waveform labelled as Irregular 8 showed a significant dosimetric impact (Figure 4.6). The corresponding profile shows a width reduction of -1.22 mm, characterised by a change of -2.16 mm on the left, 0.92 mm on the right, and a positive midpoint shift of 1.54 mm. In fact, this change in the midpoint positions is the highest out of all profiles. This is reflected in the isodose lines in Figure 4.7b where the profile can clearly be seen to be shifted compared to the reference (Static). Such shifts are consistent with the observed beam on firing (Figure 4.8), where the beam was triggered outside the intended gating window due to prediction-execution mismatch. As well as the shifted latency histograms for beam-on instances and lower beam-on %. In practice, this behaviour could compromise target coverage, as systematic offsets may accumulate to clinically relevant underdosage to the CTV.

To mitigate this, an additional margin may be warranted for patients with similar erratic breathing patterns. For example, expanding the PTV by an additional 1 mm or incorporating an internal margin into the CTV could help compensate for these uncertainties, ensuring that the target remains adequately covered despite prediction errors. However, while such margins improve coverage robustness, they would also increase the irradiated volume of surrounding tissue, underlining the need for further investigation into margin optimisation specifically for irregular breathing patterns. However, these findings were acquired with a 5 mm gating threshold. Future work should determine whether the width reduction is threshold or waveform-driven. If threshold-driven, CTV to PTV margins may not need enlargement.

Comparing this with the waveform labelled as Typical 1 waveform which was also compared with the static reference it has $<$ 0.4 mm in width profile and $<$ 0.25 mm in changes in left, right and midpoint. Thus, the findings of the latency which showed that it did not pass the 95% criteria, did not result in a dose accumulation outside the target at the 7 Gy prescription dose. Meaning, that the CTV is still covered and not being underdosed. Moreover, Typical 1 exhibited almost twice the delivery time (Table 4.10) compared to the waveform labelled as Irregular 8 which may be due to the missing isolated beam on events in Typical 1.

These measured offsets seen on films may in part be attributable to a limitation of this study which is the presence of inherent film-related and setup-related uncertainties in addition to uncertainties reported in Table 4.11. Although every effort was made to minimise these, such as ensuring that the fusion of the daily MR with the planning MR (using ATP) produced a transformation matrix error of $\leq$ 0.25 mm in all directions and the $<$ 0.25 mm limitation of the film cassette positioning. This process was done to provide a quantitative estimate of positioning uncertainty, allowing its contribution to the film measurement results to be characterised and separated from motion or gating related effects. Furthermore, when aligning the film profiles with their respective references, fiducial marks were used and zooming to the finest available pixel resolution was applied. At worst, this manual alignment introduces an additional uncertainty of $\sim$1-2 pixels (0.2-0.4 mm). However, it may very well be true delivery effect. Having said that, it is still difficult to generalize these findings to the entire population. But this width reduction in the waveform labelled as Irregular 8 is still an actionable result.

5.2.4.2 | Gamma Pass Rates

As a general remark, changes in the CAX doses, quite visible in Figure 4.6 may be attributed to the 7 Gy scaling method used. Moreover, every effort was made including generating a new calibration curve for each measurement day using the 7 Gy scaling

method, discrepancies were visible when comparing dose values at the CAX with the reference (Static). These deviations arised from several factors including: (1) Inherent variability in film response (2) the effect of exposure-to-scan time and (3) amplification of small errors during the scaling process. Moreover, without an independent ion chamber measurement we cannot separate delivery effects from film/scaling effects. Thus, these CAX dose values can only be reported descriptively.

However, due to this potential percentage error arising from the scaling method, the gamma analysis was evaluated using a range of criteria (3%/1 mm, 3%/2 mm, 5%/1 mm, and 5%/2 mm). The 3% dose-difference sets reflect standard practice in film-based dosimetry as reported by various literature (Smith et al., 2025; Uijtewaal et al., 2024), but also because CAX dose deviations of $\sim$3% were observed, higher 5% criteria were included to prevent lower gamma pass rates dominated by CAX error bias. Having said so, the absolute dose percentage component of gamma was less impactful, reflecting both the intrinsic scaling uncertainties of film dosimetry. However, as no ion chamber measurements were performed in parallel, absolute dose could not be independently verified, and the interpretation of this absolute component is therefore limited. The 1mm and 2mm distance-to-agreement thresholds were chosen to emphasise sensitivity to spatial accuracy, which was the goal of interest in this study.

For the 3%/2 mm criterion which is one of the most standard criterion in gamma analysis, all profiles achieved pass rates above 95%, with most exceeding 98%, except for the expected failure of the ungated case, as follows from dose-profile discussion. Moreover, further support of the previous argument that a stricter gating threshold results in almost full recovery can be seen in these measurements with the gating threshold of 2 mm and VOICE 100% having gamma pass rates of >95% even under the most stringent criteria. Having gating thresholds be more lenient (VOICE 97% and threshold 3mm) still achieved >95% but mostly showed further reduction compared to the 2mm gating threshold and VOICE 100%. This is consistent with the findings that small residual motion broadens the penumbra and introduce a further width reduction.

Furthermore, in most criteria, the lowest gamma rates were observed for the 5mm gating threshold and VOICE 95%. Although under lenient criteria(3%/5%/2mm) they achieved >95%, under stricter criteria (3%/1mm) they fell below this percentage, again driven by the reduction observed in widths with edge deviations of -0.98mm and -0.99 mm, respectively. Adjusting the spatial tolerance (1-2mm) restores the gamma pass rates >95%. This highlights that the failure was attributable to millimetric positioning offsets rather than systematic dose error.

For complex waveforms (Typical 1 and Irregular 8) they achieved >95% under more lenient criteria (5%/2mm and 3%/2mm). However, under more stringent criteria, irregular 8 showed a reduction of 72.5% and 85.9% for 3%/1mm and 5%/1mm, respectively. These failures correspond to profile edge deviations of +2.16 mm in Irregular 8 an adjustment in spatial tolerance once again increases the gamma rates. This demonstrates further that such millimetric deviations should be anticipated and incorporated into PTV margin design to ensure adequate CTV coverage at the tumour periphery.

5.3 | Conclusion

This chapter has provided a comprehensive analysis and interpretation of the findings of this study. The following chapter will focus on presenting the conclusions drawn from this research and providing recommendations for professional practice and future research.

6

Conclusions and Recommendations

6.1 | Introduction

This chapter covers the main findings from the research and provides practical recommendations for professional practice and future research.

6.2 | Summary of conclusions from the study

- The commissioning of the Modus QUASAR^{TM} Motion Phantom confirmed its suitability for simulating tumour motion in MRgRT, with positional accuracy on average remaining within the ± 0.25 mm specification given by the manufacturer (Modus QA, 2022).
- Across all motion scenarios and strategies (respiratory, exhale-navigated, and non-respiratory), APM met the ± 2 mm accuracy specification and also demonstrated that it is generally better than ± 1 mm in all axes.
- Latency analysis confirms that the predictive algorithm in respiratory strategies effectively reduced average gating delays and maintained latencies within clinical specifications for regular periodic waveforms. However, highly irregular or fast waveforms produced larger latency outliers, which are not fully compensated for by the prediction algorithm.

- Film dosimetry showed that regular patterns maintained adequate target coverage with minimal reduction in profile width (dependent on gating critera) despite having a slightly worse lower beam-on latency results. Irregular respiratory patterns can cause clinically relevant underdosage to the target and may result in systematic profile shifts as observed for the waveforms studies.

- Tighter gating (2 mm or VOICE 100%) improved dosimetric target coverage (0.2 to 0.7% of the reference) but increased delivery efficiency by $\sim$3.3 to 5.5$\times$ more. Conversely, wider gating (5 mm or VOICE 95%) is 1.8 to 2.0$\times$ more efficient but reduced dosimetric target coverage by $-$3.3 to $-$4.1% of the reference.

6.3 | Recommendations for Professional Practice

The following are recommendations for professional medical physics/radiation protection practice:

- In general, for respiratory gated strategy an additional 1mm may be considered in the PTV margin, or equivalently adding a small margin to the CTV margin to allow for a potential reduction in prescription isodose widths, to safeguard against systematic undercoverage arising from gating latency as observed in this study.

- Clinicians can consider balancing target dose conformity with delivery practicality. In current practice, 5mm or 3mm are commonly applied for abdominal sites such as the liver. One can improve efficiency by going to wider gating criteria, but one needs to increase the PTV margin to compensate for the slight lack of CTV coverage. The trade-off will be the higher treatment volume as a result. Conversely, if tight margins (2mm or 3mm) are clinically relevant, and increasing PTV margins is clinically undesirable, this will come at the cost of the reduction in treatment efficiency.

6.4 | Recommendations for Future Research

Suggestions for further research are:

- A future study could replicate this work following the planned upgrade of the Philips Marlin system to the new cine imaging, to enable direct pre-and post-upgrade comparison. Repeating key experiments under identical settings will quantify any changes in APM, latency, and gating efficiency providing an evidence base for any clinical parameter updates.
- Replication of this work under the same conditions to re-assess waveforms that showed asymmetry width reduction in the profiles that could translate to under-dosage on one side of the CTV.
- A separate future study can assess the accuracy of the CMM system using low contrast targets. This can be done on the Modus QUASAR^{TM} phantom by diluting the solution in the spherical target from 100% to 15% with 0% being the same as the background water in the phantom body. However, viability is still limited considered the high-contrast dark annulus around the target on cine imaging due to the perspex wall giving no signal. Possibility of designing a phantom to mimic such low contrast tumour relative to background could also be considered.
- The findings of the dosimetry study are not directly transferable to lung inhomogeneities. Additional validation for the film measurements is required using MR safe 4D lung-equivalent phantoms or patient-derived imaging and motion data to ensure the reliability of gating performance and dosimetric accuracy in thoracic treatments.
- Although the exhale navigated strategy could not be fully explored in this study, the assessment of latency and dosimetric affect under exhale navigation is still desirable. As this approach could reduce the ITV and improve target conformity by restricting beam delivery to the exhale phase, thereby minimising irradiation of healthy tissue compared with the respiratory strategy. However, in our implemen-

tation, it was inconsistent across testing days, manifesting as a double-image of the target. This inconsistency is presently being attributed to difficulties in translating scanning parameters tuned for patient anatomy into the phantom context. However, a future study could address and confirm this inconsistency. Further research should therefore, include volumetric assessment of the target during the exhale phase to determine if its apparent size changes and compare to literature, such as Snyder et al. (2019).

6.5 | Conclusion

This study successfully met all its objectives except the full assessment of the exhale-navigated strategy, which was limited by unresolved technical issues. It is believed that this study is the first to evaluate three strategies on the Elekta Unity MRL using irregular, non-periodic waveforms that more closely reflect patient motion. The APM system consistently achieved millimetre-level accuracy across all strategies tested, confirming its reliability across all tested scenarios. Latency evaluation highlighted the benefits of predictive algorithm for the respiratory strategy. Subsequently, regular respiratory waveforms met latency specifications, whereas irregular traces produced degraded latency performance and occasional gating mismatches. Non-respiratory strategies did not meet the latency specifications, which is expected since they are not designed with predictive algorithm and are intended for static targets. Film measurements demonstrated that typical breathing traces maintained target coverage despite minor latency deviations, whereas irregular breathing may compromise dose conformity and reduced CTV coverage and may require small additional PTV margins to ensure adequate dosing. While tighter gating thresholds (2 mm and VOICE 100%) setting provided better target coverage, wider thresholds improved delivery efficiency at the expense of conformity.

Overall, the findings confirm the robustness of the Elekta Unity CMM system. In view of the knowledge gained in this project, consideration can be given to to assess

PTV margins to ensure adequate CTV coverage in respiratory motion patients. Future work should consider replication of this study using a 4D lung-equivalent phantom to explore system's performance for thoracic treatments.

References

Agnew, C. E. and McGarry, C. K. (2016). A tool to include gamma analysis software into a quality assurance program. *Radiotherapy and Oncology*, 118(3):568–573.

Ashland Advanced Materials (2019). *FilmQA^{TM} Pro User Guide*. Bridgewater, NJ, USA. Version 7.0.

Autret, D., Guillerminet, C., Roussel, A., Cossec-Kerloc'h, E., and Dufreneix, S. (2023). Comparison of four synthetic CT generators for brain and prostate MR-only workflow in radiotherapy. *Radiation Oncology*, 18(1):146.

Benitez, C. M., Steinberg, M. L., Cao, M., Qi, X. S., Lamb, J. M., Kishan, A. U., and Valle, L. F. (2023). Mri-guided radiation therapy for prostate cancer: the next frontier in ultrahypofractionation. *Cancers*, 15(18):4657.

Berson, A. M., Emery, R., Rodriguez, L., Richards, G. M., Ng, T., Sanghavi, S., and Barsa, J. (2004). Clinical experience using respiratory gated radiation therapy: Comparison of free-breathing and breath-hold techniques. *International Journal of Radiation Oncology*Biology*Physics*, 60(2):419–426.

Bertholet, J., Knopf, A., Eiben, B., McClelland, J., Grimwood, A., Harris, E., Menten, M., Poulsen, P., Nguyen, D. T., Keall, P., and Oelfke, U. (2019). Real-time intrafraction motion monitoring in external beam radiotherapy. *Physics in Medicine & Biology*, 64(15):15TR01.

Bortfeld, T., Jokivarsi, K., Goitein, M., Kung, J., and Jiang, S. B. (2002). Effects of intra-fraction motion on imrt dose delivery: statistical analysis and simulation. *Physics in Medicine & Biology*, 47(13):2203.

Brady, S. L., Brown, W. E., Clift, C. G., Yoo, S., and Oldham, M. (2010). Investigation into the feasibility of using PRESAGE™/optical-CT dosimetry for the verification of gating treatments. *Physics in Medicine and Biology*, 55(8):2187–2201.

Brown, K. (2024). Elekta Unity Comprehensive Motion Management—Explained.

Butson, M. J., Cheung, T., and Yu, P. (2009). Evaluation of the magnitude of EBT Gafchromic film polarization effects. *Australasian Physics & Engineering Sciences in Medicine*, 32(1):21–25.

Chiloiro, G., Boldrini, L., Romano, A., Placidi, L., Tran, H. E., Nardini, M., Massaccesi, M., Cellini, F., Indovina, L., and Gambacorta, M. A. (2023). Magnetic resonance-guided stereotactic body radiation therapy (MRgSBRT) for oligometastatic patients: a single-center experience. *La radiologia medica*, 128(5):619–627.

CIRS (2019). ZEUS: MRgRT Motion Management QA Phantom.

Corbett, J. (2022). Elekta Unity with CMM at UMC Utrecht—first patient experience. Elekta. Webinar.

Corradini, S., Alongi, F., Andratschke, N., Belka, C., Boldrini, L., Cellini, F., Debus, J., Guckenberger, M., Hörner-Rieber, J., Lagerwaard, F., Mazzola, R., Palacios, M., Philippens, C., Raaijmakers, J., Terhaard, C., Valentini, V., and Niyazil, M. (2019). MR-guidance in clinical reality: current treatment challenges and future perspectives. *Radiation Oncology*, 14.

Cuccia, F., Mazzola, R., Nicosia, L., Figlia, V., Giaj-Levra, N., Ricchetti, F., Rigo, M., C., V., Mantoan, B., De Simone, A., Sicignano, G., Ruggieri, R., Cavalleri, S., and Alongi, F. (2020). Impact of hydrogel peri-rectal spacer insertion on prostate gland intra-fraction motion during 1.5t mr-guided stereotactic body radiotherapy. *Radiation oncology*, 15.

Cui, G., Housley, D. J., Chen, F., Mehta, V. K., and Shepard, D. M. (2014). Delivery efficiency of an Elekta linac under gated operation. *Journal of Applied Clinical Medical Physics*, 15(5):2–11.

Das, I. J., Alongi, F., Yadav, P., and Mittal, B. B. (2024). *A Practical Guide to MR-Linac: Technical Innovation and Clinical Implication*. Springer Nature.

Dassen, M. G. et al. (2023). Comparing adaptation strategies in mri-guided online adaptive radiotherapy. *Radiotherapy and Oncology*. Quantifies ATP vs. ATS accuracy, finding ATS superior under significant anatomical change.

Datta, A., Aznar, M. C., Dubec, M., Parker, G. J. M., and O'Connor, J. P. B. (2018). Delivering functional imaging on the mri-linac: Current challenges and potential solutions. *Clinical oncology (Royal College of Radiologists (Great Britain))*, 30:702–710.

Devic, S. (2011). Radiochromic film dosimetry: past, present, and future. *Physica medica*, 27(3):122–134.

Dunn, L., Kron, T., Johnston, P. N., McDermott, L. N., Taylor, M. L., Callahan, J., and Franich, R. D. (2012a). A programmable motion phantom for quality assurance of motion management in radiotherapy. *Australas Phys Eng Sci Med*, 35:93–100.

Dunn, L., Kron, T., Johnston, P. N., McDermott, L. N., Taylor, M. L., Callahan, J., and Franich, R. D. (2012b). A programmable motion phantom for quality assurance of motion management in radiotherapy. *Australasian Physical & Engineering Sciences in Medicine*, 35(1):93–100.

Elekta (2022). Elekta unity's motion management capabilities herald a new era in precision radiation therapy. `https://ir.elekta.com/investors/press-releases/2022/elekta-unitys-motion-management-capabilities-herald-a-new-era-in-precision-radiation-therapy/`. Press release.

Elekta (2023a). Elekta receives fda 510(k) clearance for advanced radiotherapy motion management using elekta unity mr-linac. `https://ir.elekta.com/investors/pres`

s-releases/2023/elekta-receives-fda-510k-clearance-for-advanced-radiotherapy-motion-management-using-elekta-unity-mr-linac/. Press release.

Elekta (2023b). *Elekta Unity Instructions for Use – Clinical Mode*. Elekta.

Finazzi, T., Palacios, M. A., Haasbeek, C. J. A., Admiraal, M. A., Spoelstra, F. O. B., Bruynzeel, A. M. E., Slotman, B. J., Lagerwaard, F. J., and Senan, S. (2020). Stereotactic MR-guided adaptive radiation therapy for peripheral lung tumors. *Radiotherapy and oncology : journal of the European Society for Therapeutic Radiology and Oncology*, 144:46–52.

Freislederer, P., Reiner, M., Hoischen, W., Quanz, A., Heinz, C., Walter, F., Belka, C., and Soehn, M. (2015). Characteristics of gated treatment using an optical surface imaging and gating system on an Elekta linac. *Radiation Oncology*, 10(1):68.

Green, O. L., Rankine, L. J., Cai, B., Curcuru, A., Kashani, R., Rodriguez, V., Li, H. H., Parikh, P. J., Robinson, C. G., Olsen, J. R., Mutic, S., Goddu, S. M., and Santanam, L. (2018). First clinical implementation of real-time, real anatomy tracking and radiation beam control. *Medical Physics*, 45(8):3728–3740.

Guan, F., Chen, H., Draeger, E., Li, Y., Aydin, R., Tien, C. J., and Chen, Z. (2023a). Characterization of gafchromic™ ebt4 film with clinical kv/mv photons and mev electrons. *Precision Radiation Oncology*, 7(2):84–91.

Guan, F. et al. (2023b). Dosimetric response of gafchromic™ ebt-xd film to to therapeutic protons. *Applied Clinical Medical Physics*. EBT-XD has broader optimal dynamic dose range up to 40 Gy.

Han, E., Luo, D., Kim, J., Tharp, K., Wen, Z., and Briere, T. (2019). Dosimetric validation of the gamma knife® icontm plan adaptation and high-definition motion management system with a motorized anthropomorphic head phantom. *J Radiosurg SBRT.*, 6.

Hussein, M., Clark, C., and Nisbet, A. (2017). Challenges in calculation of the gamma index in radiotherapy–towards good practice. *Physica Medica*, 36:1–11.

ICRU (2010). ICRU Report 83: Prescribing, Recording, and Reporting Photon-Beam Intensity-Modulated Radiation Therapy (IMRT). Technical Report 1, ICRU, Journal of the ICRU, Oxford University Press.

ICRU Report 50 (1992). Prescribing, Recording, and Reporting Photon Beam Therapy.

ICRU Report 62 (1999). ICRU Report 62, Prescribing, Recording and Reporting Photon Beam Therapy (Supplement to ICRU 50). 32.

International Organization for Standardization (2006). Iso 3534-1:2006 — statistics — vocabulary and symbols — part 1: General statistical terms and terms used in probability. Standard.

Jiang, S. B., Wolfgang, J., and Mageras, G. S. (2008). Quality Assurance Challenges for Motion-Adaptive Radiation Therapy: Gating, Breath Holding, and Four-Dimensional Computed Tomography. *International Journal of Radiation Oncology*Biology*Physics*, 71(1):S103–S107.

Johno, H., Saito, M., and Onishi, H. (2018). Prediction-based compensation for gate on/off latency during respiratory-gated radiotherapy. *Computational and mathematical methods in medicine*, 2018(1):5919467.

Keall, P. J., Mageras, G. S., Balter, J. M., Emery, R. S., Forster, K. M., Jiang, S. B., Kapatoes, J. M., Low, D. A., Murphy, M. J., Murray, B. R., et al. (2006). The management of respiratory motion in radiation oncology report of aapm task group 76 a. *Medical physics*, 33(10):3874–3900.

Keshmiri, S., Lemaire, G., André, A., Thevenet, F., Ocadiz, A., Rosuel, N., Huffschmidt, B., Bencheikh, Y., Ghafooryan-Sangchooli, M., Pellicioli, P., et al. (2025). Recent advances in film dosimetry for quality assurance in microbeam radiation therapy. *Scientific Reports*, 15(1):28959.

Kim, J., Lee, Y., Shin, H., Ji, S., Park, S., Kim, J., Jang, H., and Kang, Y. (2016). Development of Deformable Moving Lung Phantom to Simulate Respiratory Motion in Radiotherapy. *Medical Dosimetry*, 41(2):113–117.

Kim, T., Lewis, B., Lotey, R., Barberi, E., and Green, O. (2021). Clinical experience of MRI ^{4D} QUASAR motion phantom for latency measurements in 0.35T MR-LINAC. *Journal of Applied Clinical Medical Physics*, 22(1):128–136.

Kron, T., Clements, N., Aarons, Y., Dunn, L., Chesson, B., Miller, J., Roozen, K., and Ball, D. (2011). Radiochromic film for individual patient QA in extracranial stereotactic lung radiotherapy. *Radiation Measurements*, 46(12):1920–1923.

Lachaine, M. and Falco, T. (2013). Intrafractional Prostate Motion Management with the Clarity Autoscan System.

Lamb, J. M., Ginn, J. S., O'Connell, D. P., Agazaryan, N., Cao, M., Thomas, D. H., Yang, Y., Lazea, M., Lee, P., and Low, D. A. (2017). Dosimetric validation of a magnetic resonance image gated radiotherapy system using a motion phantom and radiochromic film. *Journal of Applied Clinical Medical Physics*, 18(3):163–169.

Lee, S. H., Kim, K. B., Kim, M.-S., Yoo, H.-J., Park, S., Jung, H., Ji, Y. H., and Yi, C.-Y. (2013). Quantitative analysis of dose distribution to determine optimal width of respiratory gating window using Gafchromic EBT2 film. *Journal of the Korean Physical Society*, 62(4):657–663.

Lewis, B. C., Shin, J., Maraghechi, B., Quinn, B., Cole, M., Barberi, E., Kim, J. S., Green, O., and Kim, T. (2022). Assessment of a novel commercial large field of view phantom for comprehensive MR imaging quality assurance of a 0.35T MRgRT system. *Journal of Applied Clinical Medical Physics*, 23(4):e13535.

Lewis, D. and Chan, M. F. (2015). Correcting lateral response artifacts from flatbed scanners for radiochromic film dosimetry. *Medical Physics*, 42(1):416–429.

Lewis, D., Micke, A., Yu, X., and Chan, M. F. (2012). An efficient protocol for radiochromic film dosimetry combining calibration and measurement in a single scan. *Medical Physics*, 39(10):6339–6350.

Ma, C.-M. C. (2019). Physics and Dosimetric Principles of SRS and SBRT. *Mathews J Cancer Science*, 4.

Méndez, I., Rovira-Escutia, J. J., and Casar, B. (2021). A protocol for accurate radiochromic film dosimetry using radiochromic. com. *Radiology and oncology*, 55(3):369.

Micallef, K. A. (2025). Validation of a motion management and gating protocol on the Elekta Unity MR Linac for margin reduction in prostate cancer. Master's thesis, University of Malta.

Miura, H. et al. (2016). Gafchromic ebt-xd film: Dosimetry characterization in high-dose volumetric-modulated arc therapy. *J Appl Clin Med Phys*. EBT-XD dynamic range up to 40 Gy.

Modus QA (2022). *MRI_4D v2.0 Low Latency Controller User's Guide*. Modus Medical Devices Inc., London, Ontario, Canada. Document ID: P312987 R2.

Ng, J., Gregucci, F., Pennell, R. T., Nagar, H., Golden, E. B., Knisely, J. P. S., Sanfilippo, N. J., and Formenti, S. C. (2023). MRI-LINAC: A transformative technology in radiation oncology. *Frontiers in Oncology*, 13:1117874.

Nicosia, L., Rigo, M., Pellegrini, R. G., Allegra, A. G., De-Colle, C., Giaj-Levra, N., Pastorello, E., Ricchetti, F., Ruggieri, R., and Alongi, F. (2025). First clinical application of comprehensive motion management with 1.5 t mr-linac on prostate cancer patients treated with radiotherapy: technical aspects and suggested workflow recommendations. *La radiologia medica*, pages 1–6.

Nioutsikou, E., Seppenwoolde, Y., Symonds-Tayler, J. R. N., Heijmen, B., Evans, P., and Webb, S. (2008). Dosimetric investigation of lung tumor motion compensation with a robotic respiratory tracking system: An experimental study. *Medical Physics*, 35(4):1232–1240.

Niroomand-Rad, A., Blackwell, C. R., Coursey, B. M., Gall, K. P., Galvin, J. M., McLaughlin, W. L., Meigooni, A. S., Nath, R., Rodgers, J. E., and Soares, C. G. (1998). Radiochromic film dosimetry: Recommendations of AAPM Radiation Therapy Committee Task Group 55. *Medical Physics*, 25(11):2093–2115.

Ocanto, A., Torres, L., Montijano, M., Rincón, D., Fernández, C., Sevilla, B., Gonsalves, D., Teja, M., Guijarro, M., Glaría, L., Hernánz, R., Zafra-Martin, J., Sanmamed, N., Kishan, A., Alongi, F., Moghanaki, D., Nagar, H., and Couñago, F. (2024). MR-LINAC, a New Partner in Radiation Oncology: Current Landscape. *Cancers*, 16(2):270.

Oliver, M., Staruch, R., Gladwish, A., Craig, J., Chen, J., and Wong, E. (2008). Monte Carlo dose calculation of segmental IMRT delivery to a moving phantom using dynamic MLC and gating log files. *Physics in Medicine and Biology*, 53(10):N187–N196.

Oncology Medical Physics (2023). Film dosimeters. `https://oncologymedicalphysics.com/film-dosimeters/`.

Pepin, E. W., Wu, H., and Shirato, H. (2011). Dynamic gating window for compensation of baseline shift in respiratory-gated radiation therapy. *Medical Physics*, 38(4):1912–1918.

Placidi, L., Nardini, M., Cusumano, D., Boldini, L., Chiloiro, G., Votta, C., Antonelli, M., Valentini, V., and Indovina, L. (2021). OD51 - Dosimetric and planning evaluation of IMRT vs VMAT-like plans for magnetic resonance guided radiotherapy treatment. *Physica Medica*, 92:S79–S80. Abstracts of the 3rd European Congress of Medical Physics.

Powers, M., Baines, J., Crane, R., Fisher, C., Gibson, S., Marsh, L., Oar, B., Shoobridge, A., Simpson-Page, E., Van der Walt, M., and de Vine, G. (2022). Commissioning measurements on an Elekta Unity MR-Linac. *Physical and engineering sciences in medicine*, 45:457–473.

Rammohan, N., Randall, J. W., and Yadav, P. (2022). History of Technological Advancements towards MR-Linac: The Future of Image-Guided Radiotherapy. *Journal of Clinical Medicine*, 11(16):4730.

Rana, S. (2013). Intensity modulated radiation therapy versus volumetric intensity modulated arc therapy. *J Med Radiat Sci.*, 60.

Reinhardt, S., Hillbrand, M., Wilkens, J. J., and Assmann, W. (2012). Comparison of gafchromic ebt2 and ebt3 films for clinical photon and proton beams. *Medical Physics*, 39(10):5448–5458.

Roberts, D. A., Sandin, C., Vesanen, P. T., Lee, H., Hanson, I. M., Nill, S., Perik, T., Lim, S. B., Vedam, S., Yang, J., Woodings, S. W., Wolthaus, J. W. H., Keller, B., Budgell, G., Chen, X., and Li, X. A. (2021). Machine QA for the Elekta Unity system: A Report from the Elekta MR-linac consortium. *Medical Physics*, 48(5).

Rusu, S., Smith, B., At-Aubin, J., Shaffer, N., and Hyer, D. E. (2024). Surrogate gating strategies for the elekta unity mr-linac gating system. *Journal of applied clinical Medical Physics*.

Saito, M., Kawahara, D., Takahashi, Y., Ono, T., Torii, T., Yamashita, H., and Ohtomo, K. (2018). Evaluation of the latency and the beam characteristics of a respiratory gating system using an elekta linear accelerator and a respiratory indicator device, abches. *Medical Physics*, 45(12):5402–5408.

Schnarr, E., Beneke, M., Casey, D., Chao, E., Chappelow, J., Cox, A., Henderson, D., Jordan, P., Lessard, E., Lucas, D., Myronenko, A., and Maurer, C. (2018). Feasibility of real-time motion management with helical tomotherapy. *Journal of Medical Physics*, 45.

Shiinoki, T., Kawamura, S., Uehara, T., Yuasa, Y., Fujimoto, K., Koike, M., Sera, T., Emoto, Y., Hanazawa, H., and Shibuya, K. (2016). Evaluation of a combined respiratory-gating system comprising the TrueBeam linear accelerator and a new real-time tumor-tracking radiotherapy system: A preliminary study. *Journal of Applied Clinical Medical Physics*, 17(4):202–213.

Short, W. A. (2018). *Evaluating the Dosimetric Accuracy of Small Gating Windows Using Film Dosimetry*. PhD thesis, The Ohio State University. Shows up to 7× increase in treatment time for small beam-on windows, with film gamma pass rates > 95

Smith, B. R., St-Aubin, J., and Hyer, D. E. (2025). Commissioning of a motion management system for a 1.5 t elekta unity mr-linac: A single institution experience. *Journal of applied clinical medical physics*, 26(4):e70005.

Snyder, J. E., Hyer, D. E., Flynn, R. T., Boczkowski, A., and Wang, D. (2019). The commissioning and validation of Monaco treatment planning system on an Elekta Versa HD linear accelerator. *Journal of Applied Clinical Medical Physics*, 20(1):184–193.

Soloviev, A., Burdonov, K., Chen, S., Eremeev, A., Korzhimanov, A., Pokrovskiy, G., Pikuz, T., Revet, G., Sladkov, A., Ginzburg, V., et al. (2017). Experimental evidence for short-pulse laser heating of solid-density target to high bulk temperatures. *Scientific Reports*, 7(1):12144.

Szkitsak, J., Werner, R., Fernolendt, S., Schwarz, A., Ott, O. J., Fietkau, R., Hofmann, C., and Bert, C. (2021). First clinical evaluation of breathing controlled four-dimensional computed tomography imaging. *Physics and imaging in radiation oncology*, 20.

Taylor, A. and Powell, M. (2004). Intensity-modulated radiotherapy-what is it? . *Cancer Imaging*, 4:68–73.

Tekatli, H., Palacios, M. A., Schneiders, F. L., Haasbeek, C. J. A., Slotman, B. J., Lagerwaard, F. J., and Senan, S. (2023). Local control and toxicity after magnetic resonance imaging (MR)-guided single fraction lung stereotactic ablative radiotherapy. *Radiotherapy and oncology : journal of the European Society for Therapeutic Radiology and Oncology*, 187.

Tsekas, G., Bol, G. H., and Raaymakers, B. W. (2022). Robust deep learning-based forward dose calculations for VMAT on the 1.5T MR-linac. *Physics in Medicine Biology*, 67(22):225020.

Tsiakalos, M. F., Theodorou, K., Kappas, C., Zefkili, S., and Rosenwold, J.-C. (2004). Analysis of the penumbra enlargement in lung versus the quality index of photon beams: a methodology to check the dose calculation algorithm. *Medical physics*, 31(4):943–949.

Uijtewaal, P., Borman, P., Cote, B., LeChasseur, Y., Therriault-Proulx, F., Flores, R., Smith, S., Koenig, G., Raaymakers, B., and Fast, M. (2024). Performance characterization of a novel hybrid dosimetry insert for simultaneous spatial, temporal, and motion-included dosimetry for mr-linac. *Medical Physics*, 51(4):2983–2997.

Uno, T., Tsuneda, M., Abe, K., Fujita, Y., Harada, R., Saito, M., Kanazawa, A., Kodate, A., Abe, Y., Ikeda, Y., Nemoto, M. W., and Yokota, H. (2023). A New Workflow of the On-Line 1.5-T MR-guided Adaptive Radiation Therapy. *Japanese Journal of Radiology*, 41(11):1316–1322.

Viel, F., Lee, R., Gete, E., and Duzenli, C. (2015). Amplitude gating for a coached breathing approach respiratory gated 10 mv flattening filter-free vmat delivery. *Journal of applied clinical medical physics*, 16.

Wang, L., Kielar, K. N., Mok, E., Hsu, A., Dieterich, S., and Xing, L. (2012). An end-to-end examination of geometric accuracy of IGRT using a new digital accelerator equipped with onboard imaging system. *Physics in Medicine and Biology*, 57(3):757–769.

Wen, N., Kim, J., Doemer, A., Glide-Hurst, C., Chetty, I. J., Liu, C., Laugeman, E., Xhaferllari, I., Kumarasiri, A., Victoria, J., Bellon, M., Kalkanis, S., Siddiqui, M. S., and Movsas, B. (2018). Evaluation of a magnetic resonance guided linear accelerator for stereotactic radiosurgery treatment. *Radiotherapy and Oncology*, 127(3):460–466.

White, P. J., Zwicker, R. D., and Huang, D. T. (1996). Comparison of dose homogeneity effects due to electron equilibrium loss in lung for 6 mv and 18 mv photons. *International Journal of Radiation Oncology* Biology* Physics*, 34(5):1141–1146.

Wiersma, R. D., McCabe, B. P., Belcher, A. H., Jensen, P. J., Smith, B., and Aydogan, B. (2016). Technical Note: High temporal resolution characterization of gating response time. *Medical Physics*, 43(6Part1):2802–2806.

Winkel, D., Bol, G. H., Kroon, P. S., Van Asselen, B., Hackett, S. S., Werensteijn-Honingh, A. M., Intven, M. P., Eppinga, W. S., Tijssen, R. H., Kerkmeijer, L. G., De Boer, H. C.,

Mook, S., Meijer, G. J., Hes, J., Willemsen-Bosman, M., De Groot-van Breugel, E. N., Jürgenliemk-Schulz, I. M., and Raaymakers, B. W. (2019). Adaptive radiotherapy: The Elekta Unity MR-linac concept. *Clinical and Translational Radiation Oncology*, 18:54–59.

Woodings, S. J., Bluemink, J. J., De Vries, J. H. W., Niatsetski, Y., Van Veelen, B., Schillings, J., Kok, J. G. M., Wolthaus, J. W. H., Hackett, S. L., Van Asselen, B., Van Zijp, H. M., Pencea, S., Roberts, D. A., Lagendijk, J. J. W., and Raaymakers, B. W. (2018). Beam characterisation of the 1.5 T MRI-linac. *Physics in Medicine & Biology*, 63(8):085015.

Woodings, S. J., De Vries, J. H. W., Kok, J. M. G., Hackett, S. L., Van Asselen, B., Bluemink, J. J., Van Zijp, H. M., Van Soest, T. L., Roberts, D. A., Lagendijk, J. J. W., Raaymakers, B. W., and Wolthaus, J. W. H. (2021). Acceptance procedure for the linear accelerator component of the 1.5 T MRI-linac. *Journal of Applied Clinical Medical Physics*, 22(8):45–59.

Zhou, H. et al. (2024). Dosimetric comparison of adapt-to-position and adapt-to-shape workflows for mri-guided adaptive radiotherapy in cervical cancer. *Applied Radiation and Nuclear Medicine*, 2(4):1–10.

A

Assessment of Fusion Masking Options

The ±20mm scans were used to assess different image fusion masks options available on Monaco software. For each repeated reading different volume of interest (VOI) were taken into consideration to account for slight variation in the actual data collection:

- First repeated reading the VOI was close to the border of the insert.
- Second repeated reading the border of the insert was completely eliminated.
- Third repeated reading the VOI was extremely tight around the target.

Moreover, it is important to note that, for standardization across all positions in the data collection, the y-value in the transformation matrix (which corresponds to the superior-inferior direction) was set to 17 mm. The results are tabulated as follows:

From the results one can deduce that using the RE Segmentation Mask provided the lesser spread and standard deviation making it the most reliable image fusion masking option for the data collection.

Table A.1: Position data and statistical measures for ±20mm using Shape Intensity Model Mask. SD = Standard Deviation.

	Shape Intensity Model					
	+20mm			**−20mm**		
	x	**y**	**z**	**x**	**y**	**z**
1	-2.525	20.336	-7.709	-2.221	-20.411	-6.594
2	-2.670	19.599	-7.333	-2.137	-20.499	-7.181
3	-2.547	20.382	-7.181	-2.100	-20.101	-7.181
Spread	-0.0562	0.0389	-0.0712	-0.0562	-0.0196	-0.0840
SD	0.0063	0.0359	0.0222	0.0051	0.0171	0.0277

Table A.2: Position data and statistical measures for ±20mm using RE Segmentation Mask. SD = Standard Deviation.

	RE Segmentation					
	+20mm			**−20mm**		
	x	**y**	**z**	**x**	**y**	**z**
1	-2.525	20.336	-7.709	-1.944	-19.681	-7.181
2	-2.525	20.336	-7.709	-1.944	-19.681	-7.181
3	-2.513	19.846	-7.643	-2.077	-19.680	-7.181
Spread	-0.0048	0.0243	-0.0086	-0.0669	-5.1×10^{-5}	0
SD	0.0007	0.0231	0.0031	0.0063	4.7×10^{-5}	1.1×10^{-16}

Table A.3: Position data and statistical measures for ±20mm using no Mask. SD = Standard Deviation.

	No Mask					
	+20mm			**−20mm**		
	x	**y**	**z**	**x**	**y**	**z**
1	-2.370	20.462	-6.951	-2.154	-19.681	-7.181
2	-2.438	20.334	-7.709	-2.089	-19.681	-7.181
3	-2.565	19.820	-7.709	-2.443	20.237	-7.181
Spread	-0.0793	0.0318	-0.1017	-0.1588	-6.2616	0
SD	0.0081	0.0277	0.0357	0.0154	1.8818	1.1×10^{16}

Manual fusion was also done for the ±20mm scans with the reference axis of 0mm. The results can be seen in TableA.4. These were then compared with the values obtained in the $x.y$ and z direction for the ±20mm as tabulated in section 4.2.1. Thus, the error

Table A.4: Manual Error Calculation for Sphere Target at ±20mm

	Manual Fusion Calculation					
	x	**y**	**z**	**x**	**y**	**z**
	+20mm			**-20mm**		
1	-2.500	20.000	-7.620	-2.010	-19.840	-7.200
2	-2.510	20.230	-7.580	-2.020	-19.770	-7.180
3	-2.470	20.150	-7.600	-1.980	-19.810	-7.200
Average	**-2.493**	**20.127**	**-7.600**	**-2.003**	**-19.807**	**-7.193**

from these values for the $x.y$ and z were also outputted and were found to be 0.03, -0.05, 0.09 respectively. Yielding the values obtained from the automatic fusion reliable.

B

Detailed Tabulation of Translational and Rotational Positioning Errors

Table B.1: Data representation of Monaco left-right relative positions and their errors for translational only setting. * Refers to the value obtained by Modus Equations themselves. ** Refers to the theoretical value expected from Monaco, derived from equations relative to the 0mm position. *** Refers to the actual values measured from Monaco. SD = Standard Deviation

left-right* $x(w)$	**Monaco left-right relative to 0 position (Theoretical)****	**Monaco left-right relative to 0 position (Measured)*****	**X Error** (Δx)
-15	0.00	-0.02	-0.02
-15	0.00	-0.02	-0.02
-15	0.00	-0.03	-0.03
-15	0.00	-0.02	-0.02
-15	0.00	0.00	0.00
-15	0.00	-0.02	-0.02
-15	0.00	-0.01	-0.01
-15	0.00	-0.03	-0.03
-15	0.00	-0.03	-0.03
		Abs Maximum	0.03
		Abs Minimum	0.00
		Abs Average	0.02
		SD	0.01

Table B.2: Data representation of Monaco ant-post relative positions and their errors for translational only setting. * Refers to the value obtained by Modus Equations themselves. ** Refers to the theoretical value expected from Monaco, derived from equations relative to the 0mm position. *** Refers to the actual values measured from Monaco. SD = Standard Deviation

anterior-posterior* $y(w)$	**Monaco anterior-posterior relative to 0 position (Theoretical)****	**Monaco ant-post relative to 0 position (Measured)*****	**Y Error** Δy
0.00	0.00	0.00	0.00
0.00	0.00	0.00	0.00
0.00	0.00	0.00	0.00
0.00	0.00	0.00	0.00
0.00	0.00	0.00	0.00
0.00	0.00	0.00	0.00
0.00	0.00	0.00	0.00
		Abs Maximum	0.00
		Abs Minimum	0.00
		Abs Average	0.00
		SD	0

Table B.3: Data representation of Monaco superior -inferior relative positions and their errors for translational only setting. * Refers to the value obtained by Modus Equations themselves. ** Refers to the theoretical value expected from Monaco, derived from equations relative to the 0mm position. *** Refers to the actual values measured from Monaco. SD = Standard Deviation

superior-inferior* $z(w)$	**Monaco sup-inf relative to 0 position (Theoretical)****	**Monaco sup-inf relative to 0 position (Measured)*****	**Z Error** (Δz)
20	20	20.09	0.09
15	15	15.09	0.09
10	10	10.09	0.09
5	5	5.09	0.09
0	0	0	0.00
-5	-5	-5.06	-0.06
-10	-10	-10.09	-0.09
-15	-15	-15.09	-0.09
-20	-20	-20.09	-0.09
		Abs Maximum	0.09
		Abs Minimum	0.00
		Abs Average	0.08
		SD	0.08

Table B.4: Data representation of Monaco left-right relative positions and their errors for translational and rotational setting. * Refers to the value obtained by Modus Equations themselves. ** Refers to the theoretical value expected from Monaco, derived from equations relative to the 0mm position. *** Refers to the actual values measured from Monaco. SD = Standard Deviation

left-right* $x(w)$	**Monaco left-right relative to 0 position (Theoretical)****	**Monaco left-right relative to 0 position (Measured)*****	**X Error (Δx)**
-15.00	-2.01	-2.52	-0.51
-14.16	-1.17	-1.32	-0.16
-13.52	-0.53	-0.72	-0.19
-13.13	-0.13	-0.17	-0.03
-12.99	0	0	0.00
-13.13	-0.13	-0.20	-0.07
-13.52	-0.53	-0.73	-0.20
-14.16	-1.17	-1.01	0.16
-15.00	-2.01	-1.99	0.02
		Abs Maximum	0.16
		Abs Minimum	0.00
		Abs Average	0.15
		SD	0.178

Table B.5: Data representation of Monaco ant-post relative positions and their errors for translational and rotational setting. * Refers to the value obtained by Modus Equations themselves. ** Refers to the theoretical value expected from Monaco, derived from equations relative to the 0mm position. *** Refers to the actual values measured from Monaco. SD = Standard Deviation

ant-post* $y(w)$	**Monaco ant-post relative to 0 position (Theoretical)****	**Monaco ant-post relative to 0 position (Measured)*****	**Y Error (Δy)**
0.00	-7.50	-7.69	-0.19
4.96	-2.50	-2.48	0.01
6.50	-1.00	-0.69	0.21
7.26	-0.24	0.00	0.24
7.50	0.00	0.00	0.00
7.26	-0.24	0.00	0.24
6.50	-1.00	-0.71	0.20
4.96	-2.54	-2.45	0.09
0.00	-7.50	-7.18	0.32
		Abs Maximum	0.32
		Abs Minimum	0.00
		Abs Average	0.19
		SD	0.164

Table B.6: Data representation of Monaco superior-inferior relative positions and their errors for translational and rotational setting. * Refers to the value obtained by Modus Equations themselves. ** Refers to the theoretical value expected from Monaco, derived from equations relative to the 0mm position. *** Refers to the actual values measured from Monaco. SD = Standard Deviation

superior-inferior* $z(w)$	**Monaco sup-inf relative to 0 position (Theoretical)****	**Monaco sup-inf relative to 0 position (Measured)*****	**Z Error (Δz)**
20	20	20.17	0.25
15	15	14.68	-0.22
10	10	10.30	0.20
5	5	5.09	0.09
0	0	0.00	0.00
-5	-5	-5.09	-0.09
-10	-10	-9.68	0.22
-15	-15	-14.68	0.22
-20	-20	-19.68	0.32
		Abs Maximum	0.32
		Abs Minimum	0.00
		Abs Average	0.21
		SD	0.213

C

FREC approval

L-Università ta' Malta

Maronia Chetcuti <maronia.chetcuti.20@um.edu.mt>

The status of your REDP form (FHS-2024-00640) has been updated to Acknowledged

1 message

form.urec@um.edu.mt <form.urec@um.edu.mt> 15 November 2024 at 15:49
To: maronia.chetcuti.20@um.edu.mt

Dear Maronia Chetcuti,

Please note that the status of your REDP form (FHS-2024-00640) has been set to *Acknowledged*.

You can keep track of your applications by visiting: https://www.um.edu.mt/research/ethics/redp-form/frontEnd/.

This email has been automatically generated by URECA. Please do not reply. If you wish to communicate with your F/REC please use the respective email address.

D

Filling the Film Insert with Aqueous Contrast Solution

As indicated in Modus QA (2022), to prepare the aqueous contrast solution for phantom filling, a manganese-based stock solution (1000 ppm Mn^{2+}) needed to be created. This was done by dissolving 360 mg of manganese(II) chloride tetrahydrate ($MnCl_2 \cdot 4H_2O$) in 100 mL of deionized water (d.i. H_2O) using a 100 mL mixing jar (Figure D.1). Based on the target concentrations required for each phantom compartment, specific volumes of the stock solution were diluted with d.i. H_2O to achieve the desired final concentrations.

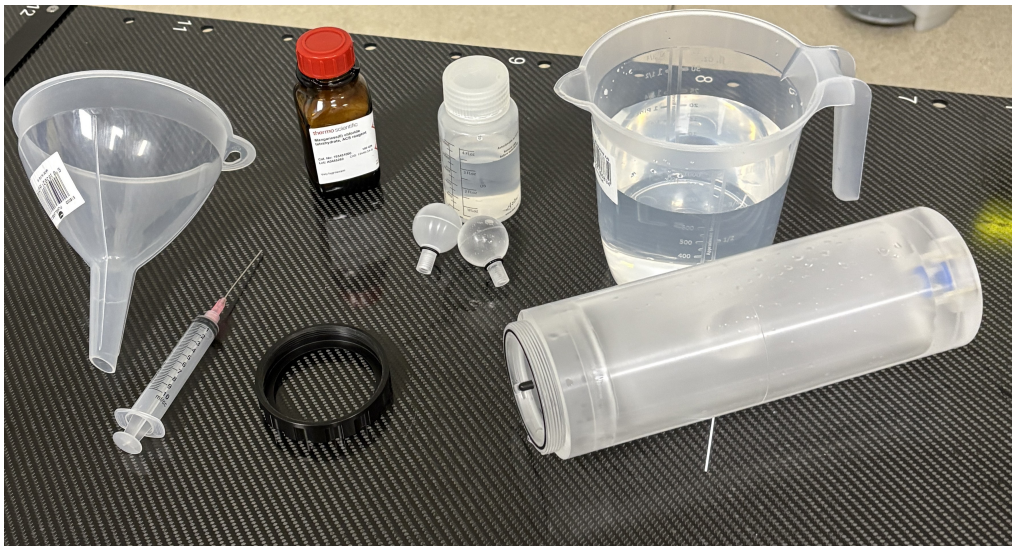

Figure D.1: Equipment used for filling of the film insert and making of the stock solution

To achieve a 70 ppm Mn^{2+} concentration in the 30-mm fillable hollow sphere, 1.0 mL of stock solution was combined with 13.5 mL of d.i. H_2O as stated in the user guide (Modus QA, 2022). To ensure homogeneity, compartments were partially filled with water before adding the stock solution, and thoroughly mixed before being filled to capacity.

Index